Teemu Niemi

Polarization transformations in bianisotropic arrays

School of Electrical Engineering

Thesis submitted for examination for the degree of Master of Science in Technology.

Espoo 21.3.2012

Thesis supervisor:

Prof. Sergei Tretyakov

Thesis instructor:

M.Sc. (Tech.) Antti Karilainen

Aalto University
School of Electrical
Engineering

AALTO UNIVERSITY
SCHOOL OF ELECTRICAL ENGINEERING

ABSTRACT OF THE
MASTER'S THESIS

Author: Teemu Niemi

Title: Polarization transformations in bianisotropic arrays

Date: 21.3.2012 Language: English Number of pages:8+62

Department of Radio Science and Technology

Professorship: Radio Science Code: S-26

Supervisor: Prof. Sergei Tretyakov

Instructor: M.Sc. (Tech.) Antti Karilainen

This thesis studies regular arrays of the most general bianisotropic particles. The goal is to develop a systematic way to find required polarizabilities for these scatters so that, when ordered into periodical lattices, they exhibit any wanted polarization transformation for a plane wave. The method is verified by synthesizing two different devices: a circular polarization selective surface and a twist polarizer. A circular polarization selective surface is a device that transmits one handedness of circular polarization and reflects the other. A twist polarizer rotates the plane of polarization of a linearly polarized plane wave by 90°. The operation of the synthesized devices is verified by analytical models, numerical simulations, and experimental measurements. The results indicate that the developed method can be efficiently used for developing novel polarization transformers.

Keywords: Polarization transformation, arrays of bianisotropic particles, interaction field, circular polarisation selectivity, twist polarizer

AALTO-YLIOPISTO
SÄHKÖTEKNIIKAN KORKEAKOULU

DIPLOMITYÖN
TIIVISTELMÄ

Tekijä: Teemu Niemi

Työn nimi: Polarisaatiomuunnokset bianisotrooppisissa hiloissa

Päivämäärä: 21.3.2012 Kieli: Englanti Sivumäärä:8+62

Radiotieteen ja -tekniikan laitos

Professuuri: Radiotiede Koodi: S-26

Valvoja: Prof. Sergei Tretyakov

Ohjaaja: DI Antti Karilainen

Tämän diplomityön tavoitteena on tutkia mahdollisimman yleisistä bianisotrooppisista sirottajista muodostettuja säännöllisiä hiloja. Työssä on kehitetty menetelmä, jota käyttämällä voidaan ratkaista sellaiset polarisoituvuudet näille sirottajille, jotta niistä muodostetut säännölliset hilat totetuttavat toivotun polarisaatiomuunnoksen tasoaallolle. Menetelmän toiminta varmistetaan suunnittelemalla kaksi erilaista laitetta – ympyräpolarisaatiolle selektiivinen pinta sekä kiertopolarisaattori. Ympyräpolarisaatiolle selektiivinen pinta on laite, joka päästää toisen ympyräpolarisaation kätisyyden läpi ja heijastaa toista. Kiertopolarisaattori kiertää lineaarisesti polarisoidun tasoaallon sähkökentän suuntaa 90 astetta. Suunniteltujen laitteiden toiminta varmistetaan analyyttisillä malleilla, numeerisilla simulaatioilla sekä kokeellisilla mittauksilla. Tulokset osoittavat, että kehitetty menetelmä voi olla tehokas työkalu erilaisten polarisaatiomuuntimien suunnittelussa.

Avainsanat: Polarisaatiomuunnos, bianisotrooppinen hila, vuorovaikutuskenttä, ympyräpolarisaatioselektiivisyys, kiertopolarisaattori

Preface

This thesis was made in the Aalto University School of Electrical Engineering at the Department of Radio Science and Engineering in the research group of Advanced Artificial Materials and Smart Structures in 2011 – 2012. I would like to thank my supervisor Prof. Sergei Tretyakov for the continuing guidance and for the possibility to work in this research group for past three years on many interesting topics. I also thank my instructor M.Sc. Antti Karilainen and others who have guided me during the past few years, especially Prof. Constantin Simovski and Dr. Pekka Alitalo.

Finally, I would like to thank my family and my friends for supporting me in the course of my studies.

Otaniemi, 21.3.2012

Teemu Niemi

Contents

Abstract ii

Abstract (in Finnish) iii

Preface iv

Contents v

Symbols and abbreviations vii

1 Introduction 1

2 Polarization transformations, literature overview 3
2.1 Circular polarization selective surfaces 4
2.2 LP to CP polarizers 6
2.3 Polarization rotators 7

3 Reflection and transmission from a bianisotropic array 9
3.1 Dyadic reflection and transmission coefficients 10
3.2 Effective polarizabilities 10
3.3 The fields radiated by the induced currents 12

4 Synthesizing polarization transformers 16
4.1 Polarizabilities for a RHCPSS 16
4.1.1 CPSS without magnetic polarizabilities 18
4.1.2 A reciprocal canonical helix as a RHCPSS 19
4.2 Polarizabilities for a twist polarizer 22

5 Synthesizing arrays of uniaxial particles 24
5.1 Uniaxial twist polarizer 24

6 A CPSS using an array of chiral particles 26
6.1 Analytical model for chiral particles 26
6.2 Numerical simulations for canonical helices 27
6.3 Comparison of the results for arrays of canonical helices 28
6.3.1 Linearly polarized normal incidence 28
6.3.2 Circularly polarized incident field 29
6.4 Possible modifications for canonical helix 33
6.4.1 The effect of the unit cell size 33
6.4.2 Effect of the particles orientation 33
6.4.3 Array of horizontal $\lambda_0/2$ true helices 36
6.5 Numerical simulations for practical PCB realization 38

7 An array of chiral elements as a twist polarizer **41**
7.1 Numerical study of an idealized twist polarizer 41
7.2 Numerical study of practical PCB realization 43
7.3 Experimental verification of the twist polarizer 44
7.4 Comparison of the numerical and experimental results 47

8 Discussion and conclusions **52**

References **54**

Appendix A — Measuring transmission through a slab **58**

Symbols and abbreviations

Symbols

$\mathbf{E}_{\text{inc}}$	Incident electric field
$\mathbf{H}_{\text{inc}}$	Incident magnetic field
$\mathbf{E}_{\text{loc}}$	Local electric field
$\mathbf{H}_{\text{loc}}$	Local magnetic field
$\mathbf{E}_{\text{t}}$	Transmitted electric field
$\mathbf{E}_{\text{r}}$	Reflected electric field
ϵ_0	Vacuum permittivity, $\epsilon_0 \approx 8.854 \cdot 10^{-12}$ As/Vm
μ_0	Vacuum permittivity, $\mu_0 = 4\pi \cdot 10^{-7}$ Vs/Am
c_0	Speed of light in free space, $c_0 = 1/\sqrt{\epsilon_0 \mu_0}$
λ_0	Free space wavelength
$\mathbf{k}_0$	Wave vector in free space, $k_0 = \omega\sqrt{\epsilon_0 \mu_0} = 2\pi/\lambda_0$.
$\mathbf{p}$	Electric dipole moment induced in the unit cell
$\mathbf{m}$	Magnetic dipole moment induced in the unit cell
AR	Axial ratio in linear scale, $AR = 0 \ldots 1$
$\hat{\mathbf{x}}$, $\hat{\mathbf{y}}$, $\hat{\mathbf{z}}$	Unit vectors of the cartesian coordinate system
$\overline{\overline{\mathrm{I}}}$	Unit dyadic, $\overline{\overline{\mathrm{I}}} = \hat{\mathbf{x}}\hat{\mathbf{x}} + \hat{\mathbf{y}}\hat{\mathbf{y}} + \hat{\mathbf{z}}\hat{\mathbf{z}}$
$\overline{\overline{\mathrm{J}}}_{\text{t}}$	Transversal rotation dyadic, $\overline{\overline{\mathrm{J}}}_{\text{t}} = \hat{\mathbf{n}} \times \overline{\overline{\mathrm{I}}}_{\text{t}}$
$\overline{\overline{\alpha}}_{\text{me}}$	Polarizability dyadic, i.e, the linear mapping from $\mathbf{E}_{\text{loc}}$ to $\mathbf{m}$
$\overline{\overline{\widehat{\alpha}}}_{\text{em}}$	Effective polarizability dyadic, i.e, the linear mapping from $\mathbf{H}_{\text{inc}}$ to $\mathbf{p}$
α_{me}^{yx}	The $\hat{\mathbf{y}}\hat{\mathbf{x}}$ component of $\overline{\overline{\alpha}}_{\text{me}}$
$\overline{\overline{\beta}}_{\text{e}}$	Interaction dyadic
$\hat{\mathbf{n}}$	Normal vector of an array
a	Lattice constant of a square array
S	Area of a square unit cell, $S = a^2$
l	Length of a dipole arm (dipole length is $2l$)
r_{l}	Loop radius
L	Total lenght of the wire
r_0	Wire radius

Operators

z^*	Complex conjugate of z, $(a + jb)^* = a - jb$
$\mathbf{ab}$	Dyadic product of vectors $\mathbf{a}$ and $\mathbf{b}$
$\left(\overline{\overline{\mathrm{A}}}\right)^{-1}$	Inverse of dyadic $\overline{\overline{\mathrm{A}}}$, $\overline{\overline{\mathrm{A}}} \cdot \left(\overline{\overline{\mathrm{A}}}\right)^{-1} = \overline{\overline{\mathrm{I}}}$
$\left(\overline{\overline{\mathrm{A}}}\right)^{T}$	Transpose of dyadic $\overline{\overline{\mathrm{A}}}$
$\mathbf{ab} \cdot \mathbf{cd} = (\mathbf{b} \cdot \mathbf{c})\mathbf{ad}$	Dot-product of two dyads
$\mathbf{ab} \times \mathbf{c} = \mathbf{a}(\mathbf{b} \times \mathbf{c})$	Cross-product of a dyad and a vector

Abbreviations

CP	Circular polarization
CPSS	Circular polarization selective surface
DGR	Dual gridded reflector
FEM	Finite element method
LH	Left handed
LHCP	Left-hand circular polarization
LHCPSS	Left-hand circular polarization selective surface
LP	Linear polarization
PCB	Printed circuit board
PEC	Perfect electrical conductor
RH	Right handed
RHCP	Right-hand circular polarization
RHCPSS	Right-hand circular polarization selective surface
VNA	Vector network analyzer

1 Introduction

In the literature, one can find a wide variety of definitions for metamaterials. Usually, metamaterials are defined as materials whose electromagnetic properties are determined by their artificial structure instead of the properties of the materials they are made of [1, 2, 3]. One of the interesting applications of the antenna and metamaterial research is the possibility to manipulate the polarization state of a plane wave [4]. These polarizers have numerous applications in practical antenna engineering.

One example of an interesting polarization transformer is a circular polarization selective surface (CPSS). An ideal CPSS is a device that reflects the wave of one handedness of circular polarization (CP) and is invisible to the other. An ideal CPSS would have numerous practical applications. The initial motive for this study was in satellite communications: a surface that would reflect only wave with one sense of polarization would be a circular polarization equivalent for dual gridded reflector (DGR). DGR reflector antennas can steer the radiation beam in different directions, depending on the polarization state of the linearly polarized (LP) wave. This reduces the weight of the antenna as only one reflector is needed instead of two totally separate antenna systems. DGR reflector antennas are widely used in satellite communications [5, 6] even when the CP would be better for satellite operations. Second possible application for an ideal CPSS would be a sub-reflector for a Cassegrain antenna: the transmitted CP wave changes polarization upon reflection from the main reflector and is no longer affected by the polarization-selective sub-reflector. This would minimize the sub-reflector blockage and thus reduce the side-lobe levels [7].

A twist polarizer is a device that rotates the polarization state of a LP plane wave by 90°. A twist polarizer could be used, for example, in a multi beam satellite ground station antenna [8, 9]. In the optical regime, the polarization rotators would have applications for example in chemistry, biology, and optoelectronics [10].

The goal of this thesis is to study such polarization transformers realized as square arrays of the most general bianisotropic particles. "Bi" in the definition of bianisotropy means that the electric field at the location of the particle creates both magnetic and electric responses, not only the electric one [1]. "Anisotropy" means that the electromagnetic properties of the particle or the material depend on the direction of the exciting fields [11]. The focus is on developing a method for synthesizing bianisotropic particles – or finding their polarizabilities – so that an array of such particles would perform a wanted polarization transformation of the incident plane wave. The method is tested by synthesizing two polarization transforming devices, namely a CPSS and a twist polarizer. The synthesized geometry and dimensions for the CPSS are verified with an analytical model and numerical simulations. The twist polarizer is tested numerically and experimentally. The results for both synthesized devices clearly show that the method can be an efficient tool in developing such operations.

The structure of the thesis is as follows: After this Introduction, a short literature review is presented. The literature review presents a few known designs

for various polarization transformations. The main emphasis is given to CPSS and polarization rotator designs as these two groups will be studied in more detail in later sections. The scientifically new content starts at Section 3 where the dyadic reflection and transmission coefficients are derived for a periodical array of the most generic bianisotropic scatterers. These coefficients act as linear mappings from the incident field into the reflected or transmitted fields. The reflection and transmission dyadics are applied in Section 4 to synthesize polarizabilities of particles that, when ordered into a periodical lattice, exhibit the desired polarization-related operations. As an example, the geometry and the approximate dimensions for a CPSS and a twist polarizer are developed. In Section 5 the method is slightly modified to enable only uniaxial polarizabilities of the particles in the array. The previously discussed twist polarizer is then re-synthesized with this simplified notation.

Section 6 verifies the operation of the previously synthesized CPSS with numerical simulations and with an analytical model showing good correspondence with the predicted behavior. The geometry is then modified to enable printed circuit board (PCB) manufacturing. However, certain properties, especially the polarization purity, are rather limited for practical applications and the experimental verification is not done for the CPSS. Similarly, the operation of the developed twist polarizer is verified in Section 7 with numerical simulations and experimental measurements. The numerical simulations are first done for an idealized structure showing very good correspondence with the theoretical predictions. Again, the geometry is modified to allow PCB manufacturing. The resulting prototype is optimized, manufactured, and finally measured. The experimental results show good correspondence with the simulations.

2 Polarization transformations, literature overview

The art of polarization transformations is old and much studied. The first examples of optically active materials, i.e., materials that rotate the plane of polarization, include certain crystals, such as quartz and solid gypsum, and also some isotropic media, such as turpentine gas. They were first studied by French scientists Arago (1811) and Biot (1812) [4, 12]. The first experimental verification of the same effect on microwave frequencies was done by Karl F. Lindman in 1920. Lindman studied randomly oriented helices and noted that they indeed rotate the plane of polarization [13]. A helix is a simple example of a chiral object, i.e., object that is not identical to its mirror image [14].

In addition to the polarization rotation, also polarization selectivity can be found in the nature, even if it might seem a highly complex operation. The reflection from the exoskeleton of a beetle Chrysina gloriosa depends strongly on the handedness of the incident light [15], as shown in Fig. 1. The polarization selectivity is caused by the chiral structure of the cells in the exoskeleton.

This section will present more recent studies and practical designs of different polarization transformers. The emphasis is on polarization selectivity and polarization rotation, as these will be studied in greater detail in this thesis. The properties of general chiral media have been studied extensively [4, 11, 16, 17]. However, as the main interest of this thesis is in thin sheets, the results of these studies are not presented here.

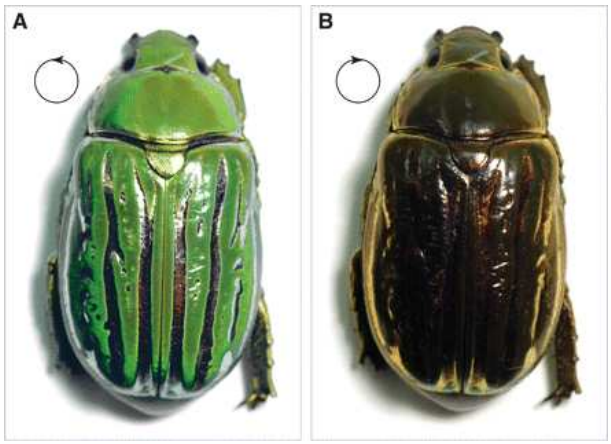

Figure 1: The exoskeleton of Chrysina gloriosa reflects the (a) left-hand circular polarized (LHCP) or unpolarized light differently than (b) right-hand circular polarized (RHCP) light. Figure from [15].

2.1 Circular polarization selective surfaces

There is a wide variety of man-made structures suitable for realization of a CPSS, a device that selects circular polarization. For some reason, most papers describing these designs are considering only the reflected and transmitted power — either the total power or the power of the specific polarization component. The axial ratio (AR) of the reflected or transmitted wave is often not shown, although this measure is, of course, crucial for practical applications.

Probably the earliest CPSS was reported by Pierrot in 1966 [18]. The design comprises an array of bent wires, each of which has the length of the wavelength in free space (λ_0) [19]. The geometry is illustrated in Fig. 2(a). Each wire is bent so that it has two $3\lambda_0/8$ long horizontal arms that are separated by a $2\lambda_0/8$ long vertical wire. While illuminated with a LHCP wave, the currents induced in the arms of the wire are in phase and create strong reflection, whereas with RHCP illumination the currents are out of phase and cancel each other, causing only a small effect on the plane wave. The structure was later studied by Morin [20]. These results are shown in Fig. 2(b) showing the relative -3 dB bandwidth of 17%. The same design was studied also by Roy [21] who noted that the axial ratio is very close to 1, i.e. circular, for normal incidence. However, the angular stability is not very good.

Another CPSS design, Tilston's cell, is based on two orthogonal dipoles that are connected by a $\lambda_0/4$ long transmission line whose electrical length is $\lambda_0/2$. The difference between physical and electrical lengths is achieved by using a dielectric material, having enough high permittivity, in the transmission line. The geometry is shown in Fig. 3(a) and the transmission coefficient for LHCP illumination in Fig. 3(b). The -3 dB bandwidth is almost 40% [22].

The aforementioned designs really work as a polarization selective surface for CP, but there are some difficulties related to the manufacturing process in both designs [23, 24]. In Pierrot's design [18] the vias penetrating the PCB are not easy to manufacture accurately enough for high frequencies. On the other hand,

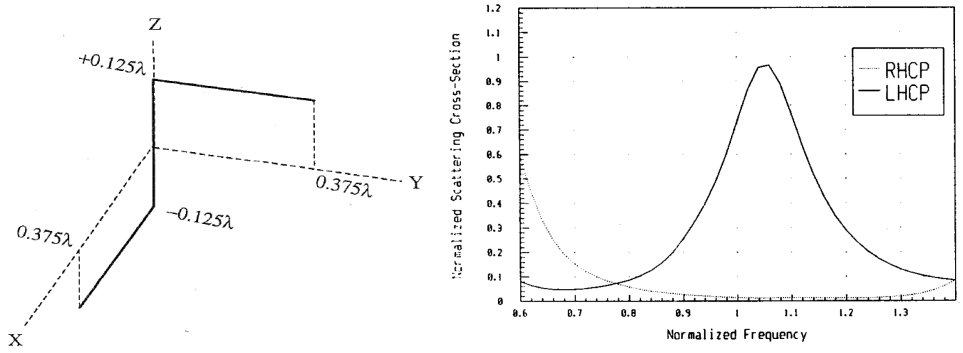

(a) (b)

Figure 2: (a) The geometry of the LHCP Pierrot's cell (Figure from [19]). (b) The results for a similar structure, LHCP-wave is almost fully reflected whereas the RHCP wave is transmitted. Figure from [20].

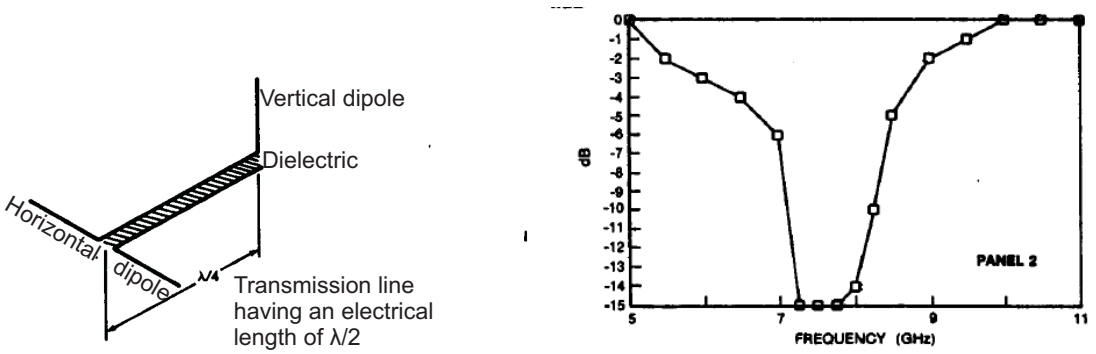

(a) (b)

Figure 3: (a) The geometry of Tilston's cell. (b) The insertion loss for Tilston's cell with LHCP illumination. Both from [22].

Tilston's design [22] relies on a transmission line, made of a substrate with different permittivity. These difficulties can be overcome if the design is made in three layers as suggested in [24]. The geometry can be seen in Fig. 4. The layer in the middle contains an "L"-shaped microstrip trace enabling capacitive coupling between the dipole elements.

The results for this three-layered structure can be seen in Fig. 5. The isolation is defined as the ratio of LHCP field measured with and without the left-hand circular polarization selective surface (LHCPSS) when the incident wave is LHCP [24]. Therefore, the isolation for a lossless surface roughly corresponds to the inverse of the reflection loss for RHCP used later in this thesis (note that this design has the opposite polarization from our design). Similarly, the transmission loss is defined as the power lost when a RHCP wave is transmitted through the surface [24]. In a lossless case, this corresponds to the transmission loss for LHCP in our design and also takes the polarization mismatch into account. This measure is practical, as it is enough to measure only the transmitted field. The obvious downside is that the properties of the reflected wave are neglected. The simulated -3 dB bandwidth for isolation is found to be 8.5%. These numbers, however, are not fully comparable to the other designs as the losses are taken into account and the definitions vary.

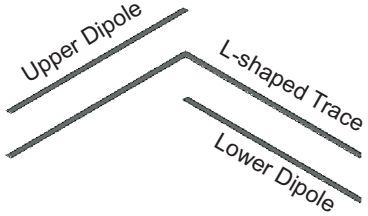

Figure 4: The geometry for Tarn's three-layered CPSS structure. Figure from [24].

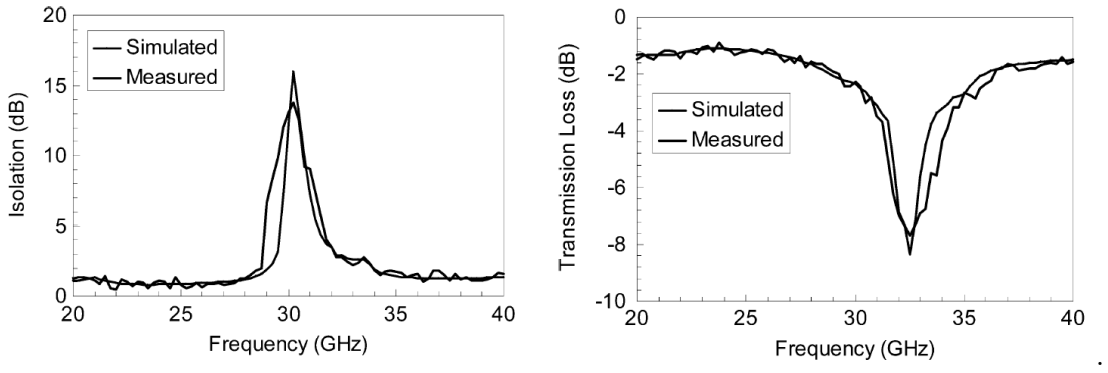

(a) (b)

Figure 5: The results for the Tarn's three-layered surface [24]: (a) isolation, (b) transmission loss.

2.2 LP to CP polarizers

Theoretically, every CPSS also transforms LP to CP: a LP plane wave can always be divided into equally strong LHCP and RHCP parts [4]. An ideal CPSS would reflect, e.g., the right handed component and allow the LHCP to pass through. Both transmitted and reflected waves would therefore be CP. The downside is that half of the incident total power would be lost in reflection. LP to CP polarizers have a wide variety of possible applications, e.g., in millimeter and sub-millimeter wave imaging [25], antennas [26], and in creating different microwave components [25].

One practical example of a planar linear to circular polarizer is a set of two orthogonal slots in a metallic screen. One of the slots is slightly longer than $\lambda_0/2$ and the other is slightly shorter. The longer slot corresponds to inductive path and the shorter slot a capacitive path causing phase difference between the two transmitted components [27]. Ideally, two orthogonal field components have 90° phase shift and equal magnitudes. The handedness and ellipticity of the transmitted wave is determined by the polarization plane of the incident wave. If the incident electric field is parallel to either of the slots, the transmitted field will be linearly polarized. Ideally, the incident field is slanted 45° in relation to the slots to produce pure CP.

In [26] the authors utilize an array of dipoles to obtain a LP to CP conversion for the reflected wave. The resulting design has a very low profile and still exhibits the good purity of polarization over a very large bandwidth. As the design is backed by a copper ground plane, there are no losses due to transmission [26]. In [28] the authors model ultrathin LP to CP polarizer under oblique incidence with certain effective polarizabilities.

2.3 Polarization rotators

A polarization rotator is a device that rotates the polarization plane of a LP plane wave. A twist polarizer is a polarization rotator with a 90° rotation angle. As previously discussed, the first experiments on man-made chirality were polarization rotators when Karl F. Lindman demonstrated that a box, filled with randomly oriented helices, rotates the polarization plane of a propagating wave [13]. The polarization rotation was noticed to be proportional to the thickness of the chiral slab and to the density of helices.

The traditional way of creating a planar polarization rotator is a stack of wire-grid polarizers whose wires are oriented in different directions in different layers [8, 29]. A wire-grid polarizer is an array of parallel conducting wires. In a wire-grid polarizer, the component of the incident wave that is polarized along the wires is reflected and the perpendicular component is transmitted [30]. A polarization rotator made of wire-grid polarizers has a low transmission loss and wide bandwidth but it works only for a certain polarization of the incident field [29]. As the wires of two consecutive layers are almost parallel, the reflected component of the field has multiple reflections between the wires. The transmission loss can then be minimized by tuning the distance between the layers [29].

The idea of creating chiral polarization rotators with non-contacting layers was first suggested probably in [31]. The design presented in [31] is based on simple, short strips that are slightly rotated in different layers. The inductive coupling between strips is used to create chirality without galvanic connection. The geometry of the proposed design is shown in Fig. 6.

A stack of slightly tilted gammadion shaped rosettes, as in Fig. 7, can be used to rotate the polarization plane [10]. The structure has two resonances in which the polarization rotation is very strong. Between these two resonances, the polarization is rotated approximately 7° with very low transmission loss. An useful figure of merit for a twist polarizer is the rotation per wavelength λ_0. As the thickness of this design is only $\lambda_0/30$, the rotation per wavelength is $250°/\lambda_0$ [10].

Another bi-layered twist polarizer was presented in [32]. On both layers of the design, there are four rectangular patches forming a square. The structure's four-

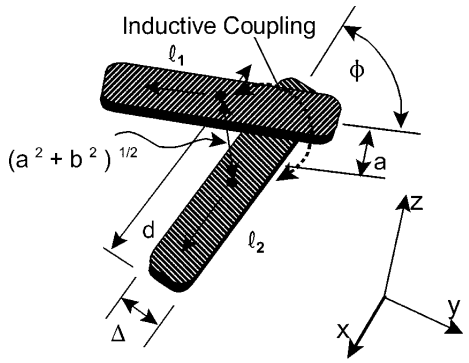

Figure 6: Two strips with inductive coupling rotates the polarization plane. Figure from [31].

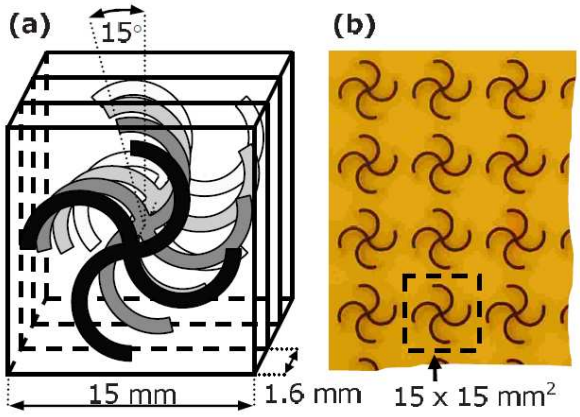

Figure 7: Four stacked rosettes exhibiting optical activity. Figure from [10].

fold rotational symmetry causes isotropy in the plane meaning that a LP wave with any polarization state would be rotated equally much. The design twists the polarization 90° and is only $\lambda_0/30$ thick, meaning that the rotation per wavelength is $2700°/\lambda_0$ [32]. This is the largest value that we have found in the literature.

These designs are based on resonant structures and their bandwidth tends to be rather limited. For more wideband operations, one can use stacked split ring resonators as in [33]. The relative bandwidth is 24% and reflections are very small. However, similarly to the wire-grid polarizers, the design works only for specific polarization state of the incident wave and electrical thickness of the device is usually significant.

3 Reflection and transmission from a bianisotropic array

In this section, dyadic reflection and transmission coefficients for an array of general bianisotropic particles are derived. The method is based on a group of polarizabilities for a single electrically small scatterer. Identical scatterers form a regular square array with the lattice constant a. The model comprises only tangential dyadics, meaning that the method is applicable for the normal incidence only. We assume that the array's period is smaller than the free space wavelength, so that no higer-order propagating waves are created. The time dependence is of the form $e^{j\omega t}$ and this term is omitted for clarity reasons. Later in this thesis, the resulting expressions for reflection and transmission are used to analytically synthesize different polarization related operations.

Dyads are dyadic products of two vectors $\mathbf{a}$ and $\mathbf{b}$, denoted by $\mathbf{ab}$. The dyadics are polynomials of dyads and describe linear relations between vectors [34]. For example, the dot product of a dyad $\mathbf{ab}$ and a vector $\mathbf{c}$ is a vector whose direction and length is defined as follows:

$$\mathbf{ab} \cdot \mathbf{c} = \mathbf{a}(\mathbf{b} \cdot \mathbf{c}) \tag{1}$$

$$\mathbf{c} \cdot \mathbf{ab} = (\mathbf{c} \cdot \mathbf{a})\mathbf{b} \tag{2}$$

Here $(\mathbf{b} \cdot \mathbf{c})$ and $(\mathbf{c} \cdot \mathbf{a})$ are, of course, scalars multiplying vectors. Note that the products involving dyadics are not generally commutative, i.e., the order of multiplication is significant. The cross product that defines a new dyad can be defined similarly:

$$\mathbf{ab} \times \mathbf{c} = \mathbf{a}(\mathbf{b} \times \mathbf{c}) \tag{3}$$

$$\mathbf{a} \times \mathbf{bc} = (\mathbf{a} \times \mathbf{b})\mathbf{c} \tag{4}$$

Dot product of two dyads produces a new dyad and is defined as:

$$\mathbf{ab} \cdot \mathbf{cd} = \mathbf{a}(\mathbf{b} \cdot \mathbf{c})\mathbf{d} = (\mathbf{b} \cdot \mathbf{c})\mathbf{ad} \tag{5}$$

Unit dyadic $\overline{\overline{\mathrm{I}}}$ is the identity element in the dot-product algebra: $\overline{\overline{\mathrm{I}}} \cdot \mathbf{a} = \mathbf{a}$ for any $\mathbf{a}$ [34]. The inverse of a dyadic $\overline{\overline{\mathrm{A}}}$ is denoted $\left(\overline{\overline{\mathrm{A}}}\right)^{-1}$ and is defined in terms of $\overline{\overline{\mathrm{I}}}$ so that [34]

$$\overline{\overline{\mathrm{A}}} \cdot \left(\overline{\overline{\mathrm{A}}}\right)^{-1} = \overline{\overline{\mathrm{I}}} \tag{6}$$

The cross product of a vector and a unit dyadic corresponds to a 90° rotation around that vector. For example, vector $\hat{\mathbf{x}}$ is rotated around $\hat{\mathbf{z}}$:

$$\begin{aligned}(\hat{\mathbf{z}} \times \overline{\overline{\mathrm{I}}}) \cdot \hat{\mathbf{x}} &= (\hat{\mathbf{z}} \times \hat{\mathbf{x}}\hat{\mathbf{x}} + \hat{\mathbf{z}} \times \hat{\mathbf{y}}\hat{\mathbf{y}} + \hat{\mathbf{z}} \times \hat{\mathbf{z}}\hat{\mathbf{z}}) \cdot \hat{\mathbf{x}} \\ &= (\hat{\mathbf{y}}\hat{\mathbf{x}} - \hat{\mathbf{x}}\hat{\mathbf{y}} + 0) \cdot \hat{\mathbf{x}} = \hat{\mathbf{y}}\end{aligned} \tag{7}$$

The transpose of a dyadic is defined as:

$$(\mathbf{ab})^T = \mathbf{ba} \tag{8}$$

3.1 Dyadic reflection and transmission coefficients

The model presented in this section is based on polarizability dyadics that define the linear relations between the local fields (at the location of an electrically small particle) and the induced dipole moments as follows [1]:

$$\begin{bmatrix} \mathbf{p} \\ \mathbf{m} \end{bmatrix} = \begin{bmatrix} \overline{\overline{\alpha}}_{\mathrm{ee}} & \overline{\overline{\alpha}}_{\mathrm{em}} \\ \overline{\overline{\alpha}}_{\mathrm{me}} & \overline{\overline{\alpha}}_{\mathrm{mm}} \end{bmatrix} \cdot \begin{bmatrix} \mathbf{E}_{\mathrm{loc}} \\ \mathbf{H}_{\mathrm{loc}} \end{bmatrix} \tag{9}$$

The illuminating plane wave is oriented towards the plane, i.e., the wave vector $\mathbf{k}_{\mathrm{inc}}$ and the surface normal $\hat{\mathbf{n}}$ are antiparallel. The local fields $\mathbf{E}_{\mathrm{loc}}$ and $\mathbf{H}_{\mathrm{loc}}$ are the sums of the incident field and the interaction field caused by the induced dipole moments in all particles:

$$\mathbf{E}_{\mathrm{loc}} = \mathbf{E}_{\mathrm{inc}} + \overline{\overline{\beta}}_{\mathrm{e}} \cdot \mathbf{p} \tag{10}$$

$$\mathbf{H}_{\mathrm{loc}} = \mathbf{H}_{\mathrm{inc}} + \overline{\overline{\beta}}_{\mathrm{m}} \cdot \mathbf{m} \tag{11}$$

Here $\overline{\overline{\beta}}_{\mathrm{e}}$ and $\overline{\overline{\beta}}_{\mathrm{m}}$ are the tangential components of the interaction term that describes the effect of the entire array on a single inclusion. Approximate expressions for the real parts and exact values for the imaginary parts can be found to be [1, 35]:

$$\overline{\overline{\beta}}_{\mathrm{e}} = -\Re\left\{\frac{j\omega\eta_0}{4S}\left(1-\frac{1}{jkR}\right)\exp(-jkR)\overline{\overline{\mathrm{I}}}_{\mathrm{t}}\right\} + \left(j\frac{\eta_0\epsilon_0\mu_0\omega^3}{6\pi} - j\frac{\eta_0\omega}{2S}\right)\overline{\overline{\mathrm{I}}}_{\mathrm{t}} \tag{12}$$

$$\overline{\overline{\beta}}_{\mathrm{m}} = \frac{\overline{\overline{\beta}}_{\mathrm{e}}}{\eta_0^2} \tag{13}$$

Here a denotes the lattice constant of a square array, $R = a/1.438$, and $\overline{\overline{\mathrm{I}}}_{\mathrm{t}} = \overline{\overline{\mathrm{I}}} - \hat{\mathbf{n}}\hat{\mathbf{n}} = \hat{\mathbf{x}}\hat{\mathbf{x}} + \hat{\mathbf{y}}\hat{\mathbf{y}}$ is the tangential unit dyadic. The approximate expression for the real part of the interaction dyadic is applicable only for $ka < 1.5 \ldots 2$ [35]. As all of the dipoles are at the same plane, the induced magnetic dipoles do not cause electric interaction field and vice versa. Thus, there are no cross beta terms ($\overline{\overline{\beta}}_{\mathrm{em}}$, $\overline{\overline{\beta}}_{\mathrm{me}}$) [35].

As we want to use as general particles as possible, no assumptions are made about reciprocity or losses. The individual polarizability dyadics have the following general forms:

$$\overline{\overline{\alpha}}_{\mathrm{ee}} = \alpha_{\mathrm{ee}}^{xx}\hat{\mathbf{x}}\hat{\mathbf{x}} + \alpha_{\mathrm{ee}}^{xy}\hat{\mathbf{x}}\hat{\mathbf{y}} + \alpha_{\mathrm{ee}}^{yx}\hat{\mathbf{y}}\hat{\mathbf{x}} + \alpha_{\mathrm{ee}}^{yy}\hat{\mathbf{y}}\hat{\mathbf{y}} \tag{14}$$

$$\overline{\overline{\alpha}}_{\mathrm{em}} = \alpha_{\mathrm{em}}^{xx}\hat{\mathbf{x}}\hat{\mathbf{x}} + \alpha_{\mathrm{em}}^{yy}\hat{\mathbf{y}}\hat{\mathbf{y}} + \alpha_{\mathrm{em}}^{xy}\hat{\mathbf{x}}\hat{\mathbf{y}} + \alpha_{\mathrm{em}}^{yx}\hat{\mathbf{y}}\hat{\mathbf{x}} \tag{15}$$

$$\overline{\overline{\alpha}}_{\mathrm{me}} = \alpha_{\mathrm{me}}^{xx}\hat{\mathbf{x}}\hat{\mathbf{x}} + \alpha_{\mathrm{me}}^{yy}\hat{\mathbf{y}}\hat{\mathbf{y}} + \alpha_{\mathrm{me}}^{xy}\hat{\mathbf{x}}\hat{\mathbf{y}} + \alpha_{\mathrm{me}}^{yx}\hat{\mathbf{y}}\hat{\mathbf{x}} \tag{16}$$

$$\overline{\overline{\alpha}}_{\mathrm{mm}} = \alpha_{\mathrm{mm}}^{xx}\hat{\mathbf{x}}\hat{\mathbf{x}} + \alpha_{\mathrm{mm}}^{xy}\hat{\mathbf{x}}\hat{\mathbf{y}} + \alpha_{\mathrm{mm}}^{yx}\hat{\mathbf{y}}\hat{\mathbf{x}} + \alpha_{\mathrm{mm}}^{yy}\hat{\mathbf{y}}\hat{\mathbf{y}} \tag{17}$$

The $\hat{\mathbf{n}}$ directed dipole moments do not affect the reflection or transmission with normal incidence and the corresponding polarizability terms are thus omitted.

3.2 Effective polarizabilities

For the most general polarizabilities, it is not easy to solve the induced dipole moments $\mathbf{p}$ and $\mathbf{m}$ from equations (9), (10) and (11). However, the calculations

can be simplified by using effective polarizabilities, denoted with hatted symbols. These effective polarizabilities are functions of the particle polarizabilities and the interaction dyadics and act as linear relations between the dipole moments and the incident fields:

$$\left[\begin{array}{c}\mathbf{p}\\ \mathbf{m}\end{array}\right]=\left[\begin{array}{cc}\overline{\overline{\widehat{\alpha}}}_{\mathrm{ee}} & \overline{\overline{\widehat{\alpha}}}_{\mathrm{em}}\\ \overline{\overline{\widehat{\alpha}}}_{\mathrm{me}} & \overline{\overline{\widehat{\alpha}}}_{\mathrm{mm}}\end{array}\right]\cdot\left[\begin{array}{c}\mathbf{E}_{\mathrm{inc}}\\ \mathbf{H}_{\mathrm{inc}}\end{array}\right] \tag{18}$$

Since the interaction with neighboring inclusions cannot create any new dipole moments, these effective polarizabilities have the same components as the individual ones. The effective polarizability dyadics have the same generic forms:

$$\overline{\overline{\widehat{\alpha}}}_{\mathrm{ee}}=\widehat{\alpha}_{\mathrm{ee}}^{xx}\hat{\mathbf{x}}\hat{\mathbf{x}}+\widehat{\alpha}_{\mathrm{ee}}^{xy}\hat{\mathbf{x}}\hat{\mathbf{y}}+\widehat{\alpha}_{\mathrm{ee}}^{yx}\hat{\mathbf{y}}\hat{\mathbf{x}}+\widehat{\alpha}_{\mathrm{ee}}^{yy}\hat{\mathbf{y}}\hat{\mathbf{y}} \tag{19}$$

$$\overline{\overline{\widehat{\alpha}}}_{\mathrm{em}}=\widehat{\alpha}_{\mathrm{em}}^{xx}\hat{\mathbf{x}}\hat{\mathbf{x}}+\widehat{\alpha}_{\mathrm{em}}^{xy}\hat{\mathbf{x}}\hat{\mathbf{y}}+\widehat{\alpha}_{\mathrm{em}}^{yx}\hat{\mathbf{y}}\hat{\mathbf{x}}+\widehat{\alpha}_{\mathrm{em}}^{yy}\hat{\mathbf{y}}\hat{\mathbf{y}} \tag{20}$$

$$\overline{\overline{\widehat{\alpha}}}_{\mathrm{me}}=\widehat{\alpha}_{\mathrm{me}}^{xx}\hat{\mathbf{x}}\hat{\mathbf{x}}+\widehat{\alpha}_{\mathrm{me}}^{xy}\hat{\mathbf{x}}\hat{\mathbf{y}}+\widehat{\alpha}_{\mathrm{me}}^{yx}\hat{\mathbf{y}}\hat{\mathbf{x}}+\widehat{\alpha}_{\mathrm{me}}^{yy}\hat{\mathbf{y}}\hat{\mathbf{y}} \tag{21}$$

$$\overline{\overline{\widehat{\alpha}}}_{\mathrm{mm}}=\widehat{\alpha}_{\mathrm{mm}}^{xx}\hat{\mathbf{x}}\hat{\mathbf{x}}+\widehat{\alpha}_{\mathrm{mm}}^{xy}\hat{\mathbf{x}}\hat{\mathbf{y}}+\widehat{\alpha}_{\mathrm{mm}}^{yx}\hat{\mathbf{y}}\hat{\mathbf{x}}+\widehat{\alpha}_{\mathrm{mm}}^{yy}\hat{\mathbf{y}}\hat{\mathbf{y}} \tag{22}$$

As mentioned before, the effective polarizabilities $\overline{\overline{\widehat{\alpha}}}_{\mathrm{ee}},\overline{\overline{\widehat{\alpha}}}_{\mathrm{em}},\overline{\overline{\widehat{\alpha}}}_{\mathrm{me}}$, and $\overline{\overline{\widehat{\alpha}}}_{\mathrm{mm}}$ are functions of particle polarizabilities and the interaction constants $\overline{\overline{\beta}}_{\mathrm{e}}$ and $\overline{\overline{\beta}}_{\mathrm{m}}$. In the following, we will find the exact expressions for the general effective polarizabilities, writing:

$$\begin{aligned}\mathbf{p}&=\overline{\overline{\alpha}}_{\mathrm{ee}}\left(\mathbf{E}_{\mathrm{inc}}+\overline{\overline{\beta}}_{\mathrm{e}}\cdot\mathbf{p}\right)+\overline{\overline{\alpha}}_{\mathrm{em}}\left(\mathbf{H}_{\mathrm{inc}}+\overline{\overline{\beta}}_{\mathrm{m}}\cdot\mathbf{m}\right)\\&=\left(\overline{\overline{\mathrm{I}}}-\overline{\overline{\alpha}}_{\mathrm{ee}}\cdot\overline{\overline{\beta}}_{\mathrm{e}}\right)^{-1}\left[\overline{\overline{\alpha}}_{\mathrm{ee}}\cdot\mathbf{E}_{\mathrm{inc}}+\overline{\overline{\alpha}}_{\mathrm{em}}\left(\mathbf{H}_{\mathrm{inc}}+\overline{\overline{\beta}}_{\mathrm{m}}\cdot\mathbf{m}\right)\right]\end{aligned} \tag{23}$$

$$\mathbf{m}=\overline{\overline{\alpha}}_{\mathrm{me}}\left(\mathbf{E}_{\mathrm{inc}}+\overline{\overline{\beta}}_{\mathrm{e}}\cdot\mathbf{p}\right)+\overline{\overline{\alpha}}_{\mathrm{mm}}\left(\mathbf{H}_{\mathrm{inc}}+\overline{\overline{\beta}}_{\mathrm{m}}\cdot\mathbf{m}\right) \tag{24}$$

By substituting $\mathbf{p}$ from equation (23), (24) can be re-written in the following form:

$$\begin{aligned}&\mathbf{m}-\overline{\overline{\alpha}}_{\mathrm{me}}\cdot\overline{\overline{\beta}}_{\mathrm{e}}\cdot\left(\overline{\overline{\mathrm{I}}}_{\mathrm{t}}-\overline{\overline{\alpha}}_{\mathrm{ee}}\cdot\overline{\overline{\beta}}_{\mathrm{e}}\right)^{-1}\cdot\overline{\overline{\alpha}}_{\mathrm{em}}\cdot\overline{\overline{\beta}}_{\mathrm{m}}\cdot\mathbf{m}-\overline{\overline{\alpha}}_{\mathrm{mm}}\cdot\overline{\overline{\beta}}_{\mathrm{m}}\cdot\mathbf{m}\\&=\overline{\overline{\alpha}}_{\mathrm{me}}\cdot\mathbf{E}_{\mathrm{inc}}+\overline{\overline{\alpha}}_{\mathrm{me}}\cdot\overline{\overline{\beta}}_{\mathrm{e}}\cdot\left(\overline{\overline{\mathrm{I}}}_{\mathrm{t}}-\overline{\overline{\alpha}}_{\mathrm{ee}}\cdot\overline{\overline{\beta}}_{\mathrm{e}}\right)^{-1}\overline{\overline{\alpha}}_{\mathrm{ee}}\cdot\mathbf{E}_{\mathrm{inc}}\\&\quad+\overline{\overline{\alpha}}_{\mathrm{me}}\cdot\overline{\overline{\beta}}_{\mathrm{e}}\cdot\left(\overline{\overline{\mathrm{I}}}_{\mathrm{t}}-\overline{\overline{\alpha}}_{\mathrm{ee}}\cdot\overline{\overline{\beta}}_{\mathrm{e}}\right)^{-1}\overline{\overline{\alpha}}_{\mathrm{em}}\cdot\mathbf{H}_{\mathrm{inc}}+\overline{\overline{\alpha}}_{\mathrm{mm}}\cdot\mathbf{H}_{\mathrm{inc}}\end{aligned} \tag{25}$$

From this equation, it is trivial to solve the induced magnetic dipole moment as the function of the incident electric and magnetic fields, i.e., polarizabilities $\overline{\overline{\widehat{\alpha}}}_{\mathrm{me}}$ and $\overline{\overline{\widehat{\alpha}}}_{\mathrm{mm}}$ respectively. Electric dipole moment $\mathbf{p}$ can be treated similarly.

Finally, the effective tangential polarizabilities for a square array of the most general bianisotropic particles read as follows:

$$\begin{aligned}\overline{\overline{\widehat{\alpha}}}_{\mathrm{ee}}=&\left(\overline{\overline{\mathrm{I}}}_{\mathrm{t}}-\overline{\overline{\alpha}}_{\mathrm{ee}}\cdot\overline{\overline{\beta}}_{\mathrm{e}}-\overline{\overline{\alpha}}_{\mathrm{em}}\cdot\overline{\overline{\beta}}_{\mathrm{m}}\cdot\left(\overline{\overline{\mathrm{I}}}_{\mathrm{t}}-\overline{\overline{\alpha}}_{\mathrm{mm}}\cdot\overline{\overline{\beta}}_{\mathrm{m}}\right)^{-1}\cdot\overline{\overline{\alpha}}_{\mathrm{me}}\cdot\overline{\overline{\beta}}_{\mathrm{e}}\right)^{-1}\\&\cdot\left(\overline{\overline{\alpha}}_{\mathrm{ee}}+\overline{\overline{\alpha}}_{\mathrm{em}}\cdot\ \overline{\overline{\beta}}_{\mathrm{m}}\cdot\left(\overline{\overline{\mathrm{I}}}_{\mathrm{t}}-\overline{\overline{\alpha}}_{\mathrm{mm}}\cdot\overline{\overline{\beta}}_{\mathrm{m}}\right)^{-1}\cdot\overline{\overline{\alpha}}_{\mathrm{me}}\right)\end{aligned} \tag{26}$$

$$\overline{\overline{\widehat{\alpha}}}_{\mathrm{em}} = \left(\overline{\overline{\mathrm{I}}}_{\mathrm{t}} - \overline{\overline{\alpha}}_{\mathrm{ee}} \cdot \overline{\overline{\beta}}_{\mathrm{e}} - \overline{\overline{\alpha}}_{\mathrm{em}} \cdot \overline{\overline{\beta}}_{\mathrm{m}} \cdot \left(\overline{\overline{\mathrm{I}}}_{\mathrm{t}} - \overline{\overline{\alpha}}_{\mathrm{mm}} \cdot \overline{\overline{\beta}}_{\mathrm{m}}\right)^{-1} \cdot \overline{\overline{\alpha}}_{\mathrm{me}} \cdot \overline{\overline{\beta}}_{\mathrm{e}}\right)^{-1} \cdot \left(\overline{\overline{\alpha}}_{\mathrm{em}} + \overline{\overline{\alpha}}_{\mathrm{em}} \cdot \ \overline{\overline{\beta}}_{\mathrm{m}} \cdot \left(\overline{\overline{\mathrm{I}}}_{\mathrm{t}} - \overline{\overline{\alpha}}_{\mathrm{mm}} \cdot \overline{\overline{\beta}}_{\mathrm{m}}\right)^{-1} \cdot \overline{\overline{\alpha}}_{\mathrm{mm}}\right) \tag{27}$$

$$\overline{\overline{\widehat{\alpha}}}_{\mathrm{me}} = \left(\overline{\overline{\mathrm{I}}}_{\mathrm{t}} - \overline{\overline{\alpha}}_{\mathrm{me}} \cdot \overline{\overline{\beta}}_{\mathrm{e}} \cdot \left(\overline{\overline{\mathrm{I}}}_{\mathrm{t}} - \overline{\overline{\alpha}}_{\mathrm{ee}} \cdot \overline{\overline{\beta}}_{\mathrm{e}}\right)^{-1} \cdot \overline{\overline{\alpha}}_{\mathrm{em}} \cdot \overline{\overline{\beta}}_{\mathrm{m}} - \overline{\overline{\alpha}}_{\mathrm{mm}} \cdot \overline{\overline{\beta}}_{\mathrm{m}}\right)^{-1} \cdot \left(\overline{\overline{\alpha}}_{\mathrm{me}} + \overline{\overline{\alpha}}_{\mathrm{me}} \cdot \overline{\overline{\beta}}_{\mathrm{e}} \cdot \left(\overline{\overline{\mathrm{I}}}_{\mathrm{t}} - \overline{\overline{\alpha}}_{\mathrm{ee}} \cdot \overline{\overline{\beta}}_{\mathrm{e}}\right)^{-1} \overline{\overline{\alpha}}_{\mathrm{ee}}\right) \tag{28}$$

$$\overline{\overline{\widehat{\alpha}}}_{\mathrm{mm}} = \left(\overline{\overline{\mathrm{I}}}_{\mathrm{t}} - \overline{\overline{\alpha}}_{\mathrm{me}} \cdot \overline{\overline{\beta}}_{\mathrm{e}} \cdot \left(\overline{\overline{\mathrm{I}}}_{\mathrm{t}} - \overline{\overline{\alpha}}_{\mathrm{ee}} \cdot \overline{\overline{\beta}}_{\mathrm{e}}\right)^{-1} \cdot \overline{\overline{\alpha}}_{\mathrm{em}} \cdot \overline{\overline{\beta}}_{\mathrm{m}} - \overline{\overline{\alpha}}_{\mathrm{mm}} \cdot \overline{\overline{\beta}}_{\mathrm{m}}\right)^{-1} \cdot \left(\overline{\overline{\alpha}}_{\mathrm{me}} \cdot \overline{\overline{\beta}}_{\mathrm{e}} \cdot \left(\overline{\overline{\mathrm{I}}}_{\mathrm{t}} - \overline{\overline{\alpha}}_{\mathrm{ee}} \cdot \overline{\overline{\beta}}_{\mathrm{e}}\right)^{-1} \overline{\overline{\alpha}}_{\mathrm{em}} + \overline{\overline{\alpha}}_{\mathrm{mm}}\right) \tag{29}$$

In a plane wave, the electric and magnetic fields are related:

$$\mathbf{H}_{\mathrm{inc}} = \frac{\mathbf{k}_{\mathrm{inc}} \times \mathbf{E}_{\mathrm{inc}}}{\mu_0 \omega} \tag{30}$$

With the help of the tangential unit dyadic $\overline{\overline{\mathrm{I}}}_{\mathrm{t}}$, the incident magnetic field $\mathbf{H}_{\mathrm{inc}}$ in (18) can be presented as a function of the incident electric field $\mathbf{E}_{\mathrm{inc}}$ (remember that $\mathbf{k}_{\mathrm{inc}} \uparrow\uparrow -\hat{\mathbf{n}}$):

$$\mathbf{H}_{\mathrm{inc}} = \left(-\frac{1}{\eta_0}\hat{\mathbf{n}} \times \overline{\overline{\mathrm{I}}}_{\mathrm{t}}\right) \cdot \mathbf{E}_{\mathrm{inc}} \tag{31}$$

Now expression (18) for the induced electric and magnetic dipole moments simplifies into:

$$\begin{bmatrix} \mathbf{p} \\ \mathbf{m} \end{bmatrix} = \begin{bmatrix} \overline{\overline{\widehat{\alpha}}}_{\mathrm{ee}} & \overline{\overline{\widehat{\alpha}}}_{\mathrm{em}} \\ \overline{\overline{\widehat{\alpha}}}_{\mathrm{me}} & \overline{\overline{\widehat{\alpha}}}_{\mathrm{mm}} \end{bmatrix} \cdot \begin{bmatrix} \overline{\overline{\mathrm{I}}}_{\mathrm{t}} \\ -\frac{1}{\eta_0}\hat{\mathbf{n}} \times \overline{\overline{\mathrm{I}}}_{\mathrm{t}} \end{bmatrix} \cdot \mathbf{E}_{\mathrm{inc}} \tag{32}$$

$$\mathbf{p} = \left\{\overline{\overline{\widehat{\alpha}}}_{\mathrm{ee}} - \frac{1}{\eta_0}\overline{\overline{\widehat{\alpha}}}_{\mathrm{em}} \cdot \left(\hat{\mathbf{n}} \times \overline{\overline{\mathrm{I}}}_{\mathrm{t}}\right)\right\} \cdot \mathbf{E}_{\mathrm{inc}} \tag{33}$$

$$\mathbf{m} = \left\{\overline{\overline{\widehat{\alpha}}}_{\mathrm{me}} - \frac{1}{\eta_0}\overline{\overline{\widehat{\alpha}}}_{\mathrm{mm}} \cdot \left(\hat{\mathbf{n}} \times \overline{\overline{\mathrm{I}}}_{\mathrm{t}}\right)\right\} \cdot \mathbf{E}_{\mathrm{inc}} \tag{34}$$

3.3 The fields radiated by the induced currents

The dipole moments (33) and (34) correspond to a certain averaged surface currents $\mathbf{J}_{\mathrm{e}}$ and $\mathbf{J}_{\mathrm{m}}$ that radiate plane waves into free space. The radiation of an infinite sheet of electric or magnetic current can easily be solved from the Maxwell equations. The orientation of currents and fields can be seen in Fig. 8. The time-varying dipole

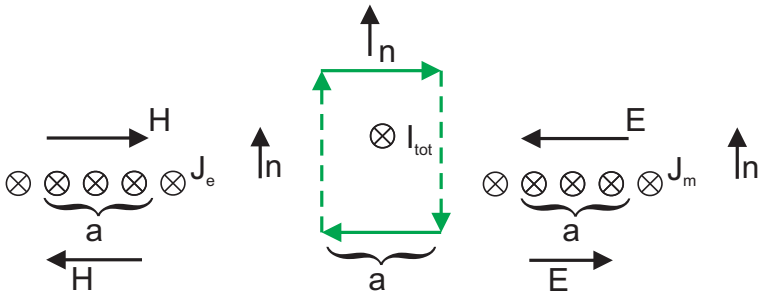

Figure 8: (a) Electric current $\mathbf{J}_\mathrm{e}$ and corresponding magnetic field $\mathbf{H}$. (b) The integration path C in green and the total current penetrating the path I_tot. Dashed green line corresponds to the integration path, along which the $\mathbf{H} \cdot \mathrm{d}\mathbf{l} = 0$. (c) Magnetic current $\mathbf{J}_\mathrm{m}$ and corresponding electric field $\mathbf{E}$.

moments correspond to a surface electric current density:

$$\mathbf{J}_\mathrm{e} = \frac{j\omega}{S}\mathbf{p} \tag{35}$$

where $S = a^2$ is the area of one unit cell. According to Ampère's law, the electric current creates a curl of magnetic field around it:

$$\nabla \times \mathbf{H} = \mathbf{J}_\mathrm{e} + j\omega\mathbf{D} \tag{36}$$

By using Stokes' theorem, we see that the path integral of the magnetic field corresponds to the total current flowing through the surface that is enclosed by the integration path:

$$\int_S (\nabla \times \mathbf{H}) \cdot \mathrm{d}\mathbf{S} = \int_S \mathbf{J}_\mathrm{e} \cdot \mathrm{d}\mathbf{S} \tag{37}$$

$$\oint_C \mathbf{H} \cdot \mathrm{d}\mathbf{l} = I_\mathrm{tot} \tag{38}$$

The surface integral of $j\omega\mathbf{D}$ tends to zero when the height of the integration area tends to zero.

As $\mathbf{H}$ is constant and parallel to the integration path, the integral simplifies into multiplication by the path length. Some parts of the path are orthogonal to the magnetic field, and that integral may be neglected. The total current I_tot can be calculated from the averaged surface current density just by multiplying it by the length a:

$$2a\,|\mathbf{H}| = a\,|\mathbf{J}_\mathrm{e}| \tag{39}$$

Again, in a plane wave the radiated magnetic field corresponds to the radiated electric field:

$$\mathbf{E} = -\frac{\mathbf{k}_0 \times \mathbf{H}}{\omega\epsilon_0} = -\eta_0 \hat{\mathbf{n}} \times \mathbf{H} \tag{40}$$

Finally, the electric field that is radiated by the effective surface current density simplifies into:

$$\mathbf{E} = -\frac{j\omega\eta_0}{2S}\mathbf{p} \tag{41}$$

This means that the reflected plane-wave field, caused by the induced electric dipole moments, is:

$$\mathbf{E}_\mathrm{r} = -\frac{j\omega\eta_0}{2S}\mathbf{p} \tag{42}$$

On the other side of the slab, the transmitted wave is the sum of the electric field caused by the induced dipoles and the incident field:

$$\mathbf{E}_\mathrm{t} = \mathbf{E}_\mathrm{inc} - \frac{j\omega\eta_0}{2S}\mathbf{p} \tag{43}$$

The fields, caused by magnetic dipoles, can be obtained similarly. First, the effective magnetic surface current reads $\mathbf{J}_\mathrm{m} = j\omega\mathbf{m}/S$. The magnetic current is always surrounded by a curl of electric field: $\nabla \times \mathbf{E} = -\mathbf{J}_\mathrm{m} - j\omega\mathbf{B}$. For an infinite sheet of this current, the field magnitude reads: $2a\,|\mathbf{E}| = a\,|\mathbf{J}_\mathrm{m}|$

From these equations, the magnitude of the electric field, caused by the induced magnetic current, can be solved to be:

$$|\mathbf{E}| = \frac{j\omega}{2S}\,|\mathbf{m}| \tag{44}$$

As this electric field is curled around the magnetic current, the direction of the field is opposite on the different sides of the sheet. In the abscence of electric dipole moments, the reflected field is:

$$\mathbf{E}_\mathrm{r} = \hat{\mathbf{n}} \times \left(\frac{j\omega}{2S}\mathbf{m}\right) \tag{45}$$

The transmitted field is the sum of incident field and the field caused by the magnetic current.

$$\mathbf{E}_\mathrm{t} = \mathbf{E}_\mathrm{inc} - \hat{\mathbf{n}} \times \left(\frac{j\omega}{2S}\mathbf{m}\right) \tag{46}$$

Finally, the total reflected field can be expressed as the sum of expressions (42) and (45):

$$\mathbf{E}_\mathrm{r} = -\frac{j\omega}{2S}\left[\eta_0\mathbf{p} - \hat{\mathbf{n}} \times \mathbf{m}\right] \tag{47}$$

$$= -\frac{j\omega}{2S}\left[\eta_0\overline{\overline{\alpha}}_\mathrm{ee} - \overline{\overline{\alpha}}_\mathrm{em} \times \hat{\mathbf{n}} - \hat{\mathbf{n}} \times \overline{\overline{\alpha}}_\mathrm{me} + \frac{1}{\eta_0}\hat{\mathbf{n}} \times \left(\overline{\overline{\alpha}}_\mathrm{mm} \times \hat{\mathbf{n}}\right)\right] \cdot \mathbf{E}_\mathrm{inc} \tag{48}$$

By substituting the effective polarizabilities with their component-wise forms (from

(19) – (22)) and re-arranging the terms, we get:

$$\begin{aligned}\mathbf{E}_{\mathrm{r}} = -\frac{j\omega}{2S}\Bigg[&\left(\eta_0\widehat{\alpha}_{\mathrm{ee}}^{xx} - \widehat{\alpha}_{\mathrm{em}}^{xy} + \widehat{\alpha}_{\mathrm{me}}^{yx} - \frac{1}{\eta_0}\widehat{\alpha}_{\mathrm{mm}}^{yy}\right)\hat{\mathbf{x}}\hat{\mathbf{x}} \\ &+ \left(\eta_0\widehat{\alpha}_{\mathrm{ee}}^{xy} + \widehat{\alpha}_{\mathrm{em}}^{xx} + \widehat{\alpha}_{\mathrm{me}}^{yy} + \frac{1}{\eta_0}\widehat{\alpha}_{\mathrm{mm}}^{yx}\right)\hat{\mathbf{x}}\hat{\mathbf{y}} \\ &+ \left(\eta_0\widehat{\alpha}_{\mathrm{ee}}^{yx} - \widehat{\alpha}_{\mathrm{em}}^{yy} - \widehat{\alpha}_{\mathrm{me}}^{xx} + \frac{1}{\eta_0}\widehat{\alpha}_{\mathrm{mm}}^{xy}\right)\hat{\mathbf{y}}\hat{\mathbf{x}} \\ &+ \left(\eta_0\widehat{\alpha}_{\mathrm{ee}}^{yy} + \widehat{\alpha}_{\mathrm{em}}^{yx} - \widehat{\alpha}_{\mathrm{me}}^{xy} - \frac{1}{\eta_0}\widehat{\alpha}_{\mathrm{mm}}^{xx}\right)\hat{\mathbf{y}}\hat{\mathbf{y}}\Bigg]\cdot\mathbf{E}_{\mathrm{inc}} \end{aligned} \tag{49}$$

Similarly, we can write the transmitted electric field as the sum of (43) and (46):

$$\mathbf{E}_{\mathrm{t}} = \mathbf{E}_{\mathrm{inc}} - \frac{j\omega}{2S}\left[\eta_0\mathbf{p} + \hat{\mathbf{n}}\times\mathbf{m}\right] \tag{50}$$

$$\begin{aligned}&= \left\{\bar{\bar{\mathrm{I}}}_{\mathrm{t}} - \frac{j\omega}{2S}\left[\eta_0\overline{\overline{\widehat{\alpha}}}_{\mathrm{ee}} - \overline{\overline{\widehat{\alpha}}}_{\mathrm{em}}\times\hat{\mathbf{n}} + \hat{\mathbf{n}}\times\overline{\overline{\widehat{\alpha}}}_{\mathrm{me}} - \frac{1}{\eta_0}\hat{\mathbf{n}}\times\left(\overline{\overline{\widehat{\alpha}}}_{\mathrm{mm}}\times\hat{\mathbf{n}}\right)\right]\right\}\cdot\mathbf{E}_{\mathrm{inc}} \\ &= \Bigg\{\left[1 - \frac{j\omega}{2S}\left(\eta_0\widehat{\alpha}_{\mathrm{ee}}^{xx} - \widehat{\alpha}_{\mathrm{em}}^{xy} - \widehat{\alpha}_{\mathrm{me}}^{yx} + \frac{1}{\eta_0}\widehat{\alpha}_{\mathrm{mm}}^{yy}\right)\right]\hat{\mathbf{x}}\hat{\mathbf{x}} \\ &\quad + \left[1 - \frac{j\omega}{2S}\left(\eta_0\widehat{\alpha}_{\mathrm{ee}}^{yy} + \widehat{\alpha}_{\mathrm{em}}^{yx} + \widehat{\alpha}_{\mathrm{me}}^{xy} + \frac{1}{\eta_0}\widehat{\alpha}_{\mathrm{mm}}^{xx}\right)\right]\hat{\mathbf{y}}\hat{\mathbf{y}} \\ &\quad - \frac{j\omega}{2S}\left(\eta_0\widehat{\alpha}_{\mathrm{ee}}^{yx} - \widehat{\alpha}_{\mathrm{em}}^{yy} + \widehat{\alpha}_{\mathrm{me}}^{xx} - \frac{1}{\eta_0}\widehat{\alpha}_{\mathrm{mm}}^{xy}\right)\hat{\mathbf{y}}\hat{\mathbf{x}} \\ &\quad - \frac{j\omega}{2S}\left(\eta_0\widehat{\alpha}_{\mathrm{ee}}^{xy} + \widehat{\alpha}_{\mathrm{em}}^{xx} - \widehat{\alpha}_{\mathrm{me}}^{yy} - \frac{1}{\eta_0}\widehat{\alpha}_{\mathrm{mm}}^{yx}\right)\hat{\mathbf{x}}\hat{\mathbf{y}}\Bigg\}\cdot\mathbf{E}_{\mathrm{inc}}\end{aligned} \tag{51}$$

4 Synthesizing polarization transformers

In this section, the previously derived expressions for reflected and transmitted fields are used to synthesize polarization transformers. The first example is a reciprocal CPSS and the second is a twist polarizer. The equations can also be used to study inverse problems: as an example, it is shown that a sheet of zero thickness cannot act as a CPSS.

4.1 Polarizabilities for a RHCPSS

By using equations (49) and (51) and imposing wanted requirements for reflected and transmitted fields, we can derive conditions that must be fulfilled by the effective polarizabilities in order to obtain a specific operation. In this section, we will study a right-hand circular polarization selective surface (RHCPSS), i.e., a device that reflects the RH circular polarization and allows the LH component to pass as circular. The handednesses of the reflected or transmitted waves are not fixed at this point. The operation of RHCPSS can be described by the following conditions: When the incident field is RHCP, the transmission must be zero and the reflected wave must be circular ($-$ in $\mp$ corresponds to RHCP, $+$ to LHCP):

$$\mathbf{E}_{\mathrm{inc}} = E_0(\hat{\mathbf{x}} + j\hat{\mathbf{y}}) \Rightarrow \begin{cases} \mathbf{E}_{\mathrm{t}} = 0 \\ \mathbf{E}_{\mathrm{r}} = AE_0(\hat{\mathbf{x}} \mp j\hat{\mathbf{y}}) \end{cases} \tag{52}$$

Similarly, for incident an LHCP wave the reflected field must be zero and the transmitted field must be circular ($-$ in $\mp$ corresponds to LHCP, $+$ to RHCP).

$$\mathbf{E}_{\mathrm{inc}} = E_0(\hat{\mathbf{x}} - j\hat{\mathbf{y}}) \Rightarrow \begin{cases} \mathbf{E}_{\mathrm{t}} = AE_0(\hat{\mathbf{x}} \mp j\hat{\mathbf{y}}) \\ \mathbf{E}_{\mathrm{r}} = 0 \end{cases} \tag{53}$$

Here A is any complex coefficient that allows any phase for reflected and transmitted waves. We also assume that the structure is lossless by setting $|A| = 1$. These conditions must be studied one at a time. At first, the RHCP incident wave and the condition of zero transmission from (52) will be substituted into the expression for the transmitted field (51):

$$\begin{aligned} \mathbf{E}_{\mathrm{t}} = &\left\{ 1 - \frac{j\omega}{2S}\left(\eta_0 \widehat{\alpha}_{\mathrm{ee}}^{xx} - \widehat{\alpha}_{\mathrm{em}}^{xy} - \widehat{\alpha}_{\mathrm{me}}^{yx} + \frac{1}{\eta_0}\widehat{\alpha}_{\mathrm{mm}}^{yy} \right) \right. \\ &\left. + j\left(-\frac{j\omega}{2S}\left(\eta_0 \widehat{\alpha}_{\mathrm{ee}}^{xy} + \widehat{\alpha}_{\mathrm{em}}^{xx} - \widehat{\alpha}_{\mathrm{me}}^{yy} - \frac{1}{\eta_0}\widehat{\alpha}_{\mathrm{mm}}^{yx} \right) \right) \right\} E_0 \hat{\mathbf{x}} \\ &+ \left\{ -\frac{j\omega}{2S}\left(\eta_0 \widehat{\alpha}_{\mathrm{ee}}^{yx} - \widehat{\alpha}_{\mathrm{em}}^{yy} + \widehat{\alpha}_{\mathrm{me}}^{xx} - \frac{1}{\eta_0}\widehat{\alpha}_{\mathrm{mm}}^{xy} \right) \right. \\ &\left. + j\left(1 - \frac{j\omega}{2S}\left(\eta_0 \widehat{\alpha}_{\mathrm{ee}}^{yy} + \widehat{\alpha}_{\mathrm{em}}^{yx} + \widehat{\alpha}_{\mathrm{me}}^{xy} + \frac{1}{\eta_0}\widehat{\alpha}_{\mathrm{mm}}^{xx} \right) \right) \right\} E_0 \hat{\mathbf{y}} = 0 \end{aligned} \tag{54}$$

This, of course, means that both components of the transmitted field must be zero simultaneously:

$$1-\frac{j\omega}{2S}\left(\eta_0\widehat{\alpha}_{\mathrm{ee}}^{xx}-\widehat{\alpha}_{\mathrm{em}}^{xy}-\widehat{\alpha}_{\mathrm{me}}^{yx}+\frac{1}{\eta_0}\widehat{\alpha}_{\mathrm{mm}}^{yy}+j\eta_0\widehat{\alpha}_{\mathrm{ee}}^{xy}+j\widehat{\alpha}_{\mathrm{em}}^{xx}-j\widehat{\alpha}_{\mathrm{me}}^{yy}-j\frac{1}{\eta_0}\widehat{\alpha}_{\mathrm{mm}}^{yx}\right)=0 \tag{55}$$

$$1-\frac{j\omega}{2S}\left(-j\eta_0\widehat{\alpha}_{\mathrm{ee}}^{yx}+j\widehat{\alpha}_{\mathrm{em}}^{yy}-j\widehat{\alpha}_{\mathrm{me}}^{xx}+j\frac{1}{\eta_0}\widehat{\alpha}_{\mathrm{mm}}^{xy}+\eta_0\widehat{\alpha}_{\mathrm{ee}}^{yy}+\widehat{\alpha}_{\mathrm{em}}^{yx}+\widehat{\alpha}_{\mathrm{me}}^{xy}+\frac{1}{\eta_0}\widehat{\alpha}_{\mathrm{mm}}^{xx}\right)=0 \tag{56}$$

The next condition in (52) is that for RHCP incidence the reflected field must be circularly polarized. Now we use the previously derived equation for the reflected field (49):

$$\begin{aligned}\mathbf{E}_{\mathrm{r}}=&-\frac{j\omega}{2S}\left[\eta_0\widehat{\alpha}_{\mathrm{ee}}^{xx}-\widehat{\alpha}_{\mathrm{em}}^{xy}+\widehat{\alpha}_{\mathrm{me}}^{xy}-\frac{1}{\eta_0}\widehat{\alpha}_{\mathrm{mm}}^{yy}+j\left(\eta_0\widehat{\alpha}_{\mathrm{ee}}^{xy}+\widehat{\alpha}_{\mathrm{em}}^{xx}+\widehat{\alpha}_{\mathrm{me}}^{yy}+\frac{1}{\eta_0}\widehat{\alpha}_{\mathrm{mm}}^{yx}\right)\right]E_0\hat{\mathbf{x}}\\&-\frac{j\omega}{2S}\left[\eta_0\widehat{\alpha}_{\mathrm{ee}}^{yx}-\widehat{\alpha}_{\mathrm{em}}^{yy}-\widehat{\alpha}_{\mathrm{me}}^{xx}+\frac{1}{\eta_0}\widehat{\alpha}_{\mathrm{mm}}^{xy}+j\left(\eta_0\widehat{\alpha}_{\mathrm{ee}}^{yy}+\widehat{\alpha}_{\mathrm{em}}^{yx}-\widehat{\alpha}_{\mathrm{me}}^{xy}-\frac{1}{\eta_0}\widehat{\alpha}_{\mathrm{mm}}^{xx}\right)\right]E_0\hat{\mathbf{y}}\end{aligned} \tag{57}$$

$$\begin{aligned}=&-\frac{j\omega}{2S}\left[\left(\eta_0\widehat{\alpha}_{\mathrm{ee}}^{xx}-\widehat{\alpha}_{\mathrm{em}}^{xy}+\widehat{\alpha}_{\mathrm{me}}^{xy}-\frac{1}{\eta_0}\widehat{\alpha}_{\mathrm{mm}}^{yy}+j\eta_0\widehat{\alpha}_{\mathrm{ee}}^{xy}+j\widehat{\alpha}_{\mathrm{em}}^{xx}+j\widehat{\alpha}_{\mathrm{me}}^{yy}+j\frac{1}{\eta_0}\widehat{\alpha}_{\mathrm{mm}}^{yx}\right)\hat{\mathbf{x}}\right.\\&\left.-j\left(j\eta_0\widehat{\alpha}_{\mathrm{ee}}^{yx}-j\widehat{\alpha}_{\mathrm{em}}^{yy}-j\widehat{\alpha}_{\mathrm{me}}^{xx}+j\frac{1}{\eta_0}\widehat{\alpha}_{\mathrm{mm}}^{xy}-\eta_0\widehat{\alpha}_{\mathrm{ee}}^{yy}-\widehat{\alpha}_{\mathrm{em}}^{yx}+\widehat{\alpha}_{\mathrm{me}}^{xy}+\frac{1}{\eta_0}\widehat{\alpha}_{\mathrm{mm}}^{xx}\right)\hat{\mathbf{y}}\right]E_0\end{aligned} \tag{58}$$

The reflected wave in (58) is circular, if the x-component times $(\mp j)$ is equal to the y-component:

$$\begin{aligned}&\eta_0\widehat{\alpha}_{\mathrm{ee}}^{xx}-\widehat{\alpha}_{\mathrm{em}}^{xy}+\widehat{\alpha}_{\mathrm{me}}^{xy}-\frac{1}{\eta_0}\widehat{\alpha}_{\mathrm{mm}}^{yy}+j\eta_0\widehat{\alpha}_{\mathrm{ee}}^{xy}+j\widehat{\alpha}_{\mathrm{em}}^{xx}+j\widehat{\alpha}_{\mathrm{me}}^{yy}+j\frac{1}{\eta_0}\widehat{\alpha}_{\mathrm{mm}}^{yx}\\=&\mp\left(j\eta_0\widehat{\alpha}_{\mathrm{ee}}^{yx}-j\widehat{\alpha}_{\mathrm{em}}^{yy}-j\widehat{\alpha}_{\mathrm{me}}^{xx}+j\frac{1}{\eta_0}\widehat{\alpha}_{\mathrm{mm}}^{xy}-\eta_0\widehat{\alpha}_{\mathrm{ee}}^{yy}-\widehat{\alpha}_{\mathrm{em}}^{yx}+\widehat{\alpha}_{\mathrm{me}}^{xy}+\frac{1}{\eta_0}\widehat{\alpha}_{\mathrm{mm}}^{xx}\right)\end{aligned} \tag{59}$$

Equation (53), i.e. the case of incident LHCP wave, can be treated similarly to obtain another set of relations. First the transmitted field from (51):

$$\begin{aligned}\mathbf{E}_{\mathrm{t}}=&\left\{1-\frac{j\omega}{2S}\left(\eta_0\widehat{\alpha}_{\mathrm{ee}}^{xx}-\widehat{\alpha}_{\mathrm{em}}^{xy}-\widehat{\alpha}_{\mathrm{me}}^{yx}+\frac{1}{\eta_0}\widehat{\alpha}_{\mathrm{mm}}^{yy}\right)\right.\\&\left.-j\left(-\frac{j\omega}{2S}\left(\eta_0\widehat{\alpha}_{\mathrm{ee}}^{xy}+\widehat{\alpha}_{\mathrm{em}}^{xx}-\widehat{\alpha}_{\mathrm{me}}^{yy}-\frac{1}{\eta_0}\widehat{\alpha}_{\mathrm{mm}}^{yx}\right)\right)\right\}E_0\hat{\mathbf{x}}\\&+\left\{-\frac{j\omega}{2S}\left(\eta_0\widehat{\alpha}_{\mathrm{ee}}^{yx}-\widehat{\alpha}_{\mathrm{em}}^{yy}+\widehat{\alpha}_{\mathrm{me}}^{xx}-\frac{1}{\eta_0}\widehat{\alpha}_{\mathrm{mm}}^{xy}\right)\right.\\&\left.-j\left(1-\frac{j\omega}{2S}\left(\eta_0\widehat{\alpha}_{\mathrm{ee}}^{yy}+\widehat{\alpha}_{\mathrm{em}}^{yx}+\widehat{\alpha}_{\mathrm{me}}^{xy}+\frac{1}{\eta_0}\widehat{\alpha}_{\mathrm{mm}}^{xx}\right)\right)\right\}E_0\hat{\mathbf{y}}\end{aligned} \tag{60}$$

$$\mathbf{E}_{\mathrm{t}} = \left\{1 - \frac{j\omega}{2S}\left(\eta_0\widehat{\alpha}_{\mathrm{ee}}^{xx} - \widehat{\alpha}_{\mathrm{em}}^{xy} - \widehat{\alpha}_{\mathrm{me}}^{yx} + \frac{1}{\eta_0}\widehat{\alpha}_{\mathrm{mm}}^{yy} - j\eta_0\widehat{\alpha}_{\mathrm{ee}}^{xy} - j\widehat{\alpha}_{\mathrm{em}}^{xx} + j\widehat{\alpha}_{\mathrm{me}}^{yy} + j\frac{1}{\eta_0}\widehat{\alpha}_{\mathrm{mm}}^{yx}\right)\right\} E_0\hat{\mathbf{x}}$$
$$- j\left\{1 - \frac{j\omega}{2S}\left(j\eta_0\widehat{\alpha}_{\mathrm{ee}}^{yx} - j\widehat{\alpha}_{\mathrm{em}}^{yy} + j\widehat{\alpha}_{\mathrm{me}}^{xx} - j\frac{1}{\eta_0}\widehat{\alpha}_{\mathrm{mm}}^{xy} + \eta_0\widehat{\alpha}_{\mathrm{ee}}^{yy} + \widehat{\alpha}_{\mathrm{em}}^{yx} + \widehat{\alpha}_{\mathrm{me}}^{xy} + \frac{1}{\eta_0}\widehat{\alpha}_{\mathrm{mm}}^{xx}\right)\right\} E_0\hat{\mathbf{y}} \tag{61}$$

With LHCP incidence the transmitted wave (61) should be circular (+ in ± corresponds to the LHCP wave):

$$1 - \frac{j\omega}{2S}\left(\eta_0\widehat{\alpha}_{\mathrm{ee}}^{xx} - \widehat{\alpha}_{\mathrm{em}}^{xy} - \widehat{\alpha}_{\mathrm{me}}^{yx} + \frac{1}{\eta_0}\widehat{\alpha}_{\mathrm{mm}}^{yy} - j\eta_0\widehat{\alpha}_{\mathrm{ee}}^{xy} - j\widehat{\alpha}_{\mathrm{em}}^{xx} + j\widehat{\alpha}_{\mathrm{me}}^{yy} + j\frac{1}{\eta_0}\widehat{\alpha}_{\mathrm{mm}}^{yx}\right)$$
$$= \pm\left(1 - \frac{j\omega}{2S}\left(j\eta_0\widehat{\alpha}_{\mathrm{ee}}^{yx} - j\widehat{\alpha}_{\mathrm{em}}^{yy} + j\widehat{\alpha}_{\mathrm{me}}^{xx} - j\frac{1}{\eta_0}\widehat{\alpha}_{\mathrm{mm}}^{xy} + \eta_0\widehat{\alpha}_{\mathrm{ee}}^{yy} + \widehat{\alpha}_{\mathrm{em}}^{yx} + \widehat{\alpha}_{\mathrm{me}}^{xy} + \frac{1}{\eta_0}\widehat{\alpha}_{\mathrm{mm}}^{xx}\right)\right) \tag{62}$$

The last condition for RHCPSS (53) states that with LHCP incidence there should be no reflection :

$$\mathbf{E}_{\mathrm{r}} = -\frac{j\omega}{2S}\left[\left(\eta_0\widehat{\alpha}_{\mathrm{ee}}^{xx} - \widehat{\alpha}_{\mathrm{em}}^{xy} + \widehat{\alpha}_{\mathrm{me}}^{xy} - \frac{1}{\eta_0}\widehat{\alpha}_{\mathrm{mm}}^{yy} - j\left(\eta_0\widehat{\alpha}_{\mathrm{ee}}^{xy} + \widehat{\alpha}_{\mathrm{em}}^{xx} + \widehat{\alpha}_{\mathrm{me}}^{yy} + \frac{1}{\eta_0}\widehat{\alpha}_{\mathrm{mm}}^{yx}\right)\right)\hat{\mathbf{x}}\right.$$
$$\left. + \left(\eta_0\widehat{\alpha}_{\mathrm{ee}}^{yx} - \widehat{\alpha}_{\mathrm{em}}^{yy} - \widehat{\alpha}_{\mathrm{me}}^{xx} + \frac{1}{\eta_0}\widehat{\alpha}_{\mathrm{mm}}^{xy} - j\left(\eta_0\widehat{\alpha}_{\mathrm{ee}}^{yy} + \widehat{\alpha}_{\mathrm{em}}^{yx} - \widehat{\alpha}_{\mathrm{me}}^{xy} - \frac{1}{\eta_0}\widehat{\alpha}_{\mathrm{mm}}^{xx}\right)\right)\hat{\mathbf{y}}\right] = 0 \tag{63}$$

Thus, both components of (63) must be zero:

$$\eta_0\widehat{\alpha}_{\mathrm{ee}}^{xx} - j\eta_0\widehat{\alpha}_{\mathrm{ee}}^{xy} - \frac{1}{\eta_0}\widehat{\alpha}_{\mathrm{mm}}^{yy} - j\frac{1}{\eta_0}\widehat{\alpha}_{\mathrm{mm}}^{yx} - j\widehat{\alpha}_{\mathrm{em}}^{xx} - j\widehat{\alpha}_{\mathrm{me}}^{yy} - \widehat{\alpha}_{\mathrm{em}}^{xy} + \widehat{\alpha}_{\mathrm{me}}^{xy} = 0 \tag{64}$$

$$-j\eta_0\widehat{\alpha}_{\mathrm{ee}}^{yy} + \eta_0\widehat{\alpha}_{\mathrm{ee}}^{yx} + j\frac{1}{\eta_0}\widehat{\alpha}_{\mathrm{mm}}^{xx} + \frac{1}{\eta_0}\widehat{\alpha}_{\mathrm{mm}}^{xy} - \widehat{\alpha}_{\mathrm{em}}^{yy} - \widehat{\alpha}_{\mathrm{me}}^{xx} - j\widehat{\alpha}_{\mathrm{em}}^{yx} + j\widehat{\alpha}_{\mathrm{me}}^{xy} = 0 \tag{65}$$

4.1.1 CPSS without magnetic polarizabilities

By using the previously discussed conditions for a CPSS, it is possible to synthesize such surfaces. This section studies a possibility of creating a CPSS with the thickness of the particle being 0. This means that there are no current loops, i.e., no transversal magnetic dipoles can be induced. In the equations this means that $\overline{\overline{\widehat{\alpha}}}_{\mathrm{em}} = \overline{\overline{\widehat{\alpha}}}_{\mathrm{me}} = \overline{\overline{\widehat{\alpha}}}_{\mathrm{mm}} = 0$ and we have only electric polarizabilities $\overline{\overline{\widehat{\alpha}}}_{\mathrm{ee}}$.

The six conditions of a RHCPSS ((55), (56), (59), (62), (64), (65)) can be sim-

plified clearly just by removing the magnetic polarizabilities:

$$1 - \frac{j\omega}{2S}(\eta_0 \widehat{\alpha}_{\mathrm{ee}}^{xx} + j\eta_0 \widehat{\alpha}_{\mathrm{ee}}^{xy}) = 0 \tag{66}$$

$$1 - \frac{j\omega}{2S}(\eta_0 \widehat{\alpha}_{\mathrm{ee}}^{yy} + j\eta_0 \widehat{\alpha}_{\mathrm{ee}}^{yx}) = 0 \tag{67}$$

$$\eta_0 \widehat{\alpha}_{\mathrm{ee}}^{xx} + j\eta_0 \widehat{\alpha}_{\mathrm{ee}}^{xy} = \pm(j\eta_0 \widehat{\alpha}_{\mathrm{ee}}^{yx} - \eta_0 \widehat{\alpha}_{\mathrm{ee}}^{yy}) \tag{68}$$

$$1 - \frac{j\omega}{2S}(\eta_0 \widehat{\alpha}_{\mathrm{ee}}^{xx} - j\eta_0 \widehat{\alpha}_{\mathrm{ee}}^{xy}) = \pm\left(1 - \frac{j\omega}{2S}(j\eta_0 \widehat{\alpha}_{\mathrm{ee}}^{yx} + \eta_0 \widehat{\alpha}_{\mathrm{ee}}^{yy})\right) \tag{69}$$

$$\widehat{\alpha}_{\mathrm{ee}}^{xx} - j\widehat{\alpha}_{\mathrm{ee}}^{xy} = 0 \tag{70}$$

$$\widehat{\alpha}_{\mathrm{ee}}^{yx} - j\widehat{\alpha}_{\mathrm{ee}}^{yy} = 0 \tag{71}$$

By substituting (70) and (71) in (68) we get $\widehat{\alpha}_{\mathrm{ee}}^{xx} = \widehat{\alpha}_{\mathrm{ee}}^{xy} = 0$. If we again substitute this result to (66) we get $1 - \frac{j\omega}{2S}(\eta_0 \cdot 0 + j\eta_0 \cdot 0) = 0$. This equation is, of course, impossible. Note that no assumptions were made of, e.g., the reciprocity of the particles. Therefore the needed conditions for a CPSS at normal incidence cannot be obtained with a sheet of zero thickness. However, this is possible for oblique incidence, as even the created magnetic dipole, that is normal to the surface, has a component that is transversal to the direction of the propagation $\mathbf{k}_0$.

4.1.2 A reciprocal canonical helix as a RHCPSS

Since the CPSS with zero thickness is impossible, also the magnetic polarizability terms must be allowed. For practical reasons, the scatterers are assumed to be reciprocal, i.e., $\overline{\overline{\alpha}}_{\mathrm{ee}} = \overline{\overline{\alpha}}_{\mathrm{ee}}^T$, $\overline{\overline{\alpha}}_{\mathrm{em}} = -\overline{\overline{\alpha}}_{\mathrm{me}}^T$, and $\overline{\overline{\alpha}}_{\mathrm{mm}} = \overline{\overline{\alpha}}_{\mathrm{mm}}^T$ [36]. Due to the symmetry of reciprocal polarizability dyadics, we can use the same symbol to represent various components of the polarizabilities (14) – (17): $\alpha_{\mathrm{ee}}^{xy} = \alpha_{\mathrm{ee}}^{yx}$, $\alpha_{\mathrm{mm}}^{xy} = \alpha_{\mathrm{mm}}^{yx}$, $\alpha_{\mathrm{em}}^{xx} = -\alpha_{\mathrm{me}}^{xx}$, $\alpha_{\mathrm{em}}^{yy} = -\alpha_{\mathrm{me}}^{yy}$, $\alpha_{\mathrm{em}}^{xy} = -\alpha_{\mathrm{me}}^{yx}$, $\alpha_{\mathrm{em}}^{yx} = -\alpha_{\mathrm{me}}^{xy}$. Reciprocity also affects the handednesses of the reflected and transmitted wave: the handedness must not change either in the reflection nor in the transmission [7, 19].

Now equations (55) and (56), i.e., the conditions that the RHCP incidence is not transmitted, simplify as following:

$$1 - \frac{j\omega}{2S}\left(\eta_0 \widehat{\alpha}_{\mathrm{ee}}^{xx} + \frac{1}{\eta_0}\widehat{\alpha}_{\mathrm{mm}}^{yy} + j\eta_0 \widehat{\alpha}_{\mathrm{ee}}^{yx} + j\widehat{\alpha}_{\mathrm{em}}^{xx} - j\widehat{\alpha}_{\mathrm{me}}^{yy} - j\frac{1}{\eta_0}\widehat{\alpha}_{\mathrm{mm}}^{yx}\right) = 0 \tag{72}$$

$$1 - \frac{j\omega}{2S}\left(\eta_0 \widehat{\alpha}_{\mathrm{ee}}^{yy} + \frac{1}{\eta_0}\widehat{\alpha}_{\mathrm{mm}}^{xx} - j\eta_0 \widehat{\alpha}_{\mathrm{ee}}^{yx} + j\widehat{\alpha}_{\mathrm{em}}^{yy} - j\widehat{\alpha}_{\mathrm{me}}^{xx} + j\frac{1}{\eta_0}\widehat{\alpha}_{\mathrm{mm}}^{xy}\right) = 0 \tag{73}$$

Similarly, the reciprocity assumption reduces equation (59) to a simpler form:

$$\eta_0^2(\widehat{\alpha}_{\mathrm{ee}}^{xx} + \widehat{\alpha}_{\mathrm{ee}}^{yy}) = \widehat{\alpha}_{\mathrm{mm}}^{xx} + \widehat{\alpha}_{\mathrm{mm}}^{yy} \tag{74}$$

By assuming the reciprocity and that the LHCP incidence is transmitted as LHCP, the condition for LHCP transmission (62) simplifies into:

$$\eta_0(\widehat{\alpha}_{\mathrm{ee}}^{xx} - \widehat{\alpha}_{\mathrm{ee}}^{yy}) + \frac{1}{\eta_0}(\widehat{\alpha}_{\mathrm{mm}}^{yy} - \widehat{\alpha}_{\mathrm{mm}}^{xx}) = j2\eta_0 \widehat{\alpha}_{\mathrm{ee}}^{yx} - j2\frac{1}{\eta_0}\widehat{\alpha}_{\mathrm{mm}}^{xy} \tag{75}$$

Also the zero-reflection conditions (64) and (65) for LHCP incidence simplify by assuming reciprocity:

$$\eta_0\widehat{\alpha}_{\mathrm{ee}}^{xx} - j\eta_0\widehat{\alpha}_{\mathrm{ee}}^{xy} - \frac{1}{\eta_0}\widehat{\alpha}_{\mathrm{mm}}^{yy} - j\frac{1}{\eta_0}\widehat{\alpha}_{\mathrm{mm}}^{yx} - j\widehat{\alpha}_{\mathrm{em}}^{xx} - j\widehat{\alpha}_{\mathrm{me}}^{yy} - 2\widehat{\alpha}_{\mathrm{em}}^{xy} = 0 \tag{76}$$

$$-j\eta_0\widehat{\alpha}_{\mathrm{ee}}^{yy} + \eta_0\widehat{\alpha}_{\mathrm{ee}}^{yx} + j\frac{1}{\eta_0}\widehat{\alpha}_{\mathrm{mm}}^{xx} + \frac{1}{\eta_0}\widehat{\alpha}_{\mathrm{mm}}^{xy} - \widehat{\alpha}_{\mathrm{em}}^{yy} - \widehat{\alpha}_{\mathrm{me}}^{xx} - j2\widehat{\alpha}_{\mathrm{em}}^{yx} = 0 \tag{77}$$

Now we have six equations ((72) – (77)) that must be fulfilled in order to obtain an ideal reciprocal RHCPSS. We also have 10 free parameters in our equations. We can use the extra freedom in design by setting all y-directed terms in polarizability dyadics to be zero and thus simplifying the equations even more. This means that y-directed fields do not induce dipole moments and no dipole moments are induced in y-direction. Now our polarizability dyadics resemble the one of a small canonical helix, geometry of which is shown in Fig. 9. Canonical helix or chiral particle comprises a loop as a magnetic dipole and a straight wire as an electric dipole. The geometry is a well-known example of a simple chiral inclusion [14, 37].

Simple expressions for the individual polarizabilities of a (right handed) canonical helix can be obtained, if we assume constant current in the loop and linear current distribution in the electric dipole [36]:

$$\alpha_{\mathrm{ee}}^{xx} = \frac{l^2}{j\omega(Z_{\mathrm{l}} + Z_{\mathrm{w}})} \tag{78}$$

$$\alpha_{\mathrm{em}}^{xx} = -\mu_0\frac{\pi r_{\mathrm{l}}^2 l}{Z_{\mathrm{l}} + Z_{\mathrm{w}}} \tag{79}$$

$$\alpha_{\mathrm{me}}^{xx} = +\mu_0\frac{\pi r_{\mathrm{l}}^2 l}{Z_{\mathrm{l}} + Z_{\mathrm{w}}} \tag{80}$$

$$\alpha_{\mathrm{mm}}^{xx} = -\mu_0^2\frac{j\omega(\pi r_{\mathrm{l}}^2)^2}{Z_{\mathrm{l}} + Z_{\mathrm{w}}} \tag{81}$$

Here Z_{l} and Z_{w} are the input impedances of the loop and the wire, respectively. Due to the symmetry of the current distribution, the following relation holds [36]:

$$\alpha_{\mathrm{ee}}^{xx}\alpha_{\mathrm{mm}}^{xx} = \alpha_{\mathrm{em}}^{xx}\alpha_{\mathrm{me}}^{xx} \tag{82}$$

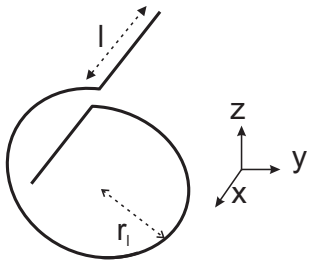

Figure 9: The geometry of a single chiral particle with the coordinate system.

The particle can be assumed to be resonant at the design frequency in order to further simplify the calculations. This means that $Z_\mathrm{l} + Z_\mathrm{w}$ is real and the total length of the wire forming the particle is $L = 2l + 2\pi r_\mathrm{l} \approx \lambda_0/2$. For small lossless electric and magnetic dipole antennas the input resistances read as follows [38]:

$$R_\mathrm{w} = \frac{\eta_0}{6\pi} k_0^2 l^2 \tag{83}$$

$$R_\mathrm{l} = \frac{\eta_0}{6\pi} k_0^4 (\pi r_\mathrm{l}^2)^2 \tag{84}$$

$$Z_\mathrm{l} + Z_\mathrm{w} = \frac{\eta_0}{6\pi} \left(k_0^2 l^2 + k_0^4 \left(\pi r_\mathrm{l}^2 \right)^2 \right) \tag{85}$$

The aforementioned six equations ((72) – (77)) get the following forms:

$$1 - \frac{j\omega}{2S} \left(\eta_0 \widehat{\alpha}_\mathrm{ee}^{xx} + j \widehat{\alpha}_\mathrm{em}^{xx} \right) = 0 \tag{86}$$

$$1 - \frac{j\omega}{2S} \left(\frac{1}{\eta_0} \widehat{\alpha}_\mathrm{mm}^{xx} - j \widehat{\alpha}_\mathrm{me}^{xx} \right) = 0 \tag{87}$$

$$\eta_0^2 \widehat{\alpha}_\mathrm{ee}^{xx} = \widehat{\alpha}_\mathrm{mm}^{xx} \tag{88}$$

$$\eta_0 \widehat{\alpha}_\mathrm{ee}^{xx} = \frac{1}{\eta_0} \widehat{\alpha}_\mathrm{mm}^{xx} \tag{89}$$

$$\eta_0 \widehat{\alpha}_\mathrm{ee}^{xx} = j \widehat{\alpha}_\mathrm{em}^{xx} \tag{90}$$

$$j \frac{1}{\eta_0} \widehat{\alpha}_\mathrm{mm}^{xx} = \widehat{\alpha}_\mathrm{me}^{xx} \tag{91}$$

From this equation group one can easily solve the required values for the effective polarizabilities: $\widehat{\alpha}_\mathrm{ee}^{xx} = S/j\omega\eta_0$ and $\widehat{\alpha}_\mathrm{em}^{xx} = -S/\omega$.

By assuming reciprocity, only $\hat{\mathbf{x}}\hat{\mathbf{x}}$-terms in polarizabilities, and equation (82), the effective polarizabilities (26) – (29) can be simplified and written with the previously obtained relations as:

$$\widehat{\alpha}_\mathrm{ee}^{xx} = \frac{\alpha_\mathrm{ee}^{xx}}{1 - \beta_e \left(\alpha_\mathrm{ee}^{xx} + \dfrac{\alpha_\mathrm{mm}^{xx}}{\eta_0^2} \right)} = \frac{S}{j\omega\eta_0} \tag{92}$$

$$\widehat{\alpha}_\mathrm{em}^{xx} = \frac{\alpha_\mathrm{em}^{xx}}{1 - \beta_e \left(\alpha_\mathrm{ee}^{xx} + \dfrac{\alpha_\mathrm{mm}^{xx}}{\eta_0^2} \right)} = -\frac{S}{\omega} \tag{93}$$

$$\widehat{\alpha}_\mathrm{mm}^{xx} = \eta_0^2 \widehat{\alpha}_\mathrm{ee}^{xx} = -j\eta_0 \widehat{\alpha}_\mathrm{me}^{xx} \tag{94}$$

The last equation (94) represents the balance of different dipole moments in the scatterer, i.e., both dipole moments radiate equally strong fields. The equation can be simplified to form:

$$l = k_0 \pi r_\mathrm{l}^2 \tag{95}$$

The same relation holds for the dimensions of an ideal Huygens source antenna [39].

By combining these three equations (92) – (93) and the polarizabilities of a canonical helix (78) – (81), we can find the optimal dimensions, i.e., values of l

and r_l. First the center frequency is fixed to $f_0 = 1.5$ GHz and the unit cell size to $S = a^2 = (40\text{ mm})^2 = (\lambda_0/5)^2$ at f_0. The optimal dimensions are found to be $l = 13.5$ mm and $r_\mathrm{l} = 11.7$ mm. Numerical results for these dimensions verify the operation of the CPSS as will be discussed in greater detail in the next section. The size of the unit cell has only a small effect on l and r_l, but affects the strength of the reflection from the array.

4.2 Polarizabilities for a twist polarizer

In addition to the circular polarization selecting devices, the equations for reflected (49) and for transmitted wave (51) can be used to synthesize various other devices. This section describes a way of synthesizing twist polarizers. An ideal twist polarizer is a device that, when illuminated with a linearly polarized plane wave, has zero reflection and the transmitted field polarization has a 90° angle to the incident field. These properties can be expressed by the following equations:

$$\mathbf{E}_\mathrm{inc} = E_0\hat{\mathbf{x}} \Rightarrow \begin{cases} \mathbf{E}_\mathrm{r} = 0 \\ \mathbf{E}_\mathrm{t} = -AE_0\hat{\mathbf{y}} \end{cases} \tag{96}$$

$$\mathbf{E}_\mathrm{inc} = E_0\hat{\mathbf{y}} \Rightarrow \begin{cases} \mathbf{E}_\mathrm{r} = 0 \\ \mathbf{E}_\mathrm{t} = AE_0\hat{\mathbf{x}} \end{cases} \tag{97}$$

where A is again any complex number ($|A| = 1$) to allow any phase for the transmitted wave.

Now conditions (96) and (97) can be substituted into equations (49) and (51) in order to obtain the values for the effective polarizabilities. In this section, both $\hat{\mathbf{x}}\hat{\mathbf{x}}$ and $\hat{\mathbf{y}}\hat{\mathbf{y}}$ directed terms are allowed in the effective polarizability dyadics. The cross-terms $\hat{\mathbf{x}}\hat{\mathbf{y}}$ and $\hat{\mathbf{y}}\hat{\mathbf{x}}$ are not used.

Again, the conditions for different incidences can be examined separately. At first, the incident field is x-polarized and the reflected field is made zero:

$$\begin{aligned} \mathbf{E}_\mathrm{r} = -\frac{j\omega}{2S}\Bigg\{ &\left(\eta_0\widehat{\alpha}_\mathrm{ee}^{xx} - \widehat{\alpha}_\mathrm{em}^{xy} + \widehat{\alpha}_\mathrm{me}^{yx} - \frac{1}{\eta_0}\widehat{\alpha}_\mathrm{mm}^{yy}\right)\hat{\mathbf{x}} \\ &+ \left(\eta_0\widehat{\alpha}_\mathrm{ee}^{yx} - \widehat{\alpha}_\mathrm{em}^{yy} - \widehat{\alpha}_\mathrm{me}^{xx} + \frac{1}{\eta_0}\widehat{\alpha}_\mathrm{mm}^{xy}\right)\hat{\mathbf{y}}\Bigg\} = 0 \end{aligned} \tag{98}$$

By assuming reciprocity and dropping the cross-polarizabilities ($\hat{\mathbf{x}}\hat{\mathbf{y}}$ and $\hat{\mathbf{y}}\hat{\mathbf{x}}$) these equations simplify:

$$\eta_0^2\widehat{\alpha}_\mathrm{ee}^{xx} = \widehat{\alpha}_\mathrm{mm}^{yy} \tag{99}$$

$$\widehat{\alpha}_\mathrm{me}^{xx} = -\widehat{\alpha}_\mathrm{em}^{yy} \tag{100}$$

The transmitted field for the x-polarized incidence is:

$$\begin{aligned} \mathbf{E}_\mathrm{t} = &\left[1 - \frac{j\omega}{2S}\left(\eta_0\widehat{\alpha}_\mathrm{ee}^{xx} - \widehat{\alpha}_\mathrm{em}^{xy} - \widehat{\alpha}_\mathrm{em}^{xy} - \widehat{\alpha}_\mathrm{me}^{yx} + \frac{1}{\eta_0}\widehat{\alpha}_\mathrm{mm}^{yy}\right)\right]\hat{\mathbf{x}} \\ &- \frac{j\omega}{2S}\left(\eta_0\widehat{\alpha}_\mathrm{ee}^{yx} - \widehat{\alpha}_\mathrm{em}^{yy} + \widehat{\alpha}_\mathrm{me}^{xx} - \frac{1}{\eta_0}\alpha_\mathrm{mm}^{xy}\right)\hat{\mathbf{y}} \end{aligned} \tag{101}$$

The x-component of the transmitted wave must be zero, wich requires:

$$\widehat{\alpha}_{\mathrm{ee}}^{xx} = \frac{S}{j\eta_0\omega} \tag{102}$$

The y-component must equal to $-A$:

$$\widehat{\alpha}_{\mathrm{me}}^{xx} - \widehat{\alpha}_{\mathrm{em}}^{yy} = 2\widehat{\alpha}_{\mathrm{me}}^{xx} = \frac{2S}{j\omega}A \tag{103}$$

The y-polarized incidence (97) can be treated similarly, which results in:

$$\widehat{\alpha}_{\mathrm{ee}}^{yy} = \frac{1}{\eta_0^2}\widehat{\alpha}_{\mathrm{mm}}^{xx} = \frac{S}{j\eta_0\omega} \tag{104}$$

$$\widehat{\alpha}_{\mathrm{em}}^{xx} = -\widehat{\alpha}_{\mathrm{me}}^{yy} \tag{105}$$

$$\widehat{\alpha}_{\mathrm{em}}^{xx} - \widehat{\alpha}_{\mathrm{me}}^{yy} = 2\widehat{\alpha}_{\mathrm{em}}^{xx} = -\frac{2S}{j\omega}A \tag{106}$$

These equations are very symmetric: $\hat{\mathbf{x}}\hat{\mathbf{x}}$ terms are similar to the $\hat{\mathbf{y}}\hat{\mathbf{y}}$ terms and can be chosen to be equal, i.e., the surface is isotropic in the transversal plane. Now the effective polarizability dyadics (18) have the forms:

$$\overline{\overline{\widehat{\alpha}}}_{\mathrm{ee}} = \widehat{\alpha}_{\mathrm{ee}}(\hat{\mathbf{x}}\hat{\mathbf{x}} + \hat{\mathbf{y}}\hat{\mathbf{y}}) = \frac{S}{j\omega\eta_0}(\hat{\mathbf{x}}\hat{\mathbf{x}} + \hat{\mathbf{y}}\hat{\mathbf{y}}) \tag{107}$$

$$\overline{\overline{\widehat{\alpha}}}_{\mathrm{em}} = \widehat{\alpha}_{\mathrm{em}}(\hat{\mathbf{x}}\hat{\mathbf{x}} + \hat{\mathbf{y}}\hat{\mathbf{y}}) = -\frac{S}{j\omega}A(\hat{\mathbf{x}}\hat{\mathbf{x}} + \hat{\mathbf{y}}\hat{\mathbf{y}}) \tag{108}$$

$$\overline{\overline{\widehat{\alpha}}}_{\mathrm{me}} = \widehat{\alpha}_{\mathrm{me}}(\hat{\mathbf{x}}\hat{\mathbf{x}} + \hat{\mathbf{y}}\hat{\mathbf{y}}) = \frac{S}{j\omega}A(\hat{\mathbf{x}}\hat{\mathbf{x}} + \hat{\mathbf{y}}\hat{\mathbf{y}}) \tag{109}$$

$$\overline{\overline{\widehat{\alpha}}}_{\mathrm{mm}} = \widehat{\alpha}_{\mathrm{mm}}(\hat{\mathbf{x}}\hat{\mathbf{x}} + \hat{\mathbf{y}}\hat{\mathbf{y}}) = \widehat{\alpha}_{\mathrm{ee}}\eta_0^2(\hat{\mathbf{x}}\hat{\mathbf{x}} + \hat{\mathbf{y}}\hat{\mathbf{y}}) \tag{110}$$

If we set $A = j$, these effective polarizabilities start again to resemble the ones in equations (92), (93), and (94). This means that a properly designed chiral element, i.e., a pair of orthogonally directed canonical helices, should work as a twist polarizer. The dimensions are the same as before: $l = 13.5$ mm and $r_1 = 11.7$ mm.

5 Synthesizing arrays of uniaxial particles

The previously discussed method is a useful tool when synthesizing polarization transformers. The equations can, however, be overly complicated in cases where uniaxial particles can be used, such as the twist polarizer. In this section, similar equations are derived for the uniaxial case, i.e., for the case where the particles are symmetric in the transverse plane. Now the polarizabilities will have the following forms:

$$\overline{\overline{\widehat{\alpha}}}_{\mathrm{ee}} = \widehat{\alpha}_{\mathrm{ee}}^{\mathrm{co}}\overline{\overline{\mathrm{I}}}_{\mathrm{t}} + \widehat{\alpha}_{\mathrm{ee}}^{\mathrm{cr}}\overline{\overline{\mathrm{J}}}_{\mathrm{t}} \tag{111}$$

$$\overline{\overline{\widehat{\alpha}}}_{\mathrm{em}} = \widehat{\alpha}_{\mathrm{em}}^{\mathrm{co}}\overline{\overline{\mathrm{I}}}_{\mathrm{t}} + \widehat{\alpha}_{\mathrm{em}}^{\mathrm{cr}}\overline{\overline{\mathrm{J}}}_{\mathrm{t}} \tag{112}$$

$$\overline{\overline{\widehat{\alpha}}}_{\mathrm{me}} = \widehat{\alpha}_{\mathrm{me}}^{\mathrm{co}}\overline{\overline{\mathrm{I}}}_{\mathrm{t}} + \widehat{\alpha}_{\mathrm{me}}^{\mathrm{cr}}\overline{\overline{\mathrm{J}}}_{\mathrm{t}} \tag{113}$$

$$\overline{\overline{\widehat{\alpha}}}_{\mathrm{mm}} = \widehat{\alpha}_{\mathrm{mm}}^{\mathrm{co}}\overline{\overline{\mathrm{I}}}_{\mathrm{t}} + \widehat{\alpha}_{\mathrm{mm}}^{\mathrm{cr}}\overline{\overline{\mathrm{J}}}_{\mathrm{t}} \tag{114}$$

Here $\overline{\overline{\mathrm{J}}}_{\mathrm{t}} = \hat{\mathbf{n}}\times\overline{\overline{\mathrm{I}}}_{\mathrm{t}}$ is the transversal rotation dyadic [34]. As the dyadics do not depend on any coordinate system, the previously discussed equations ((26) – (29)) for these effective polarizabilities can be used directly. With this notation, the induced dipole moments in (33) and (34) can be written as:

$$\mathbf{p} = \left(\overline{\overline{\widehat{\alpha}}}_{\mathrm{ee}} - \frac{1}{\eta_0}\overline{\overline{\widehat{\alpha}}}_{\mathrm{em}}\cdot\overline{\overline{\mathrm{J}}}_{\mathrm{t}}\right)\cdot\mathbf{E}_{\mathrm{inc}} \tag{115}$$

$$\mathbf{m} = \left(\overline{\overline{\widehat{\alpha}}}_{\mathrm{me}} - \frac{1}{\eta_0}\overline{\overline{\widehat{\alpha}}}_{\mathrm{mm}}\cdot\overline{\overline{\mathrm{J}}}_{\mathrm{t}}\right)\cdot\mathbf{E}_{\mathrm{inc}} \tag{116}$$

Again, the induced dipole moments correspond to a certain averaged current sheet that radiates into the surrounding free space. With the help of (47) and (50), the reflected and transmitted fields can be solved as was done previously in (49) and (51):

$$\begin{aligned}\mathbf{E}_{\mathrm{r}} = -\frac{j\omega}{2S}\Bigg[&\left(\eta_0\widehat{\alpha}_{\mathrm{ee}}^{\mathrm{co}} + \widehat{\alpha}_{\mathrm{em}}^{\mathrm{cr}} + \widehat{\alpha}_{\mathrm{me}}^{\mathrm{cr}} - \frac{1}{\eta_0}\widehat{\alpha}_{\mathrm{mm}}^{\mathrm{co}}\right)\overline{\overline{\mathrm{I}}}_{\mathrm{t}}\\ &+\left(\eta_0\widehat{\alpha}_{\mathrm{ee}}^{\mathrm{cr}} - \widehat{\alpha}_{\mathrm{em}}^{\mathrm{co}} - \widehat{\alpha}_{\mathrm{me}}^{\mathrm{co}} - \frac{1}{\eta_0}\widehat{\alpha}_{\mathrm{mm}}^{\mathrm{cr}}\right)\overline{\overline{\mathrm{J}}}_{\mathrm{t}}\Bigg]\cdot\mathbf{E}_{\mathrm{inc}}\end{aligned} \tag{117}$$

$$\begin{aligned}\mathbf{E}_{\mathrm{t}} = \Bigg\{&\left[1 - \frac{j\omega}{2S}\left(\eta_0\widehat{\alpha}_{\mathrm{ee}}^{\mathrm{co}} + \widehat{\alpha}_{\mathrm{em}}^{\mathrm{cr}} - \widehat{\alpha}_{\mathrm{me}}^{\mathrm{cr}} + \frac{1}{\eta_0}\widehat{\alpha}_{\mathrm{mm}}^{\mathrm{co}}\right)\right]\overline{\overline{\mathrm{I}}}_{\mathrm{t}}\\ &-\frac{j\omega}{2S}\left(\eta_0\widehat{\alpha}_{\mathrm{ee}}^{\mathrm{cr}} - \widehat{\alpha}_{\mathrm{em}}^{\mathrm{co}} + \widehat{\alpha}_{\mathrm{me}}^{\mathrm{co}} + \frac{1}{\eta_0}\widehat{\alpha}_{\mathrm{mm}}^{\mathrm{cr}}\right)\overline{\overline{\mathrm{J}}}_{\mathrm{t}}\Bigg\}\cdot\mathbf{E}_{\mathrm{inc}}\end{aligned} \tag{118}$$

5.1 Uniaxial twist polarizer

In order to verify these uniaxial equations, the operation of the previously presented twist polarizer is re-synthesized. In the new notation, the operation of the twist polarizer reads:

$$\mathbf{E}_{\mathrm{r}} = 0 \tag{119}$$

$$\mathbf{E}_{\mathrm{t}} = -\overline{\overline{\mathrm{J}}}_{\mathrm{t}}\cdot\mathbf{E}_{\mathrm{inc}} \tag{120}$$

The minus sign in the transmission equation is only for convenience and to produce the same handedness of particles as previously. Just as before, we set all cross-polarizabilities ($\widehat{\alpha}^{\rm cr}_{\rm ee}$, $\widehat{\alpha}^{\rm cr}_{\rm em}$, $\widehat{\alpha}^{\rm cr}_{\rm me}$, $\widehat{\alpha}^{\rm cr}_{\rm mm}$) to be zero. The zero reflection condition simplifies to:

$$\eta\widehat{\alpha}^{\rm co}_{\rm ee} + \widehat{\alpha}^{\rm cr}_{\rm em} + \widehat{\alpha}^{\rm cr}_{\rm me} - \frac{1}{\eta_0}\widehat{\alpha}^{\rm co}_{\rm mm} = 0 \tag{121}$$

$$\widehat{\alpha}^{\rm co}_{\rm ee} = \frac{1}{\eta_0^2}\widehat{\alpha}^{\rm co}_{\rm mm} \tag{122}$$

The co-polarized transmitted field must be zero:

$$1 - \frac{j\omega}{2S}\left(\eta_0\widehat{\alpha}^{\rm co}_{\rm ee} + \widehat{\alpha}^{\rm cr}_{\rm em} - \widehat{\alpha}^{\rm cr}_{\rm me} + \frac{1}{\eta_0}\widehat{\alpha}^{\rm co}_{\rm mm}\right) = 0 \tag{123}$$

$$\widehat{\alpha}^{\rm co}_{\rm mm} = \frac{\eta_0 S}{j\omega} \tag{124}$$

$$\widehat{\alpha}^{\rm co}_{\rm ee} = \frac{S}{j\omega\eta_0} \tag{125}$$

All of the power is transmitted as cross-polarized:

$$-\frac{j\omega}{2S}\left(\eta_0\widehat{\alpha}^{\rm cr}_{\rm ee} - \widehat{\alpha}^{\rm co}_{\rm em} + \widehat{\alpha}^{\rm co}_{\rm me} + \frac{1}{\eta_0}\widehat{\alpha}^{\rm cr}_{\rm mm}\right)\overline{\overline{\mathrm{J}}}_{\rm t}\cdot\mathbf{E}_{\rm inc} = -\overline{\overline{\mathrm{J}}}_{\rm t}\cdot\mathbf{E}_{\rm inc} \tag{126}$$

$$\frac{j\omega}{2S}\left(2\widehat{\alpha}^{\rm co}_{\rm me}\right) = 1 \tag{127}$$

$$\widehat{\alpha}^{\rm co}_{\rm me} = \frac{S}{j\omega} \tag{128}$$

These results are exactly the same as obtained from general bi-anisotropic equations.

6 A CPSS using an array of chiral particles

As was previously noticed in Subsection 4.1.2, an array of canonical helices, also known as chiral particles, can work as a CPSS. The previously used analytical model for such an array was greatly simplified in order to better understand the physics behind the phenomenon. Also, the model was not verified in any way. In this section, the structure will be analyzed both analytically and numerically. The geometry of a single chiral particle was shown in Fig. 9 where the electric dipole is parallel to the x-axis and the loop is in the yz-plane. The radius of the loop is denoted by r_l and the total length of the electric dipole is $2l$. The wire radius r_0 is kept constant at 0.1 mm. The square array, with the lattice constant a, is located in the xy-plane. The incident plane wave comes straight from above, i.e., $\mathbf{k}_\mathrm{inc} \uparrow\uparrow -\hat{\mathbf{z}}$.

6.1 Analytical model for chiral particles

The illuminating plane wave is propagating towards the plane, i.e., the wave vector $\mathbf{k}$ and the surface normal $\hat{\mathbf{n}}$ are antiparallel. Similarly to the approach in Section 3, the induced dipole moments can be calculated from the polarizabilities and local fields [1, 35]:

$$\begin{bmatrix} \mathbf{p} \\ \mathbf{m} \end{bmatrix} = \begin{bmatrix} \overline{\overline{\alpha}}_\mathrm{ee} & \overline{\overline{\alpha}}_\mathrm{em} \\ \overline{\overline{\alpha}}_\mathrm{me} & \overline{\overline{\alpha}}_\mathrm{mm} \end{bmatrix} \cdot \begin{bmatrix} \mathbf{E}_\mathrm{loc} \\ \mathbf{H}_\mathrm{loc} \end{bmatrix} = \begin{bmatrix} \overline{\overline{\alpha}}_\mathrm{ee} & \overline{\overline{\alpha}}_\mathrm{em} \\ \overline{\overline{\alpha}}_\mathrm{me} & \overline{\overline{\alpha}}_\mathrm{mm} \end{bmatrix} \cdot \begin{bmatrix} \mathbf{E}_\mathrm{inc} + \overline{\overline{\beta}}_\mathrm{e} \cdot \mathbf{p} \\ \mathbf{H}_\mathrm{inc} + \overline{\overline{\beta}}_\mathrm{m} \cdot \mathbf{m} \end{bmatrix} \tag{129}$$

Again, equations (42), (43), (45), and (46) can be used to calculate reflected and transmitted fields from arrays of these dipole moments. Because of the more complicated form of the polarizability dyadics, it is not easy to solve these fields directly. To overcome this difficulty, the dipole moments are divided into components and the equation group is solved analytically with the help of Wolfram Mathematica [40]:

$$p_x = \alpha_\mathrm{ee}^{xx} E_\mathrm{loc}^x + \alpha_\mathrm{ee}^{xy} E_\mathrm{loc}^y + \alpha_\mathrm{em}^{xx} H_\mathrm{loc}^x \tag{130}$$

$$p_y = \alpha_\mathrm{ee}^{yx} E_\mathrm{loc}^x + \alpha_\mathrm{ee}^{yy} E_\mathrm{loc}^y + \alpha_\mathrm{em}^{yx} H_\mathrm{loc}^x \tag{131}$$

$$m_x = \alpha_\mathrm{me}^{xx} E_\mathrm{loc}^x + \alpha_\mathrm{me}^{xy} E_\mathrm{loc}^y + \alpha_\mathrm{mm}^{xx} H_\mathrm{loc}^x \tag{132}$$

$$m_y = 0 \tag{133}$$

These individual polarizabilities can be obtained from the more detailed antenna model [36].

Since we want the reflected and transmitted wave to maintain its circular polarization, we must also study the axial ratio (AR) of these fields. AR is defined as the ratio of the minor to the major axes of the polarization ellipse. This means that $AR = 0$ corresponds to perfectly linear polarization and $AR = 1$ to perfectly circular. This is inverse of the standard IEEE definition [41]. With the standard definition, one cannot plot purely circular and purely linear polarizations on the same figure very easily. The axial ratio can be calculated with the help of the polarization vector $\mathbf{p}_\mathrm{pol}$ [34]:

$$\mathbf{p}_\mathrm{pol} = \frac{\mathbf{E} \times \mathbf{E}^*}{j\mathbf{E} \cdot \mathbf{E}^*} = \frac{E_x E_y^* - E_y E_x^*}{j(E_x E_x^* + E_y E_y^*)} \hat{\mathbf{z}} \tag{134}$$

where E_x and E_y are the corresponding components of the reflected or transmitted wave and * is the complex conjugate. The axial ratio is then obtained as

$$AR = \frac{1 - \sqrt{1 - |\mathbf{p}_{\text{pol}}|^2}}{|\mathbf{p}_{\text{pol}}|} \tag{135}$$

The direction of $\mathbf{p}_{\text{pol}}$ can be used to determine the handedness of the wave: if $\mathbf{p}_{\text{pol}} \uparrow\uparrow \mathbf{k}$ then the wave is RHCP. In our case, since $\mathbf{k}_{\text{inc}} \uparrow\uparrow -\hat{\mathbf{z}}$, the transmitted wave is RHCP if (134) is directed along the negative z-axis. Similarly the reflected wave is RHCP if the multiplier is positive [34].

6.2 Numerical simulations for canonical helices

To verify the analytical model, the same structure is studied numerically. The frequency response of the array is modeled with ANSYS HFSS [42] – a commercial finite element method (FEM) simulator. The simulation model includes a single chiral particle, made of perfect electric conductor (PEC), in free space, forming a square unit cell. The periodicity is then introduced with master and slave boundaries as suggested in [43]. As the excitation of the structure, two Floquet ports are used at both ends of the simulation space. In this case, only the first two Floquet modes are propagating (attenuation is 0 dB/mm) [43]. The simulation model can be seen in Fig. 10. After the structure is simulated, we extract the S-parameters describing the coupling between different modes on different ports. This data is then imported to MATLAB [44] and used to calculate the reflected and transmitted fields with an arbitrary excitation.

The full-wave simulated results with the analytically obtained dimensions ($S = a^2 = (40\text{ mm})^2$, $l = 13.5$ mm, $r_1 = 11.7$ mm, and wire radius $r_0 = 0.1$ mm) confirm that an array of such particles indeed acts as a CPSS. However, as the model used in Section 4.1.2 was much simplified, the polarization selectivity is not very strong and the polarization purity is poor. The aforementioned dimensions, however, are a very good starting point for optimization. As the simulations are quite lengthy

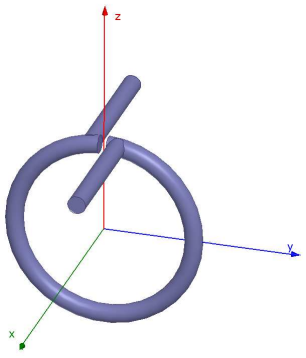

Figure 10: The simulation model of a single chiral particle. The wire radius is exaggerated for clarity.

and the results need post-processing, no automated optimization method is used but the dimensions are tuned manually. The goal of the optimization is to produce as pure CP as possible for both transmitted LHCP wave and reflected RHCP wave. According to [45] and the previously discussed analytical model, a smaller unit cell size increases the bandwidth. Therefore, also a is minimized to fit the particle in the unit cell just barely. After the optimization the final dimensions are: the length of the one arm of the electric dipole is $l = 15$ mm, the loop radius $r_\mathrm{l} = 9$ mm, the wire radius $r_0 = 0.1$ mm, and the unit cell size is $a = 34$ mm.

6.3 Comparison of the results for arrays of canonical helices

The results for previously discussed analytical and numerical methods are presented in this section. The dimensions for a chiral particle are the previously optimized ones: $l = 15$ mm, $r_\mathrm{l} = 9$ mm, $r_0 = 0.1$ mm, and $a = 34$ mm.

6.3.1 Linearly polarized normal incidence

At first, the array is illuminated with a linearly polarized plane wave. The electric field of the incident wave is directed along the x-axis: $\mathbf{E}_\mathrm{inc} = E_\mathrm{inc}\hat{\mathbf{x}}$, i.e., the incident electric field is parallel to the particle's electric dipole. The power reflection and transmission coefficients and axial ratio for the simulated and the analytical model can be seen in Fig. 11. The results show good correspondence, especially in terms of reflection and transmission coefficients. However, the frequency of the resonance is shifted from 1.55 GHz of the simulation result to 1.70 GHz of the analytical model. The shift is due to the antenna model and a similar effect has been reported earlier [36]. It seems that the frequency shift in the analytical model is caused by the difference in the loop input impedance and if this impedance is replaced with simulated one, the frequency of resonance is predicted correctly. Also the capacitance of the gap between the ends of the loop is neglected.

These results correspond to the theoretical operation of a CPSS: any plane wave can be split into two circularly polarized waves [4]. In a linearly polarized wave the left- and right-handed components are equally strong and at the surface the right-handed component is reflected and the left-handed is transmitted. This is exactly what is seen in Fig. 11 as at the resonance half of the power is reflected and the transmitted part is LH while the reflected one is RH.

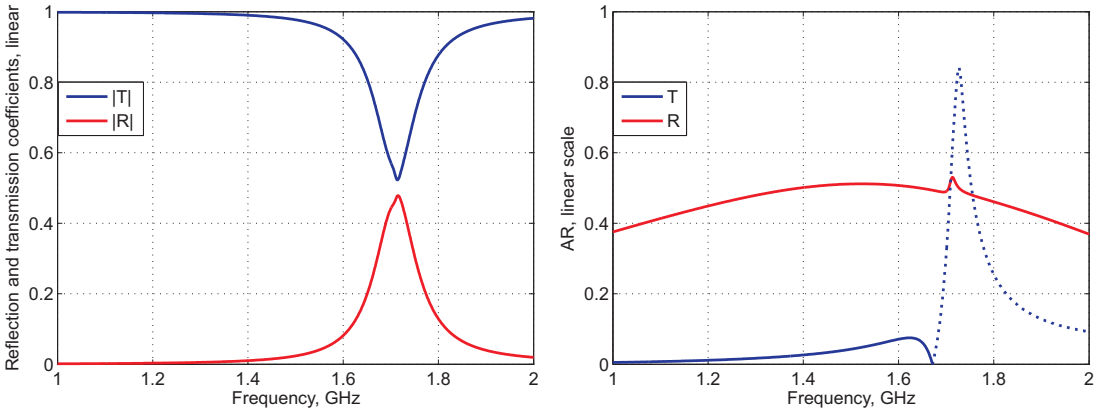

(a)

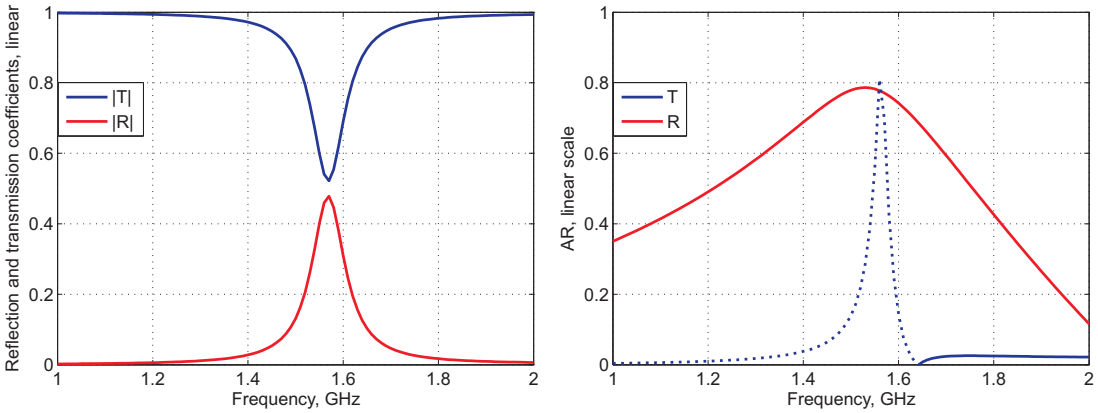

(b)

Figure 11: Comparison of (a) analytical model and (b) the numerical simulations for linear polarization $\mathbf{E}_{\text{inc}} = E_{\text{inc}}\hat{\mathbf{x}}$. In AR plots the solid lines correspond to RH and the dotted lines to LH polarization.

6.3.2 Circularly polarized incident field

For circularly polarized incidence, the analytical model correctly predicts the frequency response of the surface, but the resonance frequency has shifted a bit, as discussed previously. The results for the case of $r_1 = 9$ mm and $l = 15$ mm can be seen in Figs. 12 and 13, for RHCP and LHCP incidences. Again the results show good correspondence. At the center frequency, where the polarization selectivity is strongest, the simulated AR of the reflected RHCP wave is 0.75 and the AR of the transmitted LHCP wave is 0.70. It is curious how the AR of the transmitted LHCP wave deteriorates even if the power is transmitted almost totally. The 3 dB bandwidth of RHCP reflection is simulated to be 5.3% whereas the analytical model shows a bandwidth of 5.8%.

If the transmitted and reflected powers from Fig. 12 and Fig. 13 are summed and the sum is divided by the total incident power, the result should, of course, be unity

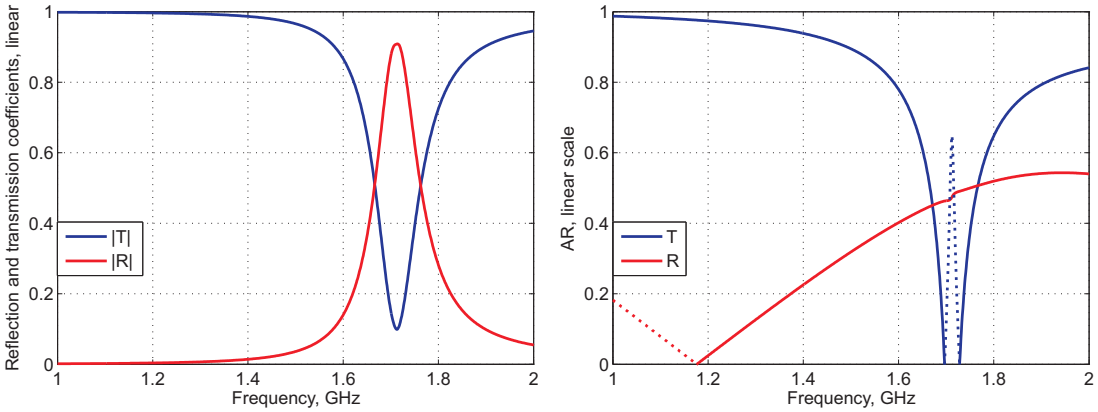

(a)

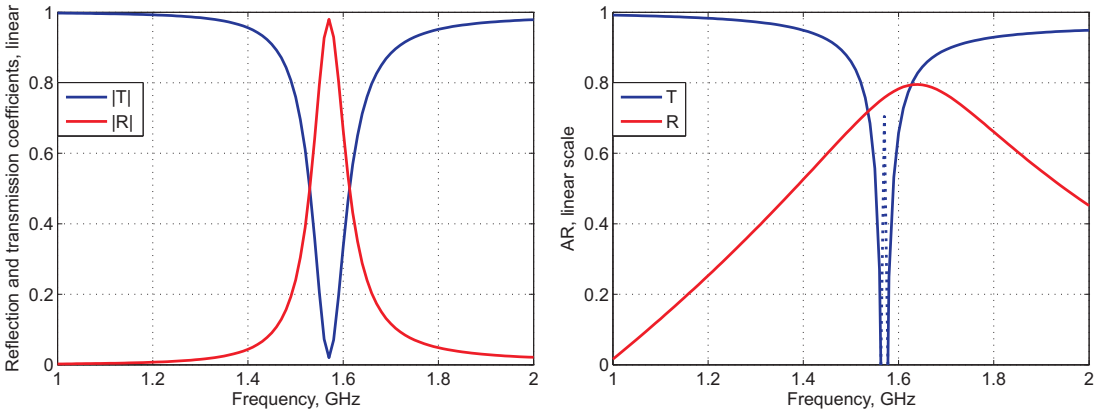

(b)

Figure 12: Comparison of (a) analytical model and (b) the numerical simulations for an array of chiral particles with incident RHCP wave. In the AR plots the solid lines correspond to RH and the dotted lines to LH polarization.

as the particles are made of ideal conductor and are in vacuum. With the analytical model, however, this is not exactly the case. The result can be seen in Fig. 14 for both LHCP and RHCP. The result varies between 0.96 and 1.03, showing a slight violation of the energy conservation. This variation is caused by the approximative nature of the polarizabilities in the antenna model [36]. In the literature, there are ways to modify the polarizabilities so that the energy conservation is satisfied [35]. This is, however, out of the scope of this thesis as the presented analytical model is only a way to verify the result of the synthesis.

In the literature, many different ways of visualizing data has been used. For example, in [24] the authors consider only the transmitted wave and calculate isolations for both handednesses of the incident field. The isolation for, e.g., RHCP is calculated by illuminating the surface with RHCP wave and then measuring the power of the RHCP component of the transmitted wave. The isolation is the ratio of these two powers. This figure of merit is a practical one as only the transmitted

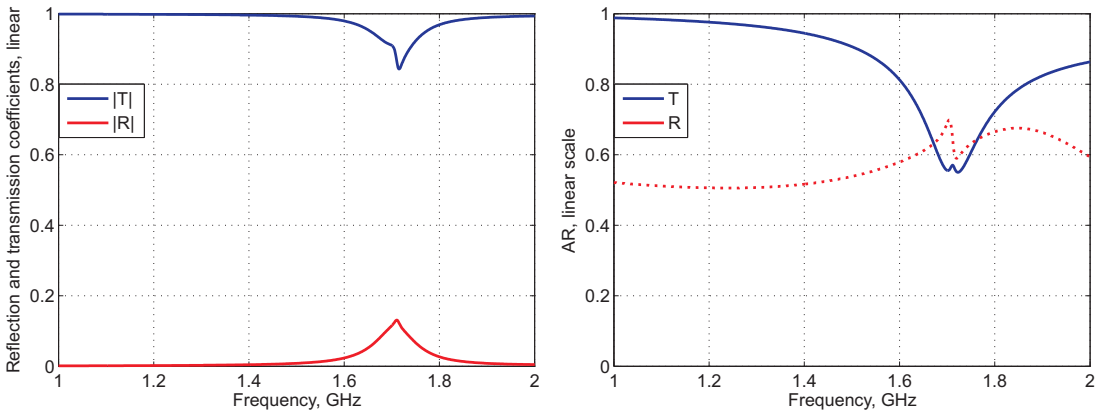

(a)

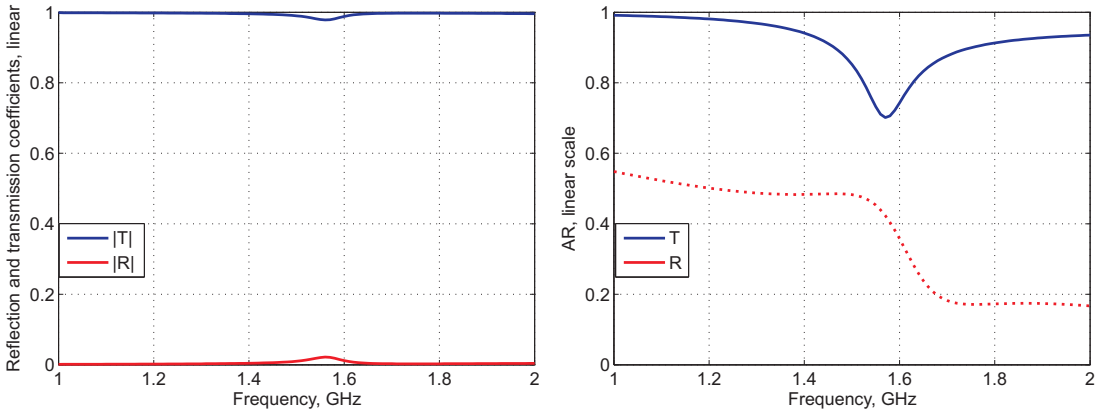

(b)

Figure 13: Comparison of (a) analytical model and (b) the numerical simulations for an array of chiral particles with incident LHCP wave. In the AR plots the solid lines correspond to LH and the dotted lines to RH polarization.

wave has to be measured. However, by considering only the isolation, we lose essential information about, e.g., the polarization purity of the reflected wave. Also, for a good RHCPSS the isolation for RHCP would be very large, as most of the RHCP power is reflected, but it is not possible to determine if large isolation is caused by reflection, absorption, or change in polarization handedness. The simulated isolation (RHCP) and transmission loss (LHCP) for this idealized PEC structure can be seen in Fig. 15. The transmission loss for LHCP is very low, only 0.23 dB. For the design in [24], the maximal measured transmission loss was 8 dB. Also the maximal isolation is very good.

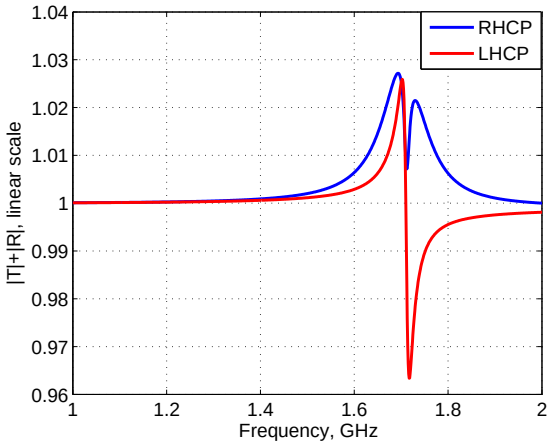

Figure 14: Energy conservation in the analytical model, in ideal case and in simulations both curves would be at unity. The model parameters are as above, i.e., $r_1 = 9$ mm, $l = 15$ mm, $a = 34$ mm, and $r_0 = 0.1$ mm.

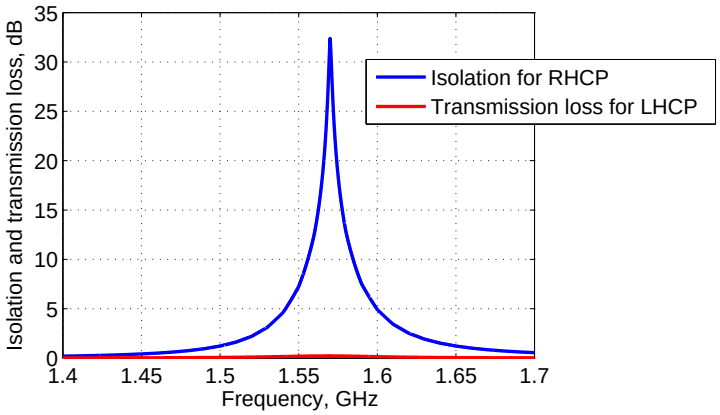

Figure 15: Simulated isolation and transmission loss for an array of RH chiral particles.

6.4 Possible modifications for canonical helix

Previously discussed design for the array of chiral particles have a limited bandwidth and the axial ratio of both reflected and transmitted wave is not very good. This section describes some possible modifications for the geometry that could improve the aforementioned properties.

6.4.1 The effect of the unit cell size

Both the analytical model and the simulations clearly show that the bandwidth of the structure will increase when the size of the unit cell is decreased. The same effect was noted by Saenz et al. [45]. In the previously shown results, the unit cell size has been $a \times a = 34$ mm $\times$ 34 mm. This size will give the bandwidths of 5.3% and 5.8% (simulated and analytical model, respectively). If we decrease a to the limit where the chiral particle just barely fits into the unit cell, i.e., $a = 32$ mm the bandwidth will increase to 6.6% or to 7.0% (again, simulated and analytical)

The size of the unit cell can be further decreased if the particle is rotated 45° around the z-axis while keeping the unit cell walls fixed. This way, the unit cell size can be further decreased to $a = 22$ mm. The geometry is shown in Fig. 16. With this modification, our simulation gives clearly better bandwidth of 13.0%. The corresponding frequency responses can be seen in Fig. 17. As the model was originally made for different geometry, there are no analytical results for this case. However, with these rotated elements the AR of the transmitted LHCP wave seems to deteriorate even more than with the previously studied case.

6.4.2 Effect of the particles orientation

The orientation of the particles seems to affect also to the bandwidth and axial ratio properties. If we turn one particle 90° around the x-axis, we get a geometry that is shown in Fig. 18. Note that the loop is still in the yz-plane and the electric dipole is parallel to the x-axis, just as in previous case. The results are shown in Fig. 19. This model produces slightly smaller bandwidth than the previously studied case (Fig. 12 and Fig. 13), but the axial ratio is better for both reflected and transmitted

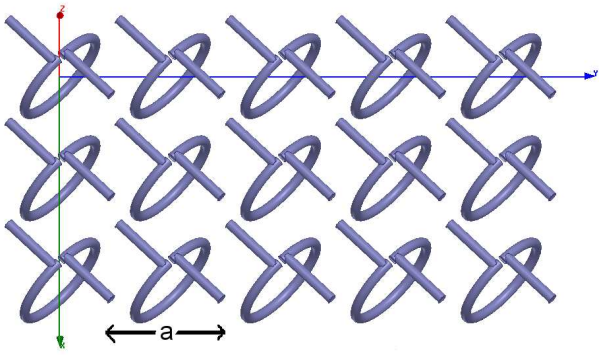

Figure 16: The simulation model for the rotated chiral particles.

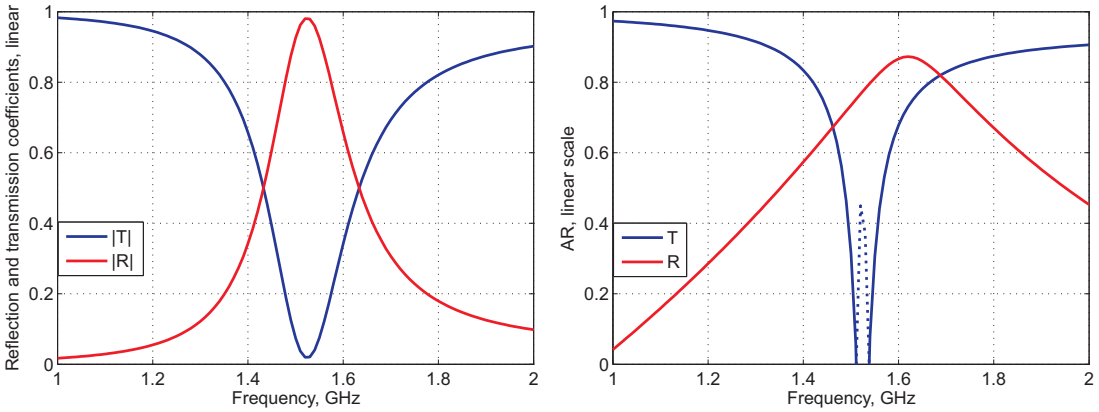

(a)

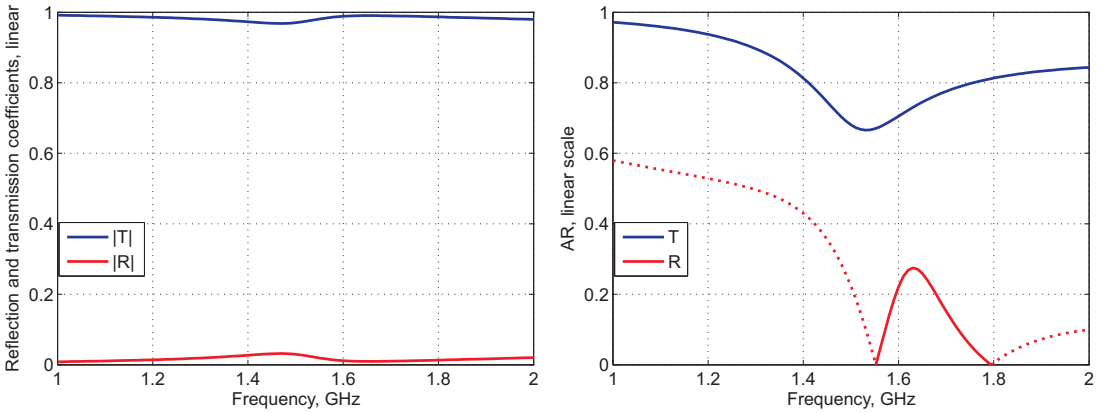

(b)

Figure 17: The simulated frequency response for an array of rotated chiral particles with (a) RHCP and (b) LHCP incidence. In the AR plots solid lines correspond to the handedness of the incident wave and dotted to the opposite one.

waves. The analytical model for this case would be only slightly different from the previously shown one, as only the electric polarizability of the loop is modified: the y-directed dipole moment will be replaced with the vertical polarizability of the loop (that previously pointed upwards). This new loop polarizability does not couple into the two other dipole moments and therefore disturbs the axial ratio less.

If the particle is rotated 90° around the y-axis, the incident wave sees only the electric polarizability of the loop. With this geometry we do not get any polarization discrimination as the magnetic dipole moment does not contribute to the radiated field.

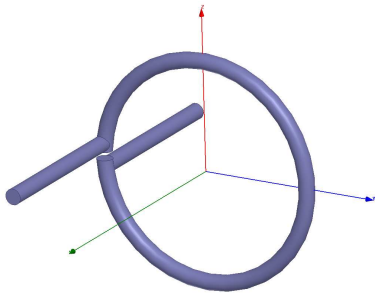

Figure 18: The simulation model for chiral particle rotated around x-axis.

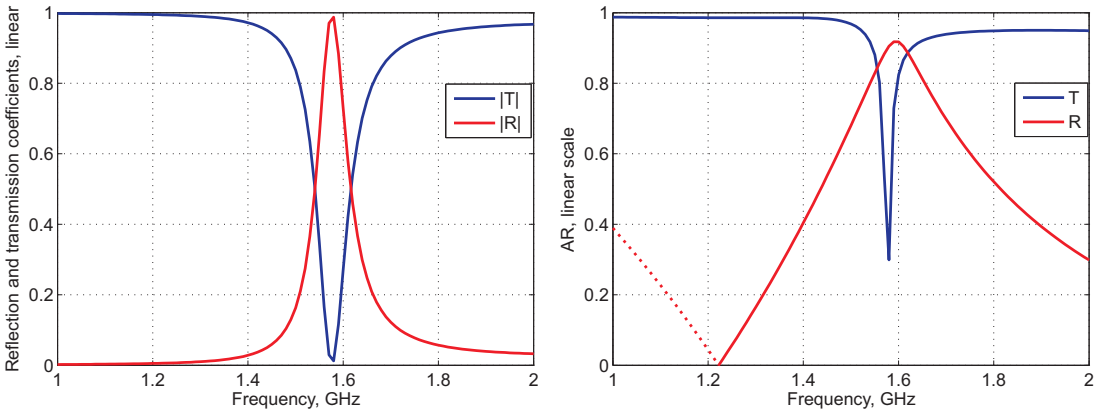

(a)

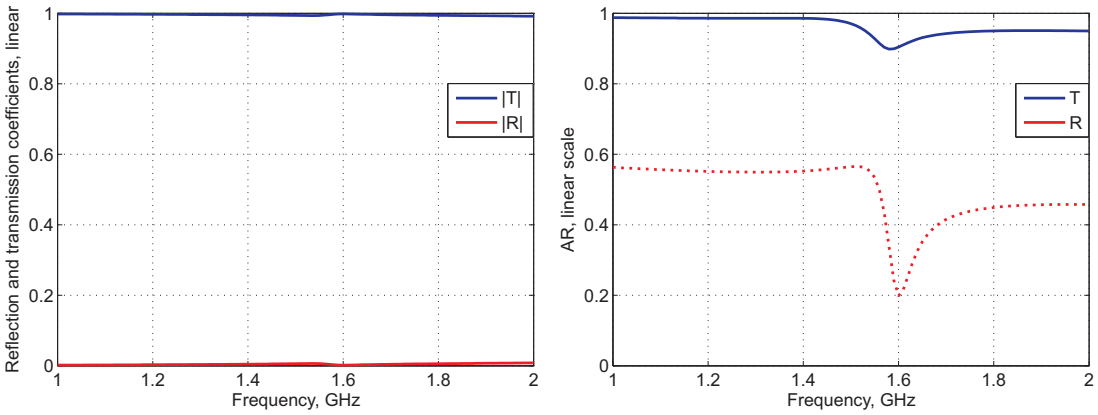

(b)

Figure 19: The simulated frequency response for an array of chiral particles that are turned around x-axis (as in Fig. 18). With (a) RHCP and (b) LHCP incidence. In the AR plots solid lines correspond to the handedness of the incident wave and dotted to the opposite one.

6.4.3 Array of horizontal $\lambda_0/2$ true helices

The electromagnetic properties of chiral particles studied in this section qualitatively correspond to a true helix whose total length is $L \approx \lambda_0/2$. The previously discussed results show that the induced p_y is limiting the resulting axial ratio. The effect can be minimized by twisting the helix so that the charges on the opposite sides of the xz-plane cross-section will cancel each other out and reduce p_y to zero. The current distribution in the wire can be assumed to be cosine-shaped, i.e., the same as in an equally long straight dipole:

$$I(x) = I_0 \cos(k_0 x) \tag{136}$$

The electric current is, by definition, movement of charges:

$$\frac{\mathrm{d}I(x)}{\mathrm{d}x} = -j\omega\rho(x) \tag{137}$$

The charge density can be easily solved from the current distribution:

$$\begin{aligned} \rho(x) &= \frac{j}{\omega}\frac{\mathrm{d}I(x)}{\mathrm{d}x} \\ &= -jI_0\sqrt{\epsilon_0\mu_0}\sin(k_0 x) \end{aligned} \tag{138}$$

By definition, the dipole moment is $\mathbf{p} = Q\mathbf{d}$. If we bend a wire with the aforementioned (138) charge distribution to form a helix with the radius r_1, the y-directed dipole moment can be solved by integrating:

$$p_y = \int_{-\alpha}^{2\pi+\alpha} y(\phi)\rho(\phi)\mathrm{d}\phi \tag{139}$$

Here ϕ circulates around the helix as illustrated in Fig. 20. Function $y(\phi) = r_1 \sin(\phi)$ presents the y-coordinate of a helix section as the function of ϕ. The equation $p_y = 0$ can be solved as follows:

$$\begin{aligned} &\int_{-\alpha}^{2\pi+\alpha} \left(\sin(\phi)\sin\left(\frac{\phi-\pi}{\pi+\alpha}\frac{\pi}{2}\right)\right)\mathrm{d}\phi \\ &\qquad = -\frac{8(\alpha-\pi)^2\cos(\alpha)}{(2\alpha+\pi)(2\alpha+3\pi)} = 0 \end{aligned} \tag{140}$$

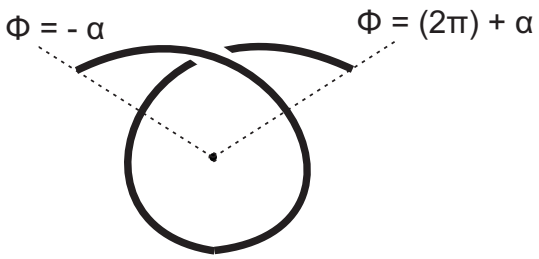

Figure 20: The geometry for the problem of p_y elimination.

One solution for $p_y = 0$ is:

$$\alpha = +\frac{\pi}{2} \tag{141}$$

The equation (140) has also other solutions, but these have not been verified numerically. However, when the wire is twisted to form a helix with multiple turns, it seems likely that the current density will differ more and more from the assumed cosine distribution of a straight wire dipole. This change would mean inaccurate initial condition and hence a less accurate solution.

The structure has been simulated in HFSS to verify the properties obtained with this method. The length of the helix is optimized to be $h = 15.5$ mm while keeping the total length of the wire and the number of turns (1.5) constant. With this length the pitch of the helix is 10.3 mm and the diameter is 21 mm. The results can be seen in Fig. 21, showing clear improvement in the axial ratio. At the center frequency AR is simulated to be 0.74 for LHCP and 0.91 for RHCP. Also the bandwidth is increased to 14.3%. It is likely that $\alpha = 90^\circ$ is not the optimal solution, as in the twisted wire the current density differs from the one in a straight wire.

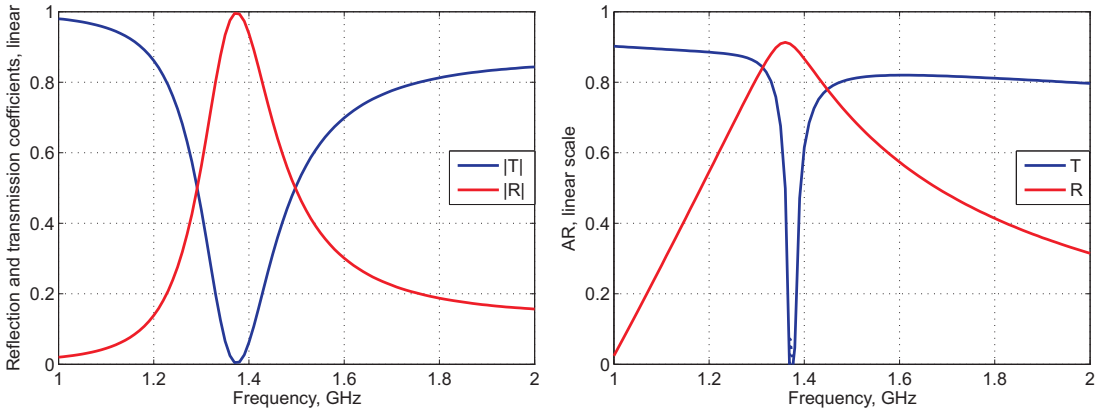

(a)

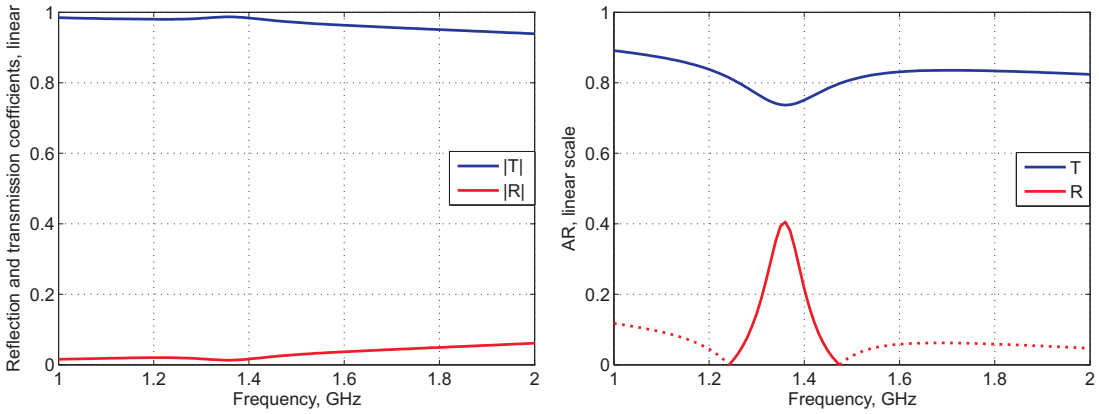

(b)

Figure 21: Transmission and reflection coefficients and AR for a $\lambda_0/2$ helix of $1\frac{1}{2}$ turns. With (a) RHCP (b) LHCP incidence. In the AR plots solid lines correspond to the handedness of the incident wave and dotted to the opposite one.

6.5 Numerical simulations for practical PCB realization

For practical applications, PCB manufacturing is preferred in order to ensure the uniformity of the unit cells in very large arrays. None of the previously discussed geometries can directly be etched on a standard two-layered PCB. However, if the loop is made rectangular and the upper parts are straightened, the induced dipole moments are preserved at least in a qualitative way. The electric dipoles on the upper layer are rotated to close the loop and to balance the strengths of the dipole moments. The resulting geometry with the optimized dimensions for 10.8 GHz can be seen in Fig. 22. The substrate is selected to be Rogers Duroid 5880 [46] that has the permittivity of $\epsilon_r = 2.2$, the dissipation factor $\tan\delta = 0.0009$, and the thickness $h = 1.575$ mm. The manufacturing process limits the dimensions [47]: the width of the strip is $w = 0.125$ mm, the via diameter 0.30 mm, and the diameter of the pad around the via is 0.6 mm. In order to prevent the metallic parts of the neighboring

particles to get too close to each other, the entire particle is rotated inside the unit cell by 30°. A part of the array of these optimized particles can be seen in Fig. 23.

The numerical results for transmission and reflection coefficients and the transmitted and reflected AR can be seen in Fig. 24. The figures clearly show that the designed geometry acts as a RHCPSS, but that the axial ratio is too low, i.e., both the transmitted and the reflected wave are probably too linear for practical antenna applications. The isolation and transmission loss are shown in Fig. 25. The maximal insertion loss is 2.6 dB which very is low if compared to the 8 dB level presented in [24] (see Fig. 5). The reason for this is in difficulties to realize a highly-symmetric particles within the limitations of the PCB technology.

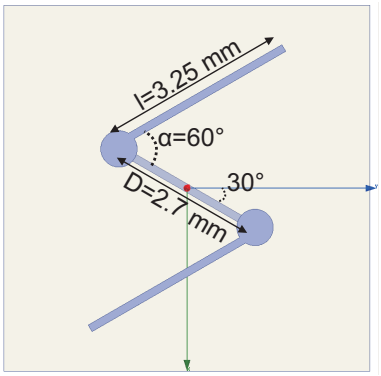

Figure 22: The geometry of a practical PCB realization of a RHCPSS. The middle section, with length D, is on the second layer.

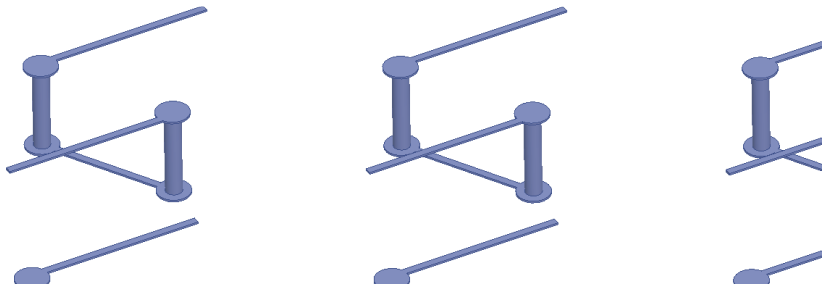

Figure 23: The array of modified chiral particles on a PCB substrate. Lattice constant is $a = 6$ mm.

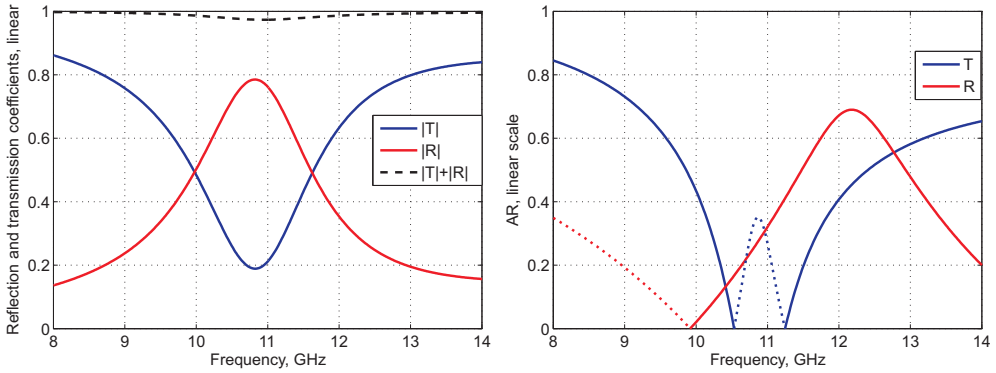

(a)

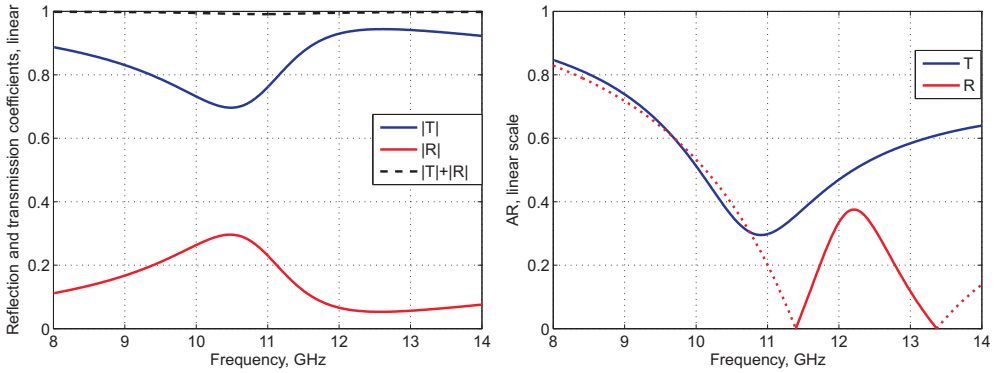

(b)

Figure 24: Transmission and reflection coefficients, efficiency as the sum $|T| + |R|$, and AR for an array of chiral particles on a PCB. With (a) RHCP (b) LHCP incidence. In the AR plots solid lines correspond to the handedness of the incident wave and dotted to the opposite one.

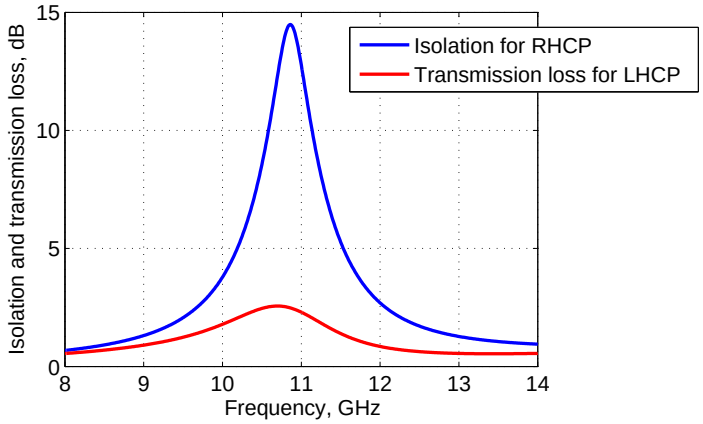

Figure 25: Simulated isolation and transmission loss for an array of modified chiral particles on a PCB.

7 An array of chiral elements as a twist polarizer

As it was noted in Section 4.2, a properly designed array of chiral elements, each comprising two orthogonal canonical helices, acts as a twist polarizer. The geometry of a single chiral element can be seen in Fig. 26. Note that the color of the other helix has been changed only for clarity reasons; both helices are made of PEC. Due to the symmetry of the design, the helices can touch each other at the bottom of the loop without disturbing the operation. This is a clear advantage when considering a practical PCB realization.

7.1 Numerical study of an idealized twist polarizer

The idealized structure, shown in Fig. 26, can be simulated with HFSS [42] similarly to the simulations described in Section 6.2. The model comprises a chiral element that is made of a PEC wire and positioned in vacuum. The chiral element is surrounded by periodical boundary conditions and has Floquet ports on both sides of the structure. The structure is then illuminated with a linearly polarized plane wave and the co- and cross-polarized components of the transmitted wave are studied.

As the analytical studies show, the loop radius and the length of the electric dipole affect the relative magnitudes of the polarizabilities of the scatterer and the induced dipole moments must be in balance. If two canonical helices are positioned orthogonally in the same position, they have only a small effect on each other [39]. This isolation is further improved when the particles are positioned exactly at the same point as is done here. Therefore, adding another canonical helix does not change the balance of the polarizabilities in a single particle and the optimal dimensions are found to be the same as for the previously optimized CPSS. The simulations are done with the following parameters: the loop radius $r_1 = 9$ mm, the wire length $l = 15$ mm, and the wire radius $r_0 = 0.1$ mm.

When the absolute strengths of both components of the transmitted wave are

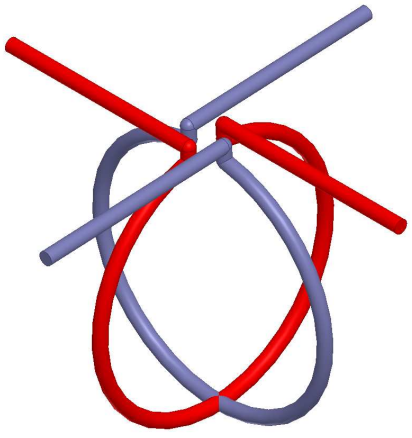

Figure 26: The geometry of a chiral element. The thickness has been increased and the color of the other helix has been changed for clarity.

plotted in Fig. 27(a), it is clear that, at the center frequency, the co-polarized component is very small and almost all power is transmitted as cross-polarized. The axial ratio, presented in Fig. 27(b), shows very good linearity of the transmitted wave. The reflected wave is totally co-polarized, as can be seen in Fig. 27(c). As Fig. 27(d) shows, the power reflection coefficient is also very small, only 0.27 dB at the center frequency. This is expected, since a single properly balanced chiral element has ideally zero backscattering [38] and the reflection from an array is the sum of the scattered fields.

As was noted in the literature review, a crucial figure of merit for a polarization rotator is the rotation angle per wavelength ($^\circ/\lambda_0$). The polarization direction of the transmitted LP wave can be calculated from the absolute values of the transmitted wave's orthogonal components. When the incident field is polarized along x, the transmitted wave is $\mathbf{E}_\mathrm{t} = E_\mathrm{t}^x\hat{\mathbf{x}} + E_\mathrm{t}^y\hat{\mathbf{y}}$ and the polarization rotation angle ϕ is given

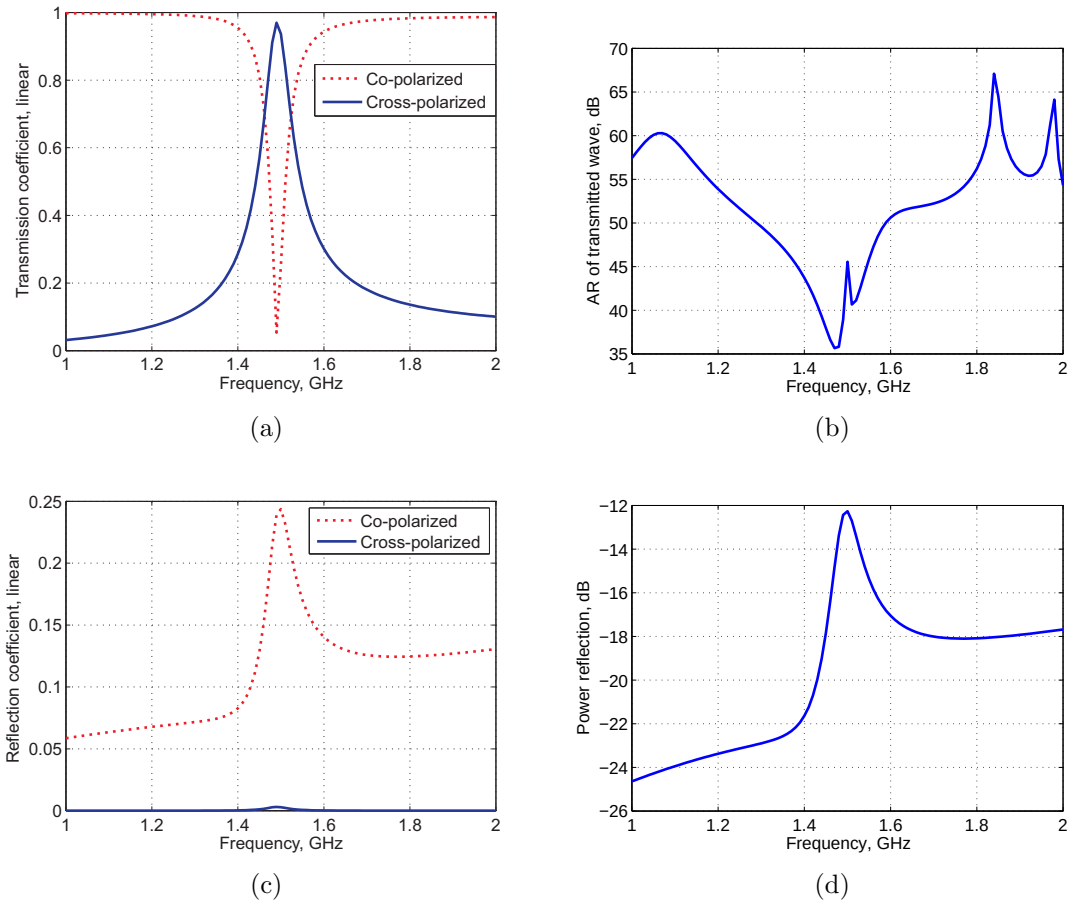

Figure 27: The numerically simulated results for $\mathbf{E}_\mathrm{inc} = E_0\hat{\mathbf{x}}$. (a) Field strength (linear scale) of transmitted co- and cross-polarized components; (b) The axial ratio of the transmitted wave in dB; (c) Reflected field strength (linear scale) of co- and cross-polarized components; (d) The power reflection coefficient in dB.

by:

$$\phi = \arctan\left(\frac{|E_{\mathrm{t}}^{y}|}{|E_{\mathrm{t}}^{x}|}\right) \tag{142}$$

For this structure, the rotation is 90°. As the loop radius is $r_{\mathrm{l}} = 9$ mm and the wavelength at the center frequency is $\lambda_0 = c_0/f_0 = 200$ mm, the polarization is rotated by $1000°/\lambda_0$.

7.2 Numerical study of practical PCB realization

The idealized structure, comprising PEC wires floating in vacuum, shows very good results. However, this design is not very practical and needs modifications to enable a PCB realization. The geometry of a single modified inclusion is shown in Fig. 28. Again, the colors are only to increase clarity, the element is made of copper. Also, the substrate is not shown. Similarly to the previously discussed PCB realization of the CPSS, the loop is straightened into a rectangular shape and the electric dipoles on the upper layer of the PCB are made to start directly from the upper end of the vias. They are also shifted slightly outwards so that the distance between the wire and the next collar is increased.

Similarly to the PCB realization of the CPSS, the structure is manufactured on Rogers Duroid 5880 [46] that has the permittivity of $\epsilon_r = 2.2$, the dissipation factor $\tan\delta = 0.0009$, and the thickness $h = 1.575$ mm. The thickness of the copper layer is 35 μm. The design frequency is selected to be around 10 GHz. The manufacturing process limits the dimensions to the following values: the widths of the strips are $w = 0.25$ mm, the via diameter is 0.5 mm, and the diameter of the pad around the vias is 0.9 mm. These limits are slightly larger than for the planned CPSS to further minimize the effect of the non-idealities in manufacturing. The following parameters are optimized in order to maximize the rotation of polarization plane and to minimize reflections: the length of the electric dipole on the upper layer is $l = 3.4$ mm, the length of the bottom of the loop is $D = 2.7$ mm, and the electric dipole is rotated by $\alpha = 65°$ from the bottom of the loop. Finally, all inclusions are rotated by 30° inside

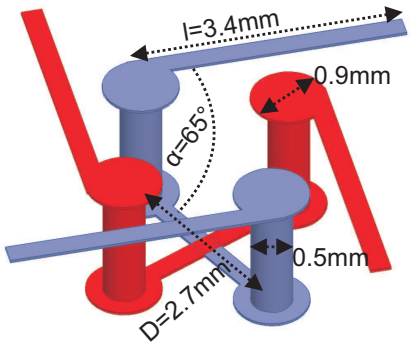

Figure 28: The geometry of modified chiral elements on a PCB. The structure is made of copper, the colors are only for clarity.

the unit cell to increase the distance of the conductors of the neighboring particles, while keeping the unit cell size a constant. The electromagnetic properties of the uniaxial particles do not change when the particles are rotated in the transversal plane. A portion of the array can be seen in Fig. 29.

7.3 Experimental verification of the twist polarizer

To experimentally verify the operation of the proposed design, the structure with the optimized dimensions has been manufactured on a PCB substrate. Due to the high accuracy requirements, the sheet is manufactured by a commercial PCB manufacturer Prinel Piirilevy Oy [47]. The manufacturing process limits the final size of the PCB to 300 mm $\times$ 260 mm. This corresponds to 49 $\times$ 42 unit cells and 10 $\times$ 8.5 wavelengths at 10 GHz. The vias in the manufactured polarizer have a small hole in the middle that was absent in the original simulations. However, this modification has no effect on the simulated performance of the structure. A photograph of a section of the manufactured structure can be seen in Fig. 30.

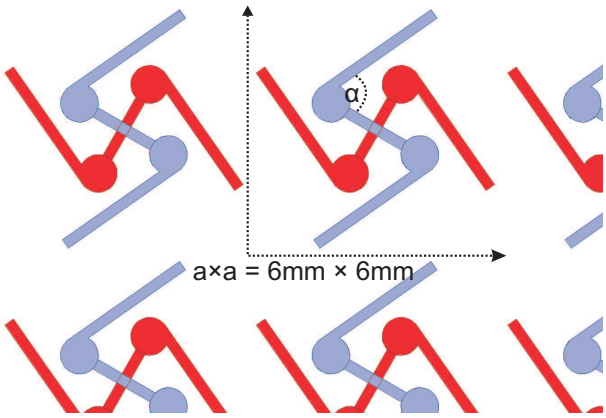

Figure 29: Array of modified chiral elements on a PCB.

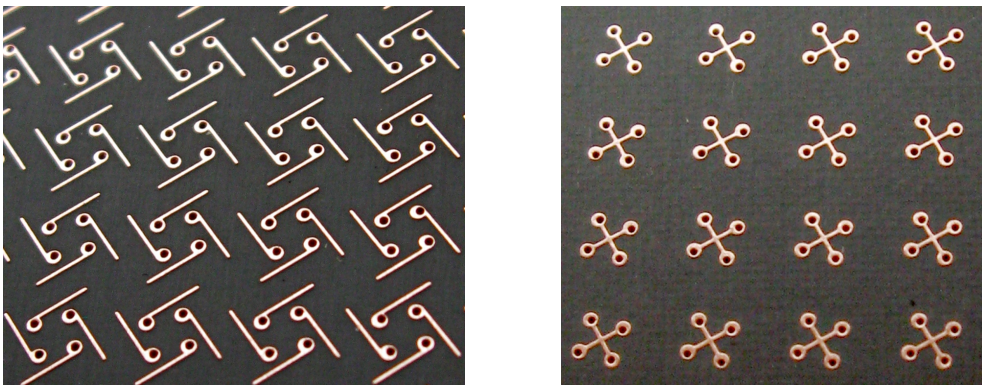

(a) (b)

Figure 30: Photographs of the manufactured polarizer: (a) upper layer, (b) bottom layer.

As the twist polarizer works for linearly polarized fields, the measurements are easily done with commercial X-band linear horn antennas. The aperture sizes of the two identical pyramidical horn antennas are $A \times B = 105$ mm$\times$90 mm. The antennas are fed with standard WR-90 waveguides that limit the measurement frequency band from 8.2 GHz to 12.4 GHz. As the twist polarizer was designed as an infinite structure that is illuminated with a plane wave, the surface must be positioned in the far-field of the antennas. At the frequency of 12 GHz, the far-field of the horn antenna with the largest dimension $D_\mathrm{h} = \sqrt{A^2 + B^2} = 138$ mm starts at [48]:

$$R = \frac{2D_\mathrm{h}^2}{\lambda_0} = 1.53 \text{ m} \tag{143}$$

The half-power beamwidths of pyramidical horn antennas can be estimated in E- and H-planes with the following approximate equations [49]:

$$HPBW_\mathrm{E} \approx 54^\circ \frac{\lambda_0}{B} \tag{144}$$

$$HPBW_\mathrm{H} \approx 78^\circ \frac{\lambda_0}{A} \tag{145}$$

At the lower end of the measurement band, the beamwidths are $HPBW_\mathrm{E} = 22^\circ$ and $HPBW_\mathrm{H} = 27^\circ$. If the polarizer is positioned at the limit of the far-field region, i.e., at distance $R = 1.53$ m from both antennas, the surface size should be at least 60×74 cm^2 in order to block the half-power beamwidth. As the manufactured surface is clearly smaller than these dimensions, most of the transmitted power would flow around the polarizer. This power could then be received by the other antenna, causing huge interference and most likely allowing only qualitative measurement results. To overcome this difficulty, a large metallic sheet is positioned between the two antennas as suggested in [24]. At the center of the metallic sheet there is a hole whose size and shape are adjusted to exactly fit the polarizer in it. The metal sheet is assembled from 50×50 cm^2 blocks and its final size is approximately 130×130 cm^2.

The sheet is then hung in the middle of the anechoic chamber of the Department of Radio Science and Engineering. The dimensions of the chamber are 8.7 m $\times$ 6.3 m $\times$ 5.5 m (length $\times$ width $\times$ height). At frequencies above 10 GHz, the reflectivity levels are -35 dB or smaller. The supporting structure and the edges of the metallic sheet are covered with RF absorbers to further minimize the interference caused by reflection and diffraction. The horn antennas are attached to standard camera tripods with in-house fabricated adapters and then positioned on the opposite sides of the metal sheet. Finally, the antennas are connected to a vector network analyzer (VNA) and an amplifier. The VNA is Agilent E8363A and the amplifier is HP 8349B that has 15 dB gain and 1 dB compression point at 21 dBm output power. Due to the nature of the measurements, the VNA is not calibrated but the normalization is done in the post-processing. The output power level is set to 0 dBm and the averaging factor to 96 to reduce the measured noise levels. The schematic of the measurement setup is presented in Fig. 31 and a photograph of the measurement site can be seen in Fig. 32. As the measurement setup can be

used also in other similar transmission measurements, the method and the estimated measurement uncertainties are discussed in greater detail in Appendix A.

At first, the S_{21} for both polarizations of the receiving antenna is measured with only a hole in the metal sheet. These two measurements act as a reference for further studies. After these measurements, the hole is blocked with a metal sheet. This gives us an estimate of the power flowing around the measurement setup. The measured levels are approximately $30 - 40$ dB smaller than with the open hole. The detailed discussion about the measurement site accuracy can be found in Appendix A. These isolation levels are clearly enough for our measurement purposes.

Finally, the designed twist polarizer is measured. The polarization rotation is calculated from the ratio of the two orthogonal S_{21} parameters without normalization as in (142): $\phi = \arctan\left(|S_{21-\text{cross}}| \,/\, |S_{21-\text{co}}|\right)$. The measurements are repeated four times and the polarization rotation is calculated as the mean value of the results of these four measurements. The measurement uncertainty is estimated by calculating the sample standard deviation for each frequency point separately [50, p. 100]:

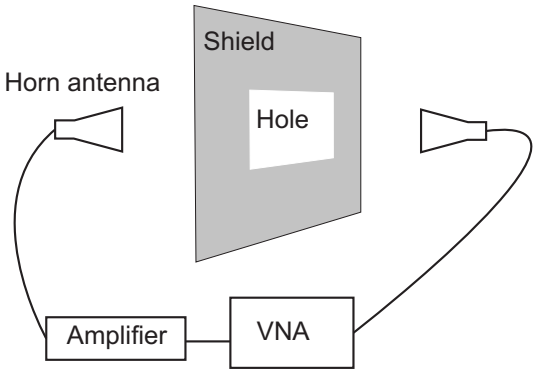

Figure 31: The measurement setup to determine the polarization properties of the twist polarizer.

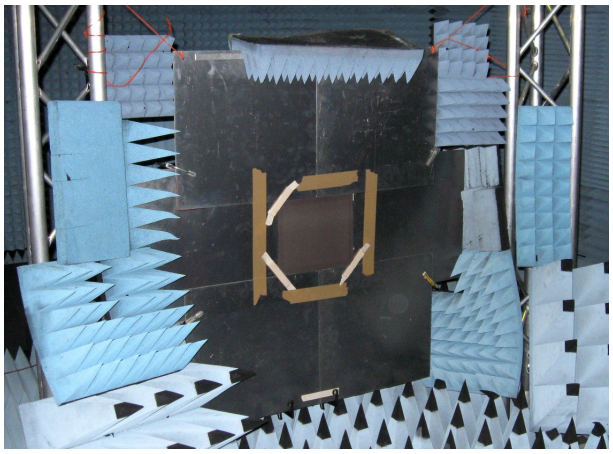

Figure 32: A photograph of the measurement setup.

$$\sigma_x = \sqrt{\frac{1}{N-1}\sum_{i=1}^{N}(x_i - \bar{x})^2} \tag{146}$$

where $\bar{x}$ is the mean value at a certain frequency point and $N = 4$ is the number of measurements. Assuming that all variations in the data are random and normally distributed, the true value of the measured quantity x deviates from the mean $\bar{x}$ less than one standard deviation with the confidence level of 68%. In other words, x_{true} falls in range $\bar{x} \pm \sigma_x$ with 68% probability [50]. Finally, these maximum and minimum estimates for uncertainty are smoothed by comparing them to the average of four neighboring frequency points and by taking the more pessimistic of these two values. No smoothing is applied to the mean value curve.

The magnitudes of the field components can be obtained if the standard Friis formula [51] is modified to take into account also the polarization mismatch:

$$P_{\text{RX}} = \left(\frac{\lambda}{4\pi \cdot 2R}\right)^2 G_{\text{RX}} G_{\text{TX}} P_{\text{TX}} \cdot S \cdot M \tag{147}$$

Here S is the effect of the shielding metal, $2R$ the distance between antennas, and M corresponds to the effect of the polarization mismatch. M is the only term that varies from one measurement to another and is also affected by the possible polarization rotation of the wave. The magnitudes of the two orthogonal field components can be obtained by dividing the measured S_{21} parameters of the twist polarizer by the co-polarized S_{21} parameters of the hole:

$$E_{\text{co}} = S^{\text{co}}_{21-\text{polarizer}} / S^{\text{co}}_{21-\text{hole}} \tag{148}$$

$$E_{\text{cross}} = S^{\text{cross}}_{21-\text{polarizer}} / S^{\text{co}}_{21-\text{hole}} \tag{149}$$

where E_{co} and E_{cross} are the normalized field strengths. It is not possible to use the cross-polarized transmission through a hole ($S^{\text{cross}}_{21-\text{hole}}$) as a reference measurement because, in the ideal case, the transmission would be zero. However, if we are interested in the phase of the transmitted wave, the normalization must be done by dividing by the $S^{\text{cross}}_{21-\text{hole}}$. As the phase information is not needed to verify the present design, the discussion on the phase measurements is done in Appendix A. The co-polarized reference measurement is not useful in the phase measurements since when turning the measurement antenna, its phase center moves several wavelengths. The power transmission in decibels is then obtained as:

$$T_{\text{dB}} = 10 \log_{10}\left(|E_{\text{co}}|^2 + |E_{\text{cross}}|^2\right) \tag{150}$$

The mean value and measurement uncertainty is then calculated similarly to the other measured variables.

7.4 Comparison of the numerical and experimental results

The numerical results for the PCB realization of the twist polarizer can be seen in Fig. 33. The results show clear correspondence with the results for the idealized

PEC structure in Fig. 27. The greates defect is the strongly increased reflection: at the center frequency the power reflection in Fig. 33(d) is -2 dB, i.e., 37% of the power is reflected back.

The experimental and numerical values for the rotation of the polarization plane can be seen in Fig. 34. The manufactured structure has slightly lower resonance frequency, but otherwise the curves show very good correspondence. The frequency shift might be caused by, for example, deviation in the material parameters of the substrate. If the permittivity of the substrate in numerical simulations is increased to $\epsilon = 2.5$, the center frequency shifts to correspond to the experimental value. However, as this deviation is much larger than the variation declared by the manufacturer ($\epsilon = 2.2 \pm 0.02$) [46], the non-idealities of the manufacturing process seem to be the more likely reason. For example, the vias are not exactly in the center of the pads. The numerical simulations show that at the center frequency $f_0 = 10830$ MHz

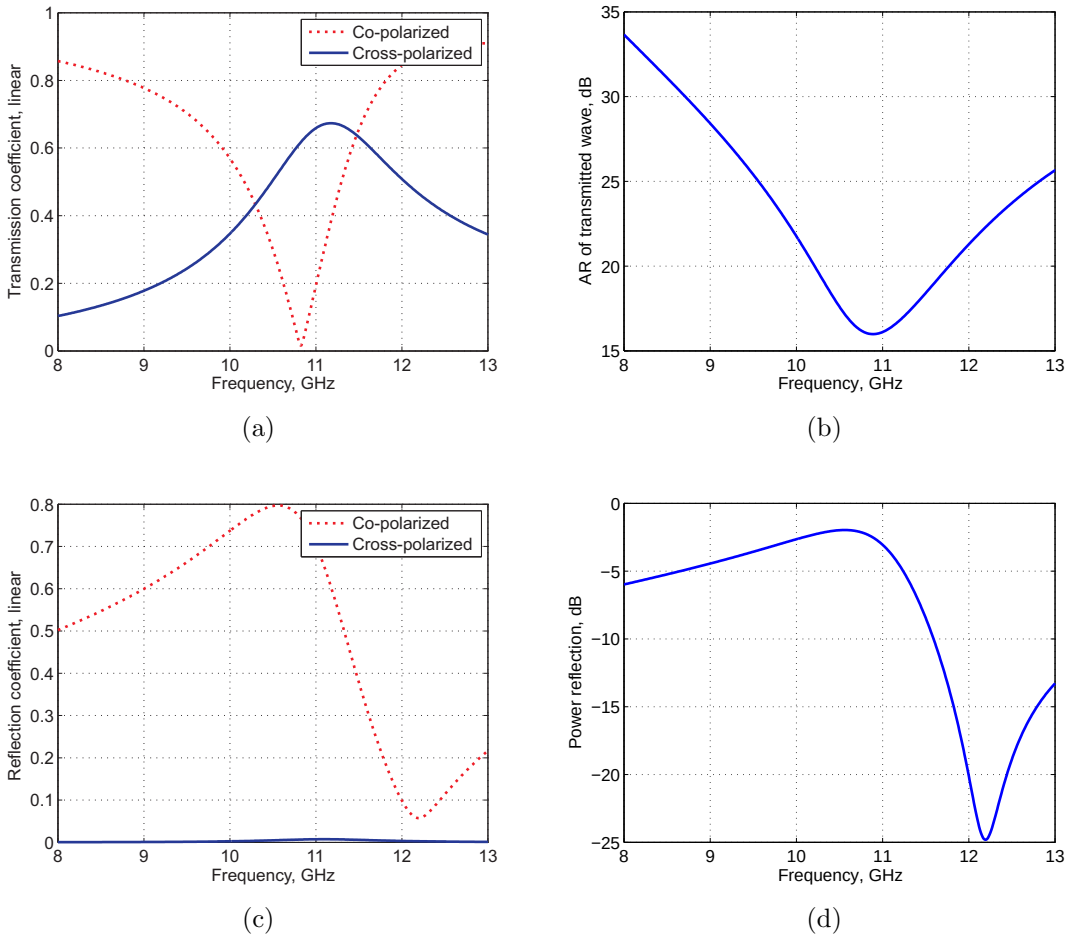

Figure 33: The numerically simulated results for the PCB realization. (a) Field strength (linear scale) of transmitted co- and cross-polarized components; (b) The axial ratio of the transmitted wave in dB; (c) Reflected field strength (linear scale) of co- and cross-polarized components; (d) The power reflection coefficient in dB.

the polarization plane is rotated 89°. On the other hand, the experimental resonance frequency is $f_0 = 10320$ MHz and the polarization rotation angle is 88°. As the thickness of the substrate is 1.6 mm = $\lambda_0/17$, the rotation per wavelength is $1540°/\lambda_0$. Another useful figure of merit is the bandwidth that can be defined as the band where the polarization rotation is at least 45°. The bandwidth of this design is 11%, in both numerical and experimental results.

The measurement accuracy of the polarization rotation angle is very good at the center frequency, the sample standard deviation being only 0.77°. This is due to the very deep drop in the co-polarized field strength. At the resonance, the S_{21} for transmitted co-polarized field has its minimum at −100 dB. The field leaking around the metal sheet has approximately the same power level and starts to limit the measurement accuracy. However, as this power is approximately 30 dB weaker than the cross-polarized component, the effect on the measured rotation angle is minimal.

The measurement uncertainty of the polarization rotation increases when the particles are no longer resonant. Especially at the high end of the measurement frequency band the uncertainty is relatively high, as the measurement frequency band slightly exceeds the band where the standard WR90 waveguide is designed for (8.2–12.4 GHz). At the lower frequencies, the largest error sources are the limited accuracy in the antenna positioning as with a standard spirit level the antenna is easily tilted at least a few degrees. When the rotation angle is calculated for only the metal sheet with a hole in it, the results are relatively constant across the frequency and vary between 1° and 5° from measurement to another. Also asymmetry of the measurement setup can cause slight rotation, but the misalignment of the antennas is most likely the largest source of error.

The experimental and numerical results for field magnitudes of both polarizations can be seen in Fig. 35. The measured results show good correspondence with the numerical values. The measurement uncertainty of the cross-polarized field strength

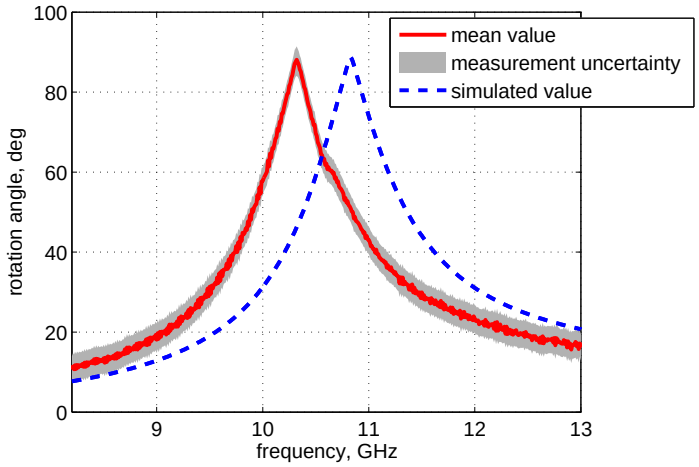

Figure 34: Polarization rotation of the manufactured twist polarizer, numerical and experimental results.

is rather large. This is caused by the normalization: as the receiving antenna is rotated between reference and real measurements, the main beam is not necessarily pointed at the transmitting antenna equally well in both measurements. As the antennas have narrow beams, pointing errors of even a few degrees cause noticeable errors in the measured field strength. The measured uncertainty levels support this theory: at higher frequencies, where the horn antenna has a narrower beam, the uncertainty levels seem to rise. In order to improve the pointing accuracy, one could equip the antenna with a laser, that points in the direction of the antenna's main beam. The measurement uncertainty could also be improved by repeating the measurements at least a few extra times.

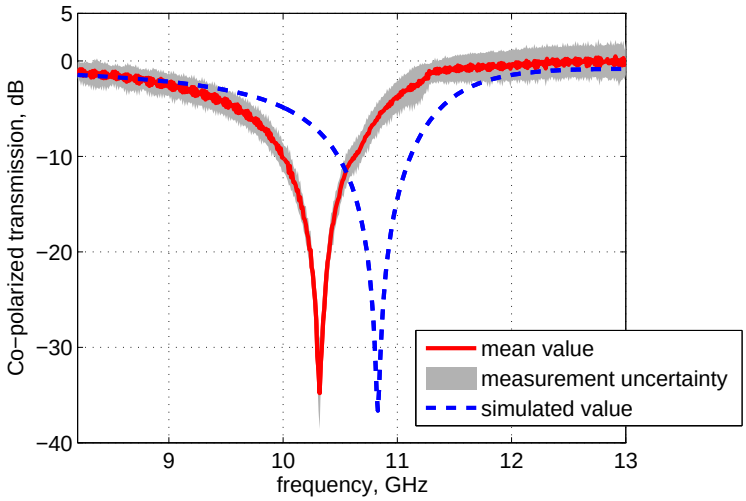

(a)

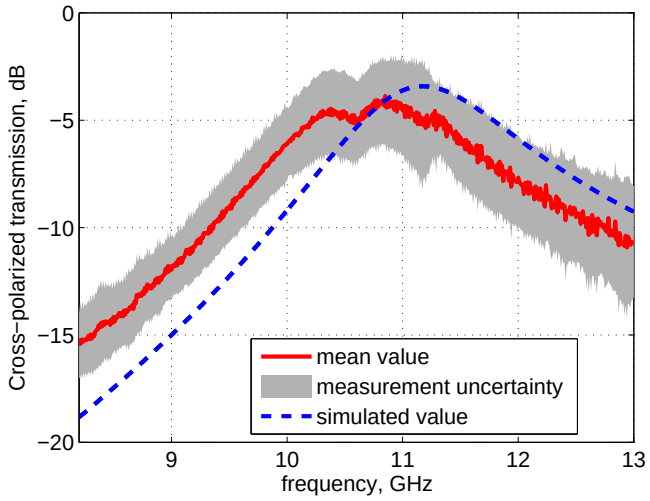

(b)

Figure 35: The numerical and experimental results for (a) co-polarized, (b) cross-polarized components of the transmitted fields. Measurement uncertainty is ± one standard deviation from the mean value.

The total power transmission coefficient for both measured and simulated results can be seen in Fig. 36. The minimum of both curves is approximately at -5 dB and also the shape is very similar. Again, the variation of the measured results and hence the measurement uncertainty is rather large. Furthermore, at the higher end of the measurement band, the measured power transmission is slightly larger than 0 dB.

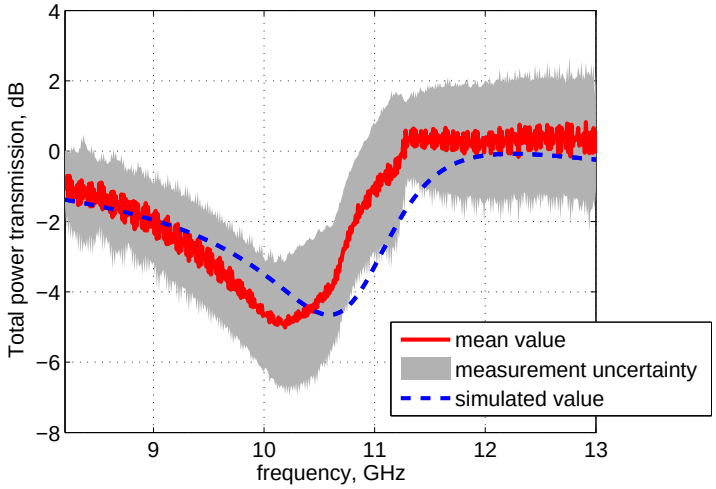

Figure 36: Measured and simulated values for total power transmission coefficient.

8 Discussion and conclusions

This thesis describes a novel way of synthesizing polarization transformers by using arrays of electrically small scatterers. The method is based on the polarizabilities of the most general bianisotropic particles and the interaction between electrically small scatterers in a square lattice. The developed method is successfully used to develop two polarization transformers: a CPSS, i.e., a surface that reflects one handedness of circular polarization and allows the other to pass the surface unchanged, and a twist polarizer, i.e., a surface that rotates the polarization state of a LP plane wave by 90°. The method can be also used in the other direction: to study if a certain polarization transformation is possible with given conditions. As an example, it is proven that circular polarization selecting device cannot be realized for normal incidence with a sheet of zero thickness, even if one would allow non-reciprocity.

The dimensions of the developed RHCPSS, namely an array of canonical helices, are optimized with FEM simulations. The structure is modeled also analytically, with good correspondence with the numerical results. Also some possible improvements of this structure are proposed and studied numerically. A possible PCB realization of RHCPSS is considered, but due to the limitations in some crucial properties the operation is not verified experimentally. The greatest defect is too low polarization selectivity, i.e., for RH incidence the power transmission coefficient is -1 dB when ideally it would reflect totally. Similarly, the reflections for LH circular polarization are too high. Furthermore, the axial ratio of both reflected and transmitted waves are probably too low for practical applications. Also, the structure has a narrow bandwidth if compared with a typical satellite communications scenario.

In order to obtain better results, one could try to modify the geometry of the inclusions with the ways presented in Section 6.4. On the other hand, one could begin the synthesis again and choose a more complex geometry with hopefully better results. Also, the effect of the substrate should be studied further. If the presented geometry is illuminated with an elliptically polarized wave, the transmission and reflection coefficients seem to improve. However, the axial ratio remains poor.

The same analytical model is used to develop a twist polarizer — a device that rotates the polarization plane of an LP plane wave by 90°. The operation of the idealized structure is verified with FEM simulations showing very good correspondence with the theory. The structure is modified for PCB realization, manufactured, and measured in the anechoic chamber. Apart from a slight deviation in resonant frequency, the experimental results show extremely good correspondence with the numerical simulations. The polarization rotation in the manufactured structure is $1540°/\lambda_0$ while the highest reported rotation is $2700°/\lambda_0$ [32]. The design presented in this thesis also suffers from considerably larger reflections than the previously reported one [32].

In conclusion, the developed analytical method is found to be a useful tool in synthesizing different polarization related operations. Furthermore, the used measurement method is found to be a practical way to study the transmission through a composite slab. Especially the co-polarized transmission, both magnitude and

phase, can be studied accurately. Although the normalization issues tend to limit the measurement accuracy for cross-polarized transmission, the measured results are in good agreement with the simulations.

Possible future work includes developing new polarization related operations with the presented method. For example, LP to CP polarizers offer new possible applications. Also, the presented designs could possibly be improved in order to obtain better results. Furthermore, the experimental verification of the CPSS was not done.

The method could also be extended to cover oblique incidence, if this is found useful. In this thesis, the oblique incidence was not considered as it would considerably increase the complexity of the synthesis. Furthermore, in most cases the practical realization will not exactly be the synthesized geometry, rendering the studies on angular stability more or less inadequate. A far more interesting direction of study would be extending the method to enable synthesis of multilayered structures. In addition to more complicated structures with possibly advantageous properties, the second sheet could be used to model a conductive ground plane that could eliminate the transmission if that is wanted. Also, the effect of the dielectric substrate could be included in the analytical model.

References

[1] S. A. Tretyakov, *Analytical Modeling in Applied Electromagnetics*. Artech House, 2003.

[2] A. H. Sihvola, "Metamaterials in electromagnetics," *Metamaterials*, vol. 1, no. 1, pp. 2–11, 2007.

[3] M. Lapine and S. A. Tretyakov, "Contemporary Notes on Metamaterials," *IET Microwaves, Antennas & Propagation*, vol. 1, pp. 3–11, Feb. 2007.

[4] I. V. Lindell, A. H. Sihvola, S. A. Tretyakov, and A. J. Viitanen, *Electromagnetic waves in chiral and Bi-isotropic media*. Artech House, 1994.

[5] B. G. Evans, *Satellite Communication Systems*. Institution of Electrical Engineers, 1999.

[6] G. Maral, M. Bousquet, and Z. Sun, *Satellite Communications Systems: Systems, Techniques and Technology*. John Wiley & Sons, 2009.

[7] G. A. Morin, "Circular polarization selective surface made of resonant helices," *U.S. Patent No. 5,280,298*, 1994.

[8] N. Amitay and A. A. M. Saleh, "Broad-band Wide-angle Quasi-optical Polarization Rotators," *IEEE Transactions on Antennas and Propagation*, vol. 31, pp. 73–76, Jan. 1983.

[9] M. Gans and N. Amitay, "Narrow multibeam satellite ground station antenna employing a linear array with a geosynchronous arc coverage of 60°, part II: Antenna design," *IEEE Transactions on Antennas and Propagation*, vol. 31, pp. 966–972, Nov. 1983.

[10] E. Plum, J. Zhou, J. Dong, V. A. Fedotov, T. Koschny, C. Soukoulis, and N. Zheludev, "Metamaterial with negative index due to chirality," *Physical Review B*, vol. 79, p. 035407, Jan. 2009.

[11] A. Serdyukov, I. Semchenko, S. A. Tretyakov, and A. H. Sihvola, *Electromagnetics of Bi-anisotropic Materials: Theory and Applications*. Gordon and Breach Science, 2001.

[12] A. H. Sihvola, *Electromagnetic Mixing Formulas and Applications*. Institution of Electrical Engineers, 1999.

[13] I. V. Lindell, A. H. Sihvola, and J. Kurkijärvi, "Karl F. Lindman: the last Hertzian, and a harbinger of electromagnetic chirality," *IEEE Antennas and Propagation Magazine*, vol. 34, pp. 24–30, June 1992.

[14] D. Jaggard, A. Mickelson, and C. Papas, "On electromagnetic waves in chiral media," *Applied Physics A: Materials Science & Processing*, vol. 18, pp. 211–216, 1979. 10.1007/BF00934418.

[15] V. Sharma, M. Crne, J. O. Park, and M. Srinivasarao, "Structural Origin of Circularly Polarized Iridescence in Jeweled Beetles," *Science*, vol. 325, no. 5939, pp. 449–451, 2009.

[16] I. V. Lindell and A. J. Viitanen, "Plane wave propagation in uniaxial bianisotropic medium," *Electronics Letters*, vol. 29, pp. 150–152, Jan. 1993.

[17] A. J. Viitanen and I. V. Lindell, "Uniaxial chiral quarter-wave polarisation transformer," *Electronics Letters*, vol. 29, pp. 1074–1075, June 1993.

[18] R. Pierrot, "Reflector for circularly polarized waves," *U.S. Patent No. 3,500,420*, 1970.

[19] J. E. Roy and L. Shafai, "Reciprocal Circular-Polarization-Selective Surface," *IEEE Antennas and Propagation Magazine*, vol. 38, pp. 18–33, Dec. 1996.

[20] G. A. Morin, "A simple circular polarization selective surface (CPSS)," in *Antennas and Propagation Society International Symposium (AP-S)*, pp. 100–103 vol.1, May 1990.

[21] J. E. Roy, "New analysis of a reciprocal Left Hand Circular Polarization Selective Surface (LHCPSS)," in *Antennas and Propagation Society International Symposium (AP-S)*, pp. 1–4, June 2009.

[22] W. V. Tilston, T. Tralman, and S. M. Khanna, "A polarization selective surface for circular polarization," in *Antennas and Propagation Society International Symposium (AP-S)*, pp. 762–765 vol.2, June 1988.

[23] "Technical proposal KI-MARK-CT-096 Vol I: Circular polarization dual-optics proof-of-concept," tech. rep., Kayser Italia, 2011.

[24] I.-Y. Tarn and S.-J. Chung, "A New Advance in Circular Polarization Selective Surface — A Three Layered CPSS Without Vertical Conductive Segments," *IEEE Transactions on Antennas and Propagation*, vol. 55, pp. 460–467, Feb. 2007.

[25] C. Dietlein, A. Luukanen, Z. Popovic, and E. Grossman, "A W-Band Polarization Converter and Isolator," *IEEE Transactions on Antennas and Propagation*, vol. 55, pp. 1804 –1809, June 2007.

[26] E. Doumanis, G. Goussetis, J. L. Gomez-Tornero, R. Cahill, and V. Fusco, "Anisotropic Impedance Surfaces for Linear to Circular Polarization Conversion," *IEEE Transactions on Antennas and Propagation*, vol. 60, pp. 212–219, Jan. 2012.

[27] M. Euler, V. Fusco, R. Cahill, and R. Dickie, "Comparison of frequency-selective screen-based linear to circular split-ring polarisation convertors," *IET Microwaves, Antennas & Propagation*, vol. 4, pp. 1764–1772, Nov. 2010.

[28] A. Alu, Y. Zhao, and X.-X. Liu, "Chirality and bianisotropy effects in plasmonic metasurfaces and their application to realize ultrathin optical circular polarizers," in *General Assembly and Scientific Symposium, 2011 URSI*, pp. 1–4, Aug. 2011.

[29] R. P. Torres and M. F. Catedra, "Analysis and Design of a Two-octave Polarization Rotator for Microwave Frequency," *IEEE Transactions on Antennas and Propagation*, vol. 41, pp. 208–213, Feb. 1993.

[30] S.-W. Ahn, K.-D. Lee, J.-S. Kim, S. H. Kim, J.-D. Park, S.-H. Lee, and P.-W. Yoon, "Fabrication of a 50 nm half-pitch wire grid polarizer using nanoimprint lithography," *Nanotechnology*, vol. 16, no. 9, p. 1874, 2005.

[31] Y. Svirko, N. Zheludev, and M. Osipov, "Layered chiral metallic microstructures with inductive coupling," *Applied Physics Letters*, vol. 78, no. 4, pp. 498–500, 2001.

[32] Y. Ye and S. He, "90° polarization rotator using a bilayered chiral metamaterial with giant optical activity," *Applied Physics Letters*, vol. 96, no. 20, p. 203501, 2010.

[33] Z. Wei, Y. Cao, Y. Fan, X. Yu, and H. Li, "Broadband polarization transformation via enhanced asymmetric transmission through arrays of twisted complementary split-ring resonators," *Applied Physics Letters*, vol. 99, no. 22, p. 221907, 2011.

[34] I. V. Lindell, *Methods for Electromagnetic Field Analysis*. IEEE Press, 1996.

[35] V. V. Yatsenko, S. I. Maslovski, S. A. Tretyakov, S. L. Prosvirnin, and S. Zouhdi, "Plane-wave reflection from double arrays of small magnetoelectric scatterers," *IEEE Transactions on Antennas and Propagation*, vol. 51, pp. 2–11, Jan. 2003.

[36] S. A. Tretyakov, F. Mariotte, C. R. Simovski, T. G. Kharina, and J.-P. Heliot, "Analytical antenna model for Chiral Scatterers: Comparison with Numerical and Experimental Data," *IEEE Transactions on Antennas and Propagation*, vol. 44, no. 7, pp. 1006–1014, 1996.

[37] P. Alitalo, A. O. Karilainen, T. Niemi, C. R. Simovski, S. A. Tretyakov, and P. de Maagt, "Chiral antennas radiating circularly polarized waves," in *Proceedings of the Fourth European Conference on Antennas and Propagation (EuCAP)*, pp. 1–5, Apr. 2010.

[38] A. O. Karilainen and S. A. Tretyakov, "Isotropic chiral objects with zero backscattering," *Eprint*, 2012. arXiv:1202.3286v1. Accepted for publication in *IEEE Transactions on Antennas and Propagation*.

[39] P. Alitalo, A. O. Karilainen, T. Niemi, C. R. Simovski, and S. A. Tretyakov, "Design and realisation of an electrically small huygens source for circular polarisation," *IET Microwaves, Antennas & Propagation*, vol. 5, pp. 783–789, May 2011.

[40] Homepage of Wolfram. Internet: `http://www.wolfram.com`. Accessed: 24.11.2011.

[41] "IEEE standard definitions of terms for antennas," *IEEE Transactions on Antennas and Propagation*, vol. 17, pp. 262–269, May 1969.

[42] Homepage of ANSYS. Internet: `http://www.ansoft.com`. Accessed: 25.11.2011.

[43] Ansoft LLC, "Getting started with HFSS: Floquet ports." Internet: `http://www.eecis.udel.edu/~spencer/HFSSFloquet.pdf`. Accessed: 24.11.2011.

[44] Homepage of MathWorks. Internet: `http://www.mathworks.com`. Accessed: 19.1.2012.

[45] E. Saenz, I. Semchenko, S. Khakhomov, K. Guven, R. Gonzalo, E. Ozbay, and S. A. Tretyakov, "Modeling of spirals with equal dielectric, magnetic, and chiral susceptibilities," *Electromagnetics*, vol. 28, 2008.

[46] Homepage of Rogers Corporation. Internet: `http://www.rogerscorp.com`. Accessed: 22.12.2011.

[47] Homepage of Prinel Piirilevy Oy. Internet: `http://www.prinel.fi`. Accessed: 3.1.2012.

[48] Y. Huang and K. Boyle, *Antennas: from Theory to Practice*. John Wiley & Sons Ltd., 2008.

[49] K. B. Baltzis, "Calculation of the half-power beamwidths of pyramidal horns with arbitrary gain and typical aperture phase error," *IEEE Antennas and Wireless Propagation Letters*, vol. 9, pp. 612 –614, 2010.

[50] J. R. Taylor, *An Introduction to Error Analysis: the Study of Uncertainties in Physical Measurements*. University Science Books, 1997.

[51] D. M. Pozar, *Microwave Engineering*. J. Wiley, 2005.

Appendix A — Measuring transmission through a slab

The experimental verification of the twist polarizer in Section 7.3 is done in the large anechoic chamber of the Department of Radio Science and Engineering. As the measurement setup has also many other applications, its assembly, operation, and estimations on the error levels are studied in this appendix.

The measurement setup is suitable for studying the transmission through a slab. The idea of the operation is to surround the measured object with a large metallic sheet that prevents the wave from leaking to the receiving antenna without going through the finite-size slab. In this thesis, the metallic sheet is assembled from separate 50 cm×50 cm metallic sheets that are attached to each others with standard clamps. This method allows a quick assembly and fine tuning the size of the hole in the middle of the metallic sheet. As an alternative solution, one could cut a hole in a suitably large continuous sheet. With this method, the weight of the metallic sheet is minimized, possibly easing the remaining assembly.

When the metallic sheet is prepared, it has to be hung in the middle of the anechoic chamber. In these measurements two light triangular antenna masts were used as is presented in Fig. 32. To stabilize the masts, suitably heavy counterweights were positioned at the feet of the masts. Alternatively, one could prevent the masts from falling under the heavy load by using stays. The studied slab must be secured to the hole by some means. In this thesis, thin wooden laths were taped to the corners of the hole on both sides and the slab was positioned between them.

The measurements are done with standard commercial X-band horn antennas. Standard camera tripods are used to position the antennas firmly in correct position. The antennas are attached to the tripods with adapters that are made of blocks of plastic that were held together by long screws. The antenna, the tripod, and the adapter can be seen in Fig. A1.

After the mechanical assembly of the measurement setup, the actual measurement devices must be connected. In these measurements the VNA is Agilent E8363A and the amplifier is HP 8349B, but other devices can be used as well. As the walls and floors of the anechoic chamber cannot be conductors, the electrostatic discharges (ESD) can occur. In order to protect the very sensitive equipment, one must always ground oneself prior to touching the VNA or the amplifier. The amplifier is connected between port 1 of the VNA and the TX antenna. The RX antenna is then connected to port 2 of the VNA and the S_{21} is measured for both polarizations of the RX antenna and for both empty hole and the polarizer in place.

The co-polarized field can be calculated simply by dividing the measured S_{21} by the reference S_{21}:

$$E_{\mathrm{co}} = S^{\mathrm{co}}_{21-\mathrm{polarizer}} / S^{\mathrm{co}}_{21-\mathrm{hole}} \tag{A1}$$

However, measuring the cross-polarized component is slightly more complicated: we must use the Friis formula [51] that is modified to take into account the polarization

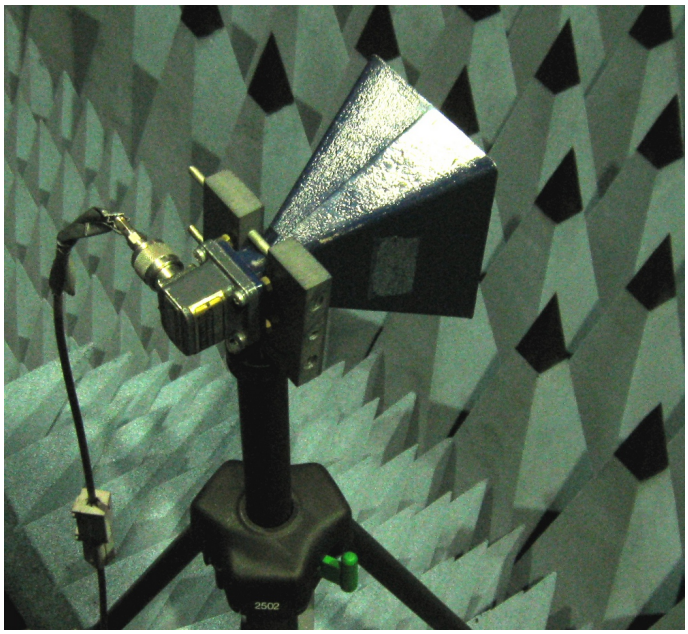

Figure A1: A standard X-band horn antenna attached to the tripod.

mismatch M:

$$P_{\mathrm{RX}} = \left(\frac{\lambda}{4\pi 2R}\right)^2 G_{\mathrm{RX}} G_{\mathrm{TX}} P_{\mathrm{TX}} \cdot SM \tag{A2}$$

The magnitude of the cross-polarized field component can be obtained by dividing the measured S_{21} parameter of the twist polarizer by the co-polarized S_{21} parameters of the hole:

$$|E_{\mathrm{cross}}| = \left|S^{\mathrm{cross}}_{21-\mathrm{polarizer}} / S^{\mathrm{co}}_{21-\mathrm{hole}}\right| \tag{A3}$$

However, if we are interested in the phase of the cross-component of the transmitted wave, the normalization must be done differently:

$$\angle E_{\mathrm{cross}} = \angle \left(S^{\mathrm{cross}}_{21-\mathrm{polarizer}} / S^{\mathrm{cross}}_{21-\mathrm{hole}}\right) \tag{A4}$$

This takes into account the distance that is travelled in the free space by the wave. As the wavelength is only 3 cm, even smallest variations in the antenna location will have a large effect on the phase.

The measurements should be repeated at least a few times and the final result is then calculated as the mean of these measurements. The measurement uncertainty is estimated by calculating the sample standard deviation for each frequency point separately [50, p. 100]:

$$\sigma_x = \sqrt{\frac{1}{N-1}\sum_{i=1}^{N}(x_i - \bar{x})^2} \tag{A5}$$

The field magnitudes with the estimated error levels can be seen in Fig. A2. The variation in the field strengths in different measurements are clearly stronger for

the cross-polarized case. The corresponding phases can be seen in Fig. A3. Again the results for cross-polarized component show much more variation. This can, of course, be seen also when the results for different measurement times are plotted separately.

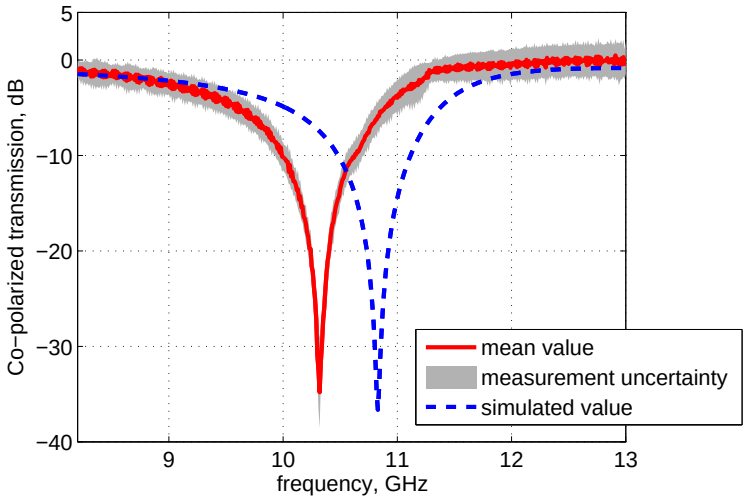

(a)

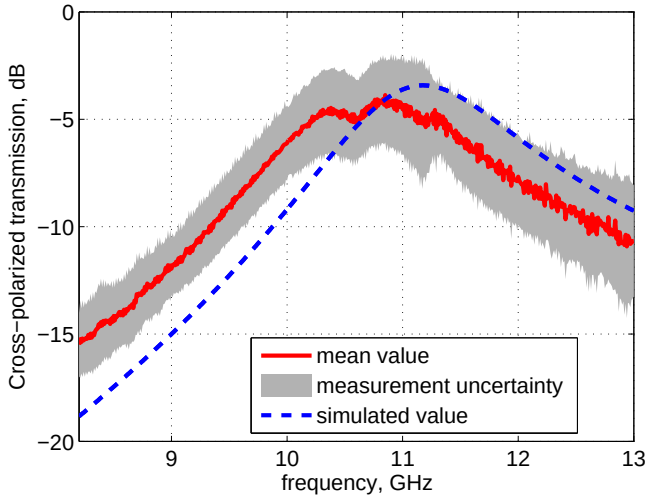

(b)

Figure A2: The numerical and experimental results for (a) co-polarized, (b) cross-polarized components of the transmitted fields. Measurement uncertainty is ± one standard deviation from the mean value.

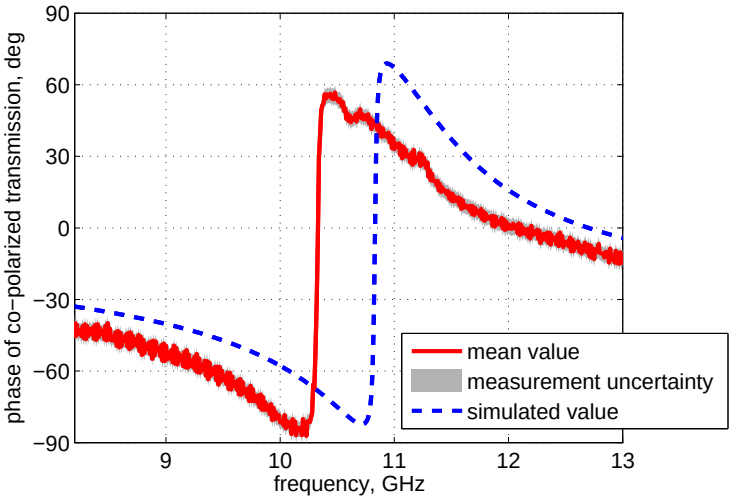

(a)

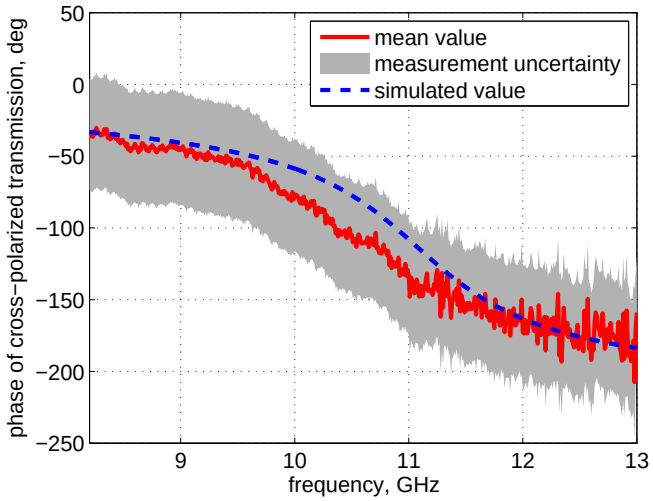

(b)

Figure A3: The numerical and experimental results for (a) co-polarized, (b) cross-polarized components of the transmitted fields. Measurement uncertainty is ± one standard deviation from the mean value.

The following piece of MATLAB code demonstrates how to calculate the mean value of measured results and the uncertainty estimates:

```
N = 4; %the amount of measurements
for k=1:1:N tmp = dlmread(sprintf('twist_CO_v%d.s2p',k),' ', 6,0); %Standard .s2p↩
     format, separated with spaces, 6 extra lines at the beginning. Different ↩
    measurements are labeled as twist_CO_v1, twist_CO_v2, ...
    S21_twistCO=tmp(:,4)+j*tmp(:,5); %the measurement data for polarizer

    tmp = dlmread(sprintf('hole_CO_v%d.s2p',k),' ', 6,0);
    S21_holeCO=tmp(:,4)+j*tmp(:,5); %reference data

    magnitude(:,k) = S21_twistCO./S21_holeCO; %normalization as described before
end
f=tmp(:,1)/1e9; %frequency in GHz

meanvalue = mean(20*log10(abs(magnitude.')))'; %mean value of the measurements

for k=1:1:length(meanvalue)
    sstd(k) = sqrt(1/(N-1)*sum((20*log10(abs(magnitude(k,:)))-meanvalue(k)).^2));
    %the sample standard deviation directly from the definition
end

uncertainty_min = meanvalue-sstd';
uncertainty_max = meanvalue+sstd';
%minimum and maximum estimates for the measurement uncertainty

figure;
fill([f',f(end:-1:1)'], [uncertainty_min',uncertainty_max(end:-1:1)'], 'b');
%fill draws a filled polygon
hold on;
plot(f, meanvalue,'r');
```